Title
Nuclear Magnetic Resonance Investigations of the Highly Correlated Unconventional Superconductor Strontium Ruthenate

Author
Chronister, Aaron Michael

Publication Date
2022

Peer reviewed|Thesis/dissertation

UNIVERSITY OF CALIFORNIA
Los Angeles

Nuclear Magnetic Resonance Investigations of the Highly Correlated Unconventional Superconductor Strontium Ruthenate

A dissertation submitted in partial satisfaction
of the requirements for the degree
Doctor of Philosophy in Physics

by

Aaron Michael Chronister

2022

ABSTRACT OF THE DISSERTATION

Nuclear Magnetic Resonance Investigations
of the Highly Correlated Unconventional Superconductor
Strontium Ruthenate

by

Aaron Michael Chronister
Doctor of Philosophy in Physics
University of California, Los Angeles, 2022
Professor Stuart Brown, Chair

Sr_2RuO_4 is the cleanest and most well-characterized example of unconventional superconductivity known to date. Early experimental reports found strong evidence for the "chiral p-wave" $\mathbf{d} = \hat{\mathbf{z}}(k_x \pm ik_y)$ superconducting state, an electronic analog to the chiral A-phase of superfluid Helium-3 [64, 33, 45]. As a result, Sr_2RuO_4 was widely accepted as the paradigmatic example of a topological quasi-two-dimensional superconductor and this colored the analysis of experimental reports for over two decades. The NMR measurements presented in this thesis directly contradict this interpretation. A pronounced drop is observed in the ^{17}O Knight shift, incompatible with the chiral p-wave state as well as a previous body of NMR work [33]. The discrepancy is shown to arise from systematic heating of the sample due to the high amplitude NMR pulses. Through quantitative measurements of the residual Knight shift as a function of applied in-plane field we additionally derive an upper bound on the magnetic response of the superconducting condensate of less than 10% that of the normal state. This is sufficient to further rule out all pure p-wave order parameter candidates for Sr_2RuO_4 and

provides strong evidence for even parity superconductivity. As such, these results represent a fundamental advancement in understanding the nature of superconductivity in this archetypal system.

The normal metallic state of Sr_2RuO_4 is also a subject of interest due to its strong correlations as well as the proximity of the Fermi energy to a quasi-two-dimensional singularity in the density of states. Application of uniaxial stress is known to be able to tune the band structure through the singularity [76] and is accompanied by profound changes to the physical properties, including a more than doubling of the superconducting critical temperature [74]. We show by way of the ^{17}O Knight shift that the Fermi liquid crossover scale in Sr_2RuO_4 can be driven to vanishing temperature with the application of in-plane uniaxial stress approaching the van Hove singularity. The behavior is then successfully described via the strain dependent dispersion of a non-interacting quasiparticle model. Finally, a recently reported magnetic phase appearing at applied stresses beyond the van Hove singularity [21] is investigated with $^{17}T_1$ measurements. Enhanced fluctuations are found in a small region of phase space near the purported line of transitions but do not extend to superconducting dome, making it unlikely they are important for the superconducting pairing mechanism.

The dissertation of Aaron Michael Chronister is approved.

Yaroslav Tserkovnyak

Anshul Kogar

Karoly Holczer

Stuart Brown, Committee Chair

University of California, Los Angeles

2022

TABLE OF CONTENTS

LIST OF FIGURES

LIST OF TABLES

ACKNOWLEDGMENTS

First I would like to thank my advisor Stuart Brown. Stuart was a great mentor and an inexhaustible source of knowledge over the last five years. I was, and still am, inspired by Stuart's experimental expertise and his physical insight. More importantly though, he is a genuinely nice guy and made my time at UCLA a pleasure. I also want to thank Andrej Pustogow, who worked closely with me in the lab on some of the projects in this thesis. He was an important second mentor who helped me take initiative and learn to be an independent experimenter. Thanks to Teresa for the good company over the years as we struggled against everything in the lab trying to break. It was nice to have someone to commiserate with during a difficult experiment. Thanks to Hank, Yongkang, and Yue-Shun for showing me the ropes when I was just a second year graduate student, you guys made joining the group an easy decision. To everyone in the lab, I appreciated our many discussions on physics (and life in general). I always learned something regardless of whether I had asked the question or attempted to answer it. Thanks as well to all my other friends near and far for keeping in touch. I looked forward to my crew from Cornell visiting for the best weekend of our lives, or getting together with the cats at James' place. Thanks of course to my family, my Mom, Dad, and my sister Sarah, who I can always rely on. Lastly, and most importantly, I want to thank my girlfriend Nancy for putting up with the whole idea.

VITA

2016	B.A. (Physics), Cornell University
2016	B.A. (Chemistry), Cornell University
2016–2022	Teaching Assistant, Physics and Astronomy Department, UCLA.
2017	M.S. (Physics), UCLA, Los Angeles, California.
2017–2022	Research Assistant, Physics and Astronomy Department, UCLA.

PUBLICATIONS

A. Pustogow, Y. Luo, **A. Chronister**, Y.-S. Su, D. A. Sokolov, F. Jerzembeck, A. P. Mackenzie, C. W. Hicks, N. Kikugawa, S. Raghu, E. D. Bauer, and S. E. Brown, "Constraints on the superconducting order parameter in Sr_2RuO_4 from oxygen-17 nuclear magnetic resonance", Nature 574, 72-75 (2019).

A. Chronister, A. Pustogow, N. Kikugawa, D. A. Sokolov, F. Jerzembeck, C. W. Hicks, A. P. Mackenzie, E. D. Bauer, and S. E. Brown. "Evidence for even parity unconventional superconductivity in Sr2RuO4." Proceedings of the National Academy of Sciences 118, no. 25 (2021).

CHAPTER 1

Introduction

A hallmark of condensed matter physics is the emergence of diverse phases of matter from the same underlying microscopic interactions. At the same time, successful descriptions of these phases involve a remarkable reduction in complexity: the behavior of systems with $\sim 10^{23}$ degrees of freedom can be determined by only a handful of collective properties. For experimentalists, tuning between different phases in the laboratory using parameters like temperature or hydrostatic pressure is a fundamental way to uncover the governing rules of many-body systems. Recently, advancements in the use of piezoelectric materials have added a new tuning parameter to the arsenal of experimental physicists: uniaxial stress. With this technique a single crystal is clamped between two piezoelectric stacks which can be actuated to produce strains of up to $1-2\%$ along a chosen direction. Unlike conventional hydrostatic pressure, this stress can be used to continuously vary electronic structure *in situ*, as well as selectively break symmetries of the crystal lattice, making it a powerful new tool for interacting with condensed matter systems.

In this thesis I apply these uniaxial stress techniques in combination with nuclear magnetic resonance spectroscopy to investigate the highly correlated, unconventional superconductor Sr_2RuO_4. This system is unique owing to the ultra-low disorder of its single crystals as well as a correspondingly well-understood normal state that is unparalleled among unconventional superconductors. Moreover, for nearly two decades since its discovery, Sr_2RuO_4 has been widely considered the paradigmatic example of a quasi-two-dimensional chiral, odd parity superconductor. This captured the attention of the experimental community due in part

to predictions that such a state could host exotic Majorana zero modes, which have important implications for fault-tolerant quantum computing [63, 37]. In recent years, however, experimental inconsistencies with this interpretation have grown, calling into question our understanding of this important system. The NMR results of this thesis address these questions by presenting robust experimental evidence directly contradicting the long held consensus of odd parity superconductivity in Sr_2RuO_4.

The main text is divided as follows. Chapter 1 introduces the basic theory of normal metals and superconductors. Chapter 2 provides an overview of the physics of Sr_2RuO_4 necessary to interpret the experimental results. Chapter 3 goes through the principles of NMR spectroscopy as well as details of the experimental setup. Chapter 4 presents new NMR data taken on the superconducting phase of Sr_2RuO_4, showing unambiguous evidence for an even parity superconducting order parameter. Finally, Chapter 5 presents experimental results on the correlated metallic phase of Sr_2RuO_4, demonstrating how applied stress can be used to tune the onset of Fermi liquid behavior, as well as magnetic order.

1.1 Theory of the Normal Metal

At first glance, one would expect any decent theory of electrons in metals to be extraordinarily complicated. In principle it involves solving an N-body problem consisting of charged electrons interacting with each other, as well as the lattice ions, via the powerful long-range Coulomb force. However, it turns out that due to the screening of electric charge by the delocalized electrons in a metal, one can arrive at a quite successful theory of metals by ignoring both of these interactions entirely. This model system is known as the free electron gas or degenerate Fermi gas.

Starting with a collection of N non-interacting electrons, the available single particle wavefunctions are just the solutions to the Schrodinger equation in free space. Each states is labeled by a wavevector $\mathbf{k}$ (or equivalently momentum $\mathbf{p} = \hbar\mathbf{k}$) and has energy:

$$E_k = \frac{\hbar^2 k^2}{2m} \tag{1.1}$$

The full many-body wavefunction is then a Slater determinant of occupied single particle states, with the total energy a sum of single particle energies:

$$\Psi(\mathbf{r_1}, \mathbf{r_2}, ...) = \begin{vmatrix} \psi_{\mathbf{k_1}}(\mathbf{r_1}) & \psi_{\mathbf{k_1}}(\mathbf{r_2}) & ... \\ \psi_{\mathbf{k_2}}(\mathbf{r_1}) & \psi_{\mathbf{k_2}}(\mathbf{r_2}) & ... \\ ... & ... & ... \end{vmatrix} \tag{1.2}$$

where $\mathbf{r_1}, \mathbf{r_2}, ...$ are the coordinates corresponding to each of the N particles. At zero temperature, electrons will populate the single particle states with lowest energy and thus smallest k. However, due to the Pauli exclusion principle, only two electrons (one for each spin state) can occupy a given $\psi_{\mathbf{k}}$. Thus, the populated single particle states will "fill up" a sphere in k-space, the boundary of which is called the Fermi surface. The filling of the single particle states is illustrated in Figure 1.1. The radius of the Fermi surface is then straightforward to calculate given the total number of electrons and results in:

$$k_F = (\frac{3\pi^2 N}{V})^{1/3} \tag{1.3}$$

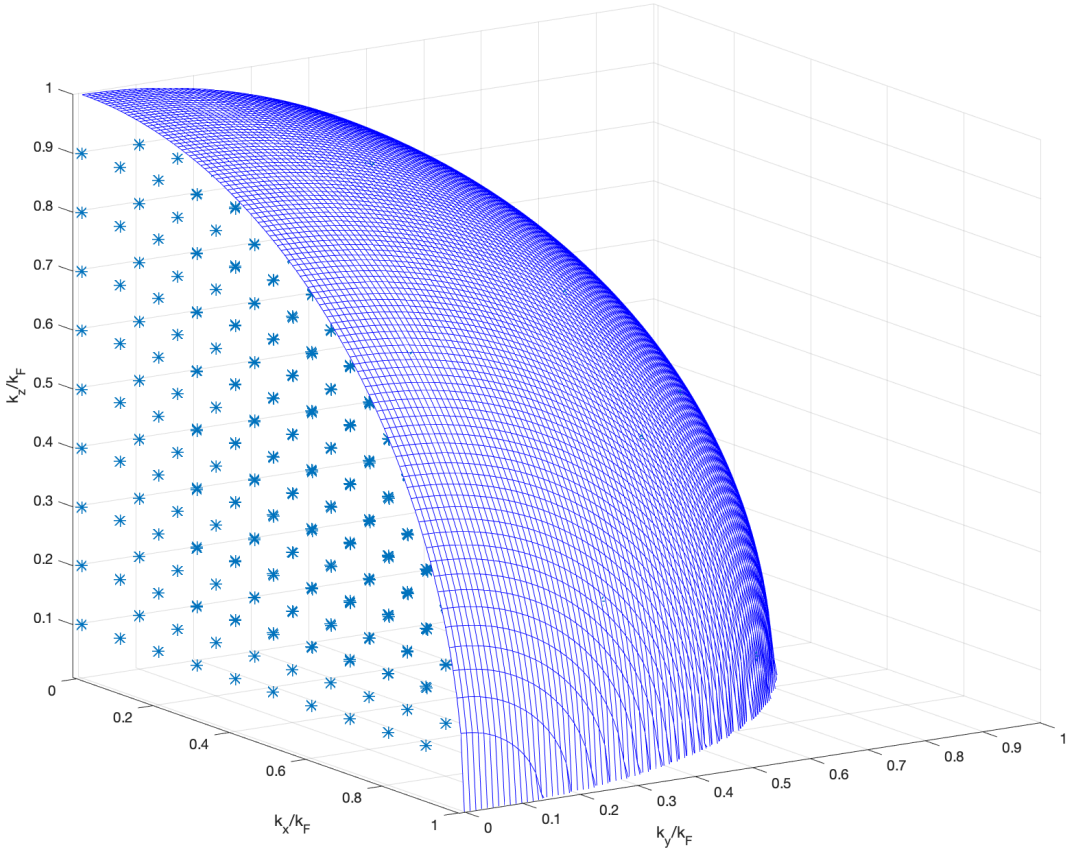

Figure 1.1: Spherical free electron Fermi surface in one octant of k-space. The blue stars represent the occupied single particle states with $k < k_F$.

Where k_F is called the Fermi wavevector and $E_F = \frac{\hbar^2 k_F^2}{2m}$ is the largest occupied single particle energy. For a real metal one can estimate E_F using a typical carrier density of $N/V \sim 10^{22}\text{cm}^{-3}$, which gives $E_F \sim 2\text{eV}$ and $T_F = E_F/k_b \sim 20{,}000\text{K}$. This is an important result of free electron theory: the characteristic temperature scale of a degenerate electron gas, imposed by the exclusion principle, is orders of magnitude higher than ambient temperature. At finite temperatures the occupation probability of a single particle state with energy E is given by the Fermi distribution:

$$f(E) = \frac{1}{1 + e^{\frac{E-\mu}{k_b T}}} \tag{1.4}$$

where μ is the chemical potential and $\mu(T = 0) = E_F$. This distribution broadens the transition between occupied and unoccupied states to an energy range of $\sim k_b T$. In principle this means the concept of a single surface containing all occupied states has broken down; however, due to the huge scale of T_F the Fermi distribution remains extraordinarily sharp even at room temperature and higher. As a result, the Fermi surface is still well-defined at all reasonable temperatures, and moreover only the electrons occupying states near this surface are important for thermodynamic properties.

To quantify this, a density of states (DOS) per unit energy is introduced. This can be calculated by considering the number of allowed quantum states with energy between E_k and $E_k + \mathrm{d}E$. For free electrons in three dimensions, the density of states at the Fermi energy is given by

$$g(E_F) = \frac{m k_F}{\pi^2 \hbar^2} \tag{1.5}$$

The left side of Table 1.1, shows some results of the free electron theory. They depend on E_k only through the DOS at the Fermi energy. Amazingly, these predictions of the electronic heat capacity are in qualitative and semi-quantitative agreement with experimental observations of simple metals in the Alkali group [39], despite the drastic oversimplification of ignoring interactions entirely.

Quantity	Free electron theory	Fermi liquid theory
Density of states, $g(E_F)$	$\frac{mk_F}{\hbar^2\pi^2}$	$\frac{m^*k_F}{\hbar^2\pi^2}$
Specific heat, c_v	$\frac{\pi^2}{3}k_b^2Tg(E_F)$	$\frac{\pi^2}{3}k_b^2Tg(E_F)$
Spin susceptibility, χ_s	$\mu_B^2 g(E_F)$	$\mu_B^2 g(E_F)\frac{1}{1+F_0^a}$

Table 1.1: Predictions of free electron theory compared to those of Fermi liquid theory. The Fermi liquid predictions are renormalized by an effective mass as well as interaction parameters, depending on the quantity. Note that the temperature dependence is consistent between both theories.

This success is encouraging, but the free electron theory has a clear flaw: it cannot explain the existence of non-metallic behavior such as as electrical insulators or semiconductors. In fact, even for some metallic elements like manganese and bismuth, experiments disagree with free electron results by almost two orders of magnitude. In these cases the interactions of electrons with the lattice ions must be considered explicitly. The periodic nature of a real crystal lattice potential significantly modifies the quadratic energy dispersion of free electrons. Models for including this effect typically begin either in a "nearly-free" electron picture where only the periodic nature of the lattice is included (but the corresponding potential is still weak), or a "tight-binding" picture starting from localized atomic-like orbitals. In either case, the potential ϕ is assumed to be invariant under translations of an integer number of primitive crystal lattice vectors $\mathbf{R}_i$:

$$\phi(\mathbf{r} + \mathbf{R}_i) = \phi(\mathbf{r}) \qquad \text{for all } i \tag{1.6}$$

Given this constraint, a general theorem from Bloch [11] shows that the corresponding solutions to the Schrodinger equation must have the form:

$$\psi_{n,\mathbf{k}}(\mathbf{r}) = e^{i\mathbf{k}\cdot\mathbf{r}}u_{n,\mathbf{k}}(\mathbf{r}) \tag{1.7}$$

where $u_{n,\mathbf{k}}$ is a periodic function of the lattice that depends on the details of the ionic potential. This decomposition is not unique, so conventionally the condition $\psi_{n,\mathbf{k}} = \psi_{n,\mathbf{k}+\mathbf{G_i}}$ is adopted

where $\mathbf{G_i}$ is a reciprocal lattice vector defined by $\mathbf{G_i} \cdot \mathbf{R_j} = 2\pi\delta_{ij}$. Using these definitions, it is sufficient to confine the wavevector $\mathbf{k}$ describing Bloch states to just the Wigner-Seitz cell of the reciprocal lattice, also called the first Brillouin zone. Importantly, $\mathbf{k}$ is no longer related to the momentum as simply $\mathbf{p} = \hbar\mathbf{k}$, since total translational symmetry has been broken. However, the Bloch wavevector plays an analogous role to the momentum in the dynamics of electrons in crystals, and is conventionally referred to as the crystal momentum.

There are two general consequences of including the lattice periodicity, the first is that the continuous spectrum of the free electron gas is replaced by bands of continuous energy levels separated by regions with no allowed states, called band gaps. Figure 1.2 illustrates the appearance of band gaps in the free electron dispersion as lattice potential is turned on. The second is a modification of the Fermi surface structure: the constant energy surface

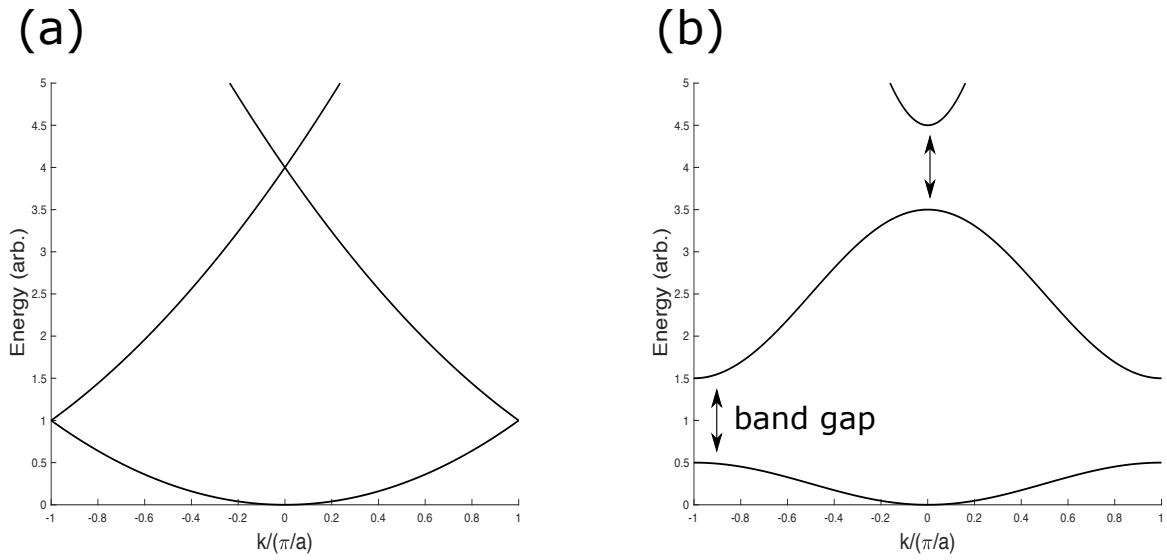

Figure 1.2: (**a**) Quadratic one dimensional free electron dispersion $E(k)$ plotted in the first Brillouin zone. There are allowed states for every energy: the spectrum is gapless. (**b**) Modification of the excitation spectrum due to a periodic lattice. Energy gaps appear which separate bands of allowed states.

in reciprocal space defined by E_F is no longer spherical as in the free-electron case, but

reflects the lower symmetry of the lattice. This is especially critical since electrons near E_F dominate the physical properties of a metal, so complicated Fermi surface structure gives rise to effects like anisotropic conduction or negative hall voltage, which cannot be explained without interactions with the lattice.

Including coupling to the ionic lattice successfully resolves many of the experimental discrepancies with the free electron theory. However, in certain systems the calculated electronic specific heat, even after including the effects of band theory, is found to be too small by factors of up to ~ 100 in the most extreme cases, such as in the heavy fermions [3]. In these "highly-correlated" systems, the refusal to address the interactions between electrons themselves is finally untenable. A phenomenological generalization of band theory taking into account the effects of electron-electron interaction was proposed by L.D. Landau [42], known as Fermi liquid theory. The theory assumes that by starting with the excited states of the free electron gas and adiabatically increasing the interaction strength, a one-to-one correspondence is established with the excited states of the interacting system. That such a statement is true is by no means obvious, but here I will take it just as the definition of a Fermi liquid system.

Before proceeding, the language of the non-interacting system will be recast into a new form. It is customary to keep track of the many-body excited states by defining a function $\delta n_k = n_k - n_k^0$ as the difference in occupation of each single particle state ψ_k relative to the ground state. In this notation, the δn_k describing an elementary excitation of one electron promoted from wavevector k_1 to k_2 would be written $\delta n_k = -\delta(k - k_1) + \delta(k - k_2)$. This is convenient bookkeeping, as now the total energy can be written as a functional of the occupation differences:

$$E[\delta n_k] - E_0 = \sum_k \frac{\hbar^2 k^2}{2m} \delta n_k \tag{1.8}$$

Moving to the interacting system, the key piece of intuition from Landau was to postulate that the spectrum of excited states could still be described by δn_k, but with the free electron

states replaced by a new set of effective fermion states with the same charge, spin, and wavevector. The collective behavior of the interacting electrons can then be simplified in terms of these new fermions, dubbed "quasiparticles". Importantly, the one-to-one correspondance with the non-interacting spectrum implies the concept of a Fermi surface is still valid for the quasiparticle distribution. However, the total energy of the interacting system is now no longer additive and will be a complex function of δn_k in general. If δn_k is nonzero only very close to the Fermi surface, however, such as at low temperatures, it can be well approximated by a Volterra series expansion, giving [61]:

$$E[\delta n_k] - E_0 \sim \sum_k \epsilon_k \delta n_k + \frac{1}{2} \sum_k \sum_{k'} f_{k,k'} \delta n_k \delta n_{k'} + \mathcal{O}(\delta n_k^3) \tag{1.9}$$

where ϵ_k is the single quasiparticle energy, and the $f_{k,k'}$ are called Landau interaction parameters. Remember that δn_k now refers to the occupation of quasiparticle states, not electron states. A Fermi velocity and effective mass for the quasiparticles can then be defined in analogy to the free electron, for a spherical Fermi surface this becomes:

$$v_F = \frac{1}{\hbar} \frac{\partial \epsilon_k}{\partial k}\bigg|_{k_F} \tag{1.10}$$

$$m^* = \hbar k_F / v_F \tag{1.11}$$

The effective mass and Landau parameters of a system are taken as phenomenological constants and allow calculation of other physical observables. Intuitively, the sharp discontinuity of the quasiparticle distribution at the Fermi surface will lead to the same qualitative conclusion as the non-interacting case: only quasiparticles within $k_b T$ of the Fermi energy contribute to equilibrium properties. Thus, aside from overall factors associated with m^* and $f_{k,k'}$, predictions for equilibrium quantities should mirror the free electron results. This is illustrated in Table 1.1, which shows a comparison of Fermi liquid calculations with those of free electron theory. While phenomenological, Fermi liquid theory has impressive predictive power. Measurement of, for example, the heat capacity can determine the effective mass alone, constraining all the other equilibrium quantities depending on m^*. Checks of this consistency

have proven Fermi liquid theory to be extremely robust, to the extent that absence of Fermi liquid behavior in a metal is seen as a signature of exotic physics.

1.2 Theory of the Superconducting State

In real materials metallic behavior does not survive to the lowest temperatures. This was first observed in measurements of mercury by Onnes in 1911, who found a phase transition to a state with near perfect conductivity around four Kelvin [36]. This new "superconducting" phase turns out to be a ubiquitous ground state in many different metallic systems. Clearly, near such a phase transition the adiabatic connection to free electron states assumed in Fermi liquid theory must break down in spectacular fashion. This was shown explicitly by Cooper in 1956 [16], who found that adding an arbitrarily small attractive interaction between two electrons near the Fermi energy could stabilize a bound state of the form:

$$\Psi(\mathbf{r_1}, \mathbf{r_2}) = \left[\sum_{k>k_F} \cos(\mathbf{k} \cdot (\mathbf{r_1} - \mathbf{r_2})) \right] \left(|\uparrow\downarrow\rangle - |\downarrow\uparrow\rangle \right) \tag{1.12}$$

where the choice of a singlet spin state allows a symmetric orbital part, maximizing the effect of the attractive interaction [78]. Thus, if the repulsive Coulomb interaction could be overcome in real materials, one would expect the formation of many such "Cooper pair" bound states and a qualitatively new ground state at low enough temperatures. This attractive coupling between electrons turns out to be physically feasible in metals if both the motion of the lattice ions (phonons) as well as the exponential screening of electric charge are considered[1].

A full many-body theory of superconductivity was put forward a year later by Bardeen, Cooper, and Schrieffer starting with the model Hamiltonian (in second-quantized notation) [6]:

$$H_{BCS} = \sum_{k,\sigma=\{\uparrow,\downarrow\}} \epsilon_k c^\dagger_{k,\sigma} c_{k,\sigma} + \sum_{k,k'} V_{k,k'} c^\dagger_{k\uparrow} c^\dagger_{-k\downarrow} c_{-k'\downarrow} c_{k'\uparrow} \tag{1.13}$$

Here ϵ_k is the single particle dispersion relation; in the simplest case this is just the free electron dispersion but can be extended to include the effects of band structure or Fermi liquid renormalizations (in the later case the $c_{k,\sigma}$ would then refer to quasiparticle states

[1]This phonon-mediated interaction is typically assumed in conventional s-wave superconductors. In some unconventional superconductors it is believed that other mechanisms such as coupling to spin fluctuations are important for the pairing.

rather than bare electron states). The second term contains the attractive electron-electron coupling necessary for stabilizing the superconducting state. The BCS Hamiltonian can be solved exactly in the mean-field limit by assuming deviations about the average quantity $b_k = \langle c_{-k\downarrow} c_{k\uparrow} \rangle$ are small. The solution relies on a change of variables to new fermionic creation operators, defined by

$$\gamma_{k0}^\dagger = u_k^* c_{k\uparrow}^\dagger - v_k^* c_{-k\downarrow} \tag{1.14}$$

$$\gamma_{k1}^\dagger = u_k^* c_{-k\downarrow}^\dagger + v_k^* c_{k\uparrow} \tag{1.15}$$

Rewriting the mean-field Hamiltonian in terms of the γ_{k0}, γ_{k1} allows it to be diagonalized by appropriate choice of u_k and v_k, finally resulting in:

$$H_{MF} = H_0 + \sum_k E_k (\gamma_{k0}^\dagger \gamma_{k0} + \gamma_{k1}^\dagger \gamma_{k1}) \tag{1.16}$$

with

$$E_k = (\epsilon_k^2 + |\Delta_k^2|)^{1/2} \tag{1.17}$$

$$\Delta_k = -\sum_{k'} V_{k,k'} b_{k'} \tag{1.18}$$

Consequently, Δ_k is identified as a gap in the excitation spectrum at the Fermi energy, which is qualitatively distinct from the normal metallic state. The temperature dependence of the gap is determined by applying Fermi statistics to the elementary excitations associated with γ_{k0} and γ_{k1}, called Bogoliubov quasiparticles[2]. In the simplest case of a constant potential $V_{kk'} = V_0$ (assumed originally by BCS), the gap becomes isotropic and an approximate analytic solution for $\Delta_0(T)$ can be found near T_c, resulting in [78]:

$$\frac{\Delta(T)}{\Delta(0)} \approx 1.74 \left(1 - \frac{T}{T_c}\right)^{1/2} \tag{1.19}$$

Upon lowering the temperature through the superconducting transition the gap function becomes nonzero and then grows like $\sim (T - T_c)^{1/2}$, characteristic of a second-order mean field

[2]Bogoliubov quasiparticles are distinct from the renormalized electron quasiparticles of the Fermi liquid theory. The term quasiparticle will be used to refer to both concepts when the meaning is clear from context.

phase transition. Evidently $\Delta(T)$ functions as the appropriate order parameter to describe the metal to superconductor phase transition. Thus, superconducting states are typically classified according to the k-space symmetry of their gap function, associating them with the standard atomic labels of s-wave, p-wave, d-wave, etc.[3] The isotropic s-wave gap assumed by BCS successfully describes most superconducting systems, such as elemental superconductors. However, in more exotic, "unconventional" systems such as the high-T_c cuprates, the gap is known experimentally to have a lower $d_{x^2-y^2}$ symmetry. Moreover, due to the requirement of an anti-symmetric fermionic wavefunction, it can be shown that the parity of the gap determines the spin symmetry of the pair wavefunction [70]. Neglecting spin-orbit coupling, even parity gaps (s-wave, d-wave, g-wave, ...) must necessarily be spin singlet, while odd parity gaps (p-wave, f-wave, ...) are spin triplet.

In the original BCS theory only spin-singlet, even parity pairing was considered by construction– the interaction term only acts between electrons with opposite spin. However, in the case of Sr_2RuO_4 the possibility of p-wave *spin-triplet* Cooper pairing will be a main consideration. To include this possibility the theory is generalized by extending the attractive interaction to arbitrary spin:

$$H_{BCS} = \sum_{k,\sigma} \epsilon_k c^\dagger_{k,\sigma} c_{k,\sigma} + \sum_{k,k'\{\sigma_i\}} V_{k,k'\{\sigma_i\}} c^\dagger_{k\sigma_1} c^\dagger_{-k\sigma_2} c_{-k'\sigma_3} c_{k'\sigma_4} \tag{1.20}$$

where $\{\sigma_i\} = \{\sigma_1, \sigma_2, \sigma_3, \sigma_4\}$ and each $\sigma_i = \uparrow$ or $\downarrow$. The mean field approach can be repeated by now expanding about the *four* average quantities $b_{k,\sigma\sigma'} = \langle c_{-k\sigma} c_{k\sigma'} \rangle$. Transforming to the quasiparticle basis again diagonalizes the mean-field Hamiltonian and gives analogous quasiparticle energies but with the scalar gap promoted to a 2x2 matrix describing the pairing in different spin channels [70]:

[3]More generally, when the underlying crystal lattice is considered an s-wave gap refers to an order parameter which respects all the symmetries of the lattice. Equivalently, the gap belongs to an A_{1g} irreducible representation of the crystal point group.

$$\hat{\Delta}_k = \begin{pmatrix} \Delta_{k,\uparrow\uparrow} & \Delta_{k,\uparrow\downarrow} \\ \Delta_{k,\downarrow\uparrow} & \Delta_{k,\downarrow\downarrow} \end{pmatrix} \tag{1.21}$$

For a spin singlet state, the matrix can be parameterized by a single complex function, reducing to the scalar gap function in the previous discussion. However, for a spin triplet state, the gap matrix retains three independent components which form a vector $\mathbf{d_k} = (d_x, d_y, d_z)$ in spin space.

$$\hat{\Delta}_k = \begin{pmatrix} 0 & \Delta_k \\ -\Delta_k & 0 \end{pmatrix} \quad \text{singlet} \tag{1.22}$$

$$\hat{\Delta}_k = \begin{pmatrix} -d_x + id_y & d_z \\ d_z & d_x + id_y \end{pmatrix} \quad \text{triplet} \tag{1.23}$$

Differentiating experimentally between an even parity and odd parity order parameter in Sr_2RuO_4 is one of the main goals of this thesis. A powerful approach is to measure the electronic spin susceptibility, accessible via NMR, for which the theoretical expectations depend crucially on the spin symmetry. The theoretical susceptibility depends on the response of the ground state to applying an infinitesimal magnetic field, which adds a term to the Hamiltonian of the form:

$$H_Z = -\mu_B B_z \sum_k c^\dagger_{k\uparrow} c_{k\uparrow} - c^\dagger_{k\downarrow} c_{k\downarrow} \tag{1.24}$$

where the field is taken to be along z. For a fully gapped singlet superconductor, $|\Delta_k| \gg \mu_B B_z$ at $T = 0$, so the energy cost of breaking a Cooper pair far outweighs the negative contribution from H_Z. Thus, the ground state will be unaffected by the infinitesimal applied field and the spin susceptibility should vanish. The same argument applies for a unitary[4] triplet state with $\mathbf{d} \parallel \mathbf{B}$ over the entire Fermi surface, as the gap matrix is again off-diagonal. However, if the

[4]A unitary state satisfies $|\mathbf{d} \times \mathbf{d}^*| = 0$, i.e. the real and imaginary parts are colinear. In this case the magnitude of the energy gap is just given by $|\mathbf{d}|$. Unitary states are generally energetically favorable in the absence of symmetry breaking fields [51] and will be assumed here.

d-vector is fixed such that $\mathbf{d} \perp \mathbf{B}$, the spin of the triplet pairs is parallel to the applied field and there is no competition between spin polarization and pair formation. In this case the spin susceptibility will be identical to that of the normal state. At finite temperatures the calculation is more involved, with the result that the spin susceptibility in the off-diagonal case (assuming a full gap) will vanish exponentially as $T \to 0$ [83]. If the gap has nodes at points or lines on the Fermi surface the susceptibility at $T = 0$ is unchanged, but will in general have polynomial rather than exponential dependence on temperature. A summary of this behavior is given in Figure 1.3 and will be crucial in interpreting the NMR results on the superconducting state of Sr_2RuO_4.

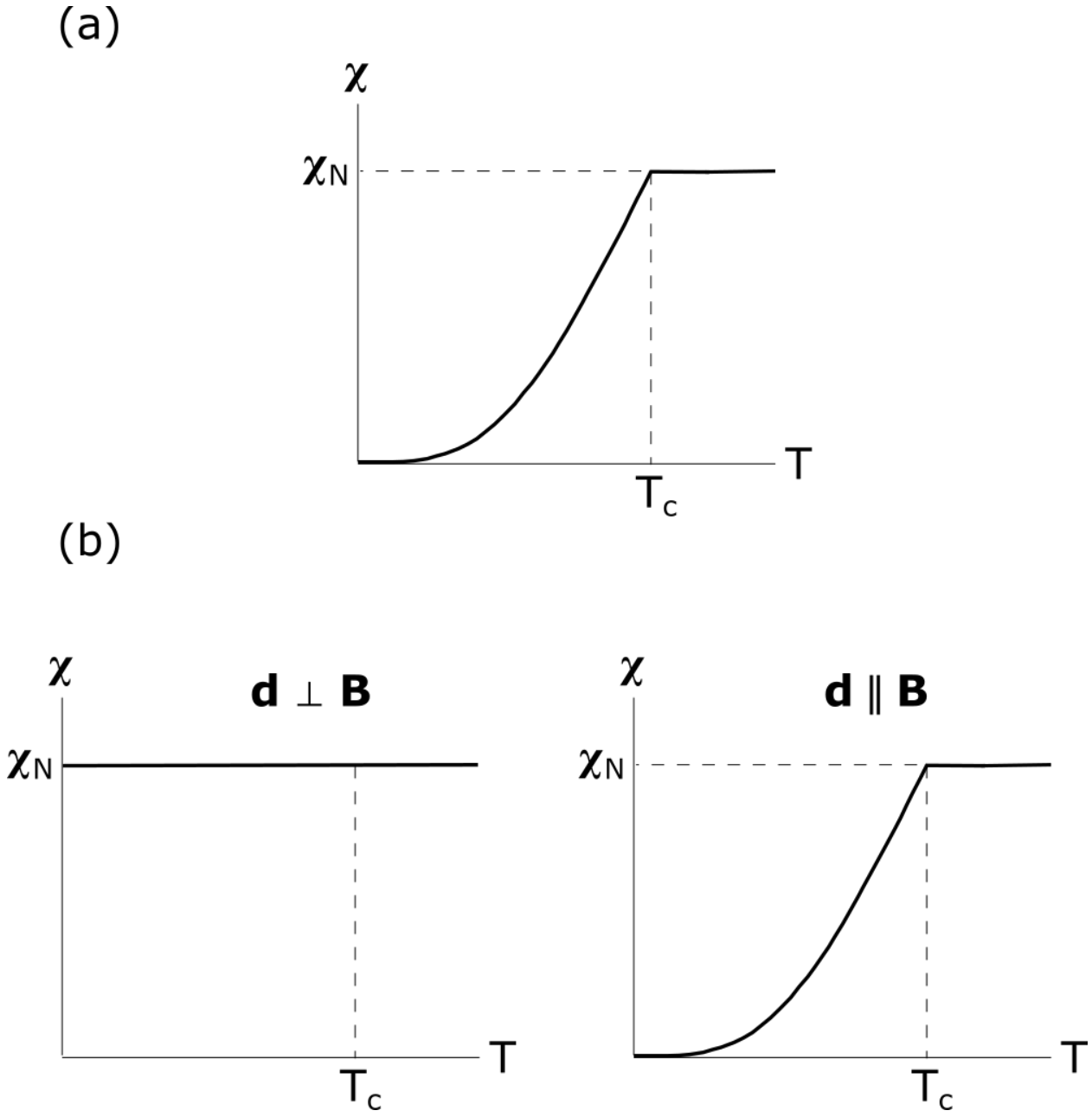

Figure 1.3: (**a**) Spin susceptibility of a fully gapped singlet superconductor. The susceptibility vanishes exponentially for all field directions at low temperatures according to the Yosida function [83]. (**b**) Spin susceptibility of a fully gapped triplet superconductor with fixed d-vector. For $\mathbf{d} \parallel \mathbf{B}$ the susceptibility vanishes exponentially, while for $\mathbf{d} \perp \mathbf{B}$ it is equal to that of the normal state.

CHAPTER 2

Physics of Sr_2RuO_4

2.1 Motivation

Sr_2RuO_4 is the cleanest and most well-characterized unconventional superconductor known to condensed matter physicists. In fact, the fermiology of the normal state is known to a level of precision that rivals even conventional elemental superconductors. Despite this, however, a successful theoretical understanding of the ground state has eluded researchers for more than two decades now. Thus, achieving a full understanding of the physics of Sr_2RuO_4 is a critical milestone in the study of unconventional superconductivity as a whole.

Originally, Sr_2RuO_4 was notable due to its connection to the high temperature cuprate superconductors, having the same layered oxide perovskite crystal structure but with Copper replaced by ruthenium. It was seen as an opportunity to study an analogous superconducting system without the large amounts of disorder found in the cuprates. However, the results of early investigations found a qualitatively different type of superconductor. Sr_2RuO_4 is superconducting in its stoichiometric form and has a quite small T_c of only ~ 1.5K. The superconducting state also emerges out of a robust Fermi liquid, in contrast to the anomalous normal state of the cuprates. Quantitative comparison of the Fermi liquid parameters to that of ^{3}He then led to the exciting proposal by Sigrist and Rice that the superconducting state of Sr_2RuO_4 could be a quasi-2D electronic analog to spin-triplet superfluid ^{3}He [64]. This positioned Sr_2RuO_4 as an exotic quantum material in its own right and interpretations of early experiments corroborated the idea [33, 19, 45]. As a result, Sr_2RuO_4 was widely

accepted as the paradigmatic example of odd parity superconductivity for the next twenty years. However, the new NMR experiments detailed in this thesis challenge this longstanding interpretation. The superconductivity is instead demonstrated convincingly to be *even* parity, ruling out all pure odd parity pairing states.

Moreover, even without consideration of the superconducting state, the normal metal phase of Sr_2RuO_4 is an interesting strongly correlated, multi-band system. These interactions create effective masses 3-5 times the band mass depending on the Fermi surface [52, 8], but despite these strong correlations Sr_2RuO_4 behaves like a textbook Fermi liquid below about ~ 30K [55, 29, 30]. Additionally, the extraordinarily well-characterized normal state, with direct experimental measurements of the Fermi surface topology, quasiparticle masses, Fermi velocities, etc., makes it a perfect testing ground for theories of interacting electrons. The material is also highly two-dimensional, with the Fermi energy in close proximity (~ 13meV) to a van Hove singularity (vHs) in the density of states at the Brillouin zone boundary [68]. This fact, along with new uniaxial stress techniques, has enabled in-situ tuning of the Fermi level across the vHs and direct observation of the effect of a singular density of states on a strongly correlated metal [74, 5, 76, 46].

The rest of this chapter will review the experimental work done on Sr_2RuO_4 most important for the interpretation of our NMR results.

2.2 Normal State

2.2.1 Crystallography and Band Structure

The crystal structure of Sr_2RuO_4 is shown in Figure 2.1. It consists of RuO_2 planes arranged in a square lattice separated by SrO layers, forming a perovskite structure analogous to the cuprate parent compound $LaCu_2O_4$. The ruthenium ions have a formal charge of 4+, leaving four electrons to populate the three low lying t_{2g} d-orbitals, which are split from the e_g orbitals by the octahedral crystal field. These hybridize with the oxygen p-orbitals to form one quasi-2D band with d_{xy} character and two quasi-1D bands with $d_{xz,yz}$ character. Due to the large interplane distance, all three bands have weak k_z dependence and form sheets that are open along the z direction of the Brillouin zone. Figure 2.2 shows the shape of the three fermi surface sheets determined from quantum oscillations experiments, as well as a level cut of the Fermi surface at $k_z = 0$ determined from angle resolved photo-emission (ARPES) measurements [8, 77].

2.2.2 Fermi Liquid Parameters

The emergence of a low temperature Fermi liquid is verified by multiple bulk thermodynamic probes. Below $T_{FL} \sim 30$K, quadratic variation with temperature is observed in the resistivity for both in-plane and out-of-plane directions [29, 55], an important prediction of coherent transport in a Fermi liquid. A typical $\gamma_e T + \beta T^3$ variation in the specific heat is also found at low temperatures [55]. Most importantly for this work, NMR measurements observe a shallow maximum in the Knight shift near T_{FL} before leveling off [30], indicative of a temperature independent spin susceptibility.

Another signature of the Fermi liquid is the presence of quantum oscillations in the magnetization (de Haas-van Alphen effect) and resistivity (Shubnikov-de Haas effect) at low temperatures, associated with quasiparticle Landau levels passing through the Fermi Energy.

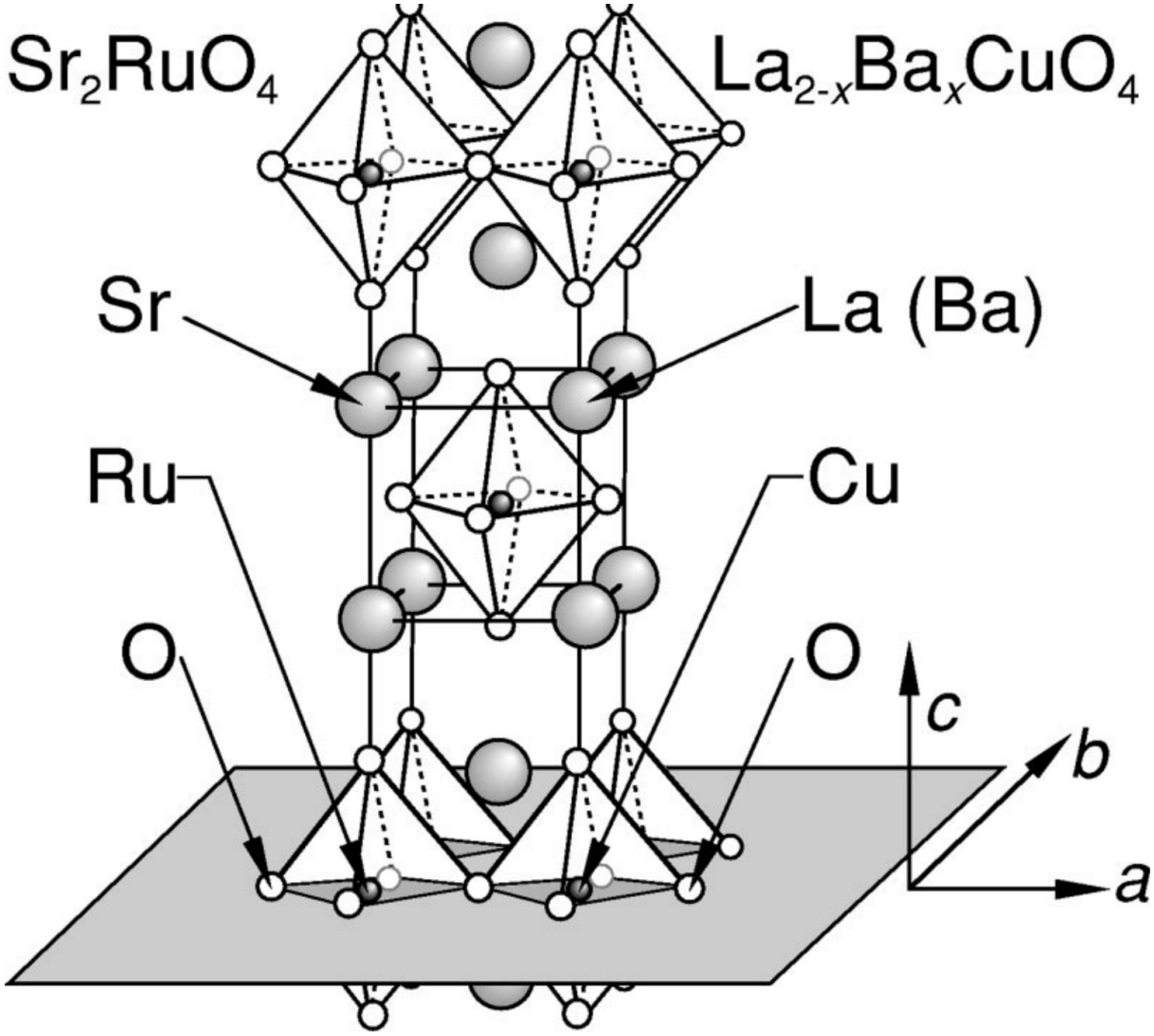

Figure 2.1: Sr_2RuO_4 crystal structure compared to that of LBCO. There are two distinct oxygen sites in the unstrained material. The apical oxygen above and below the ruthenium is labeled O(2) while the oxygen of the RuO_2 layers is labeled O(1). Reproduced from [54].

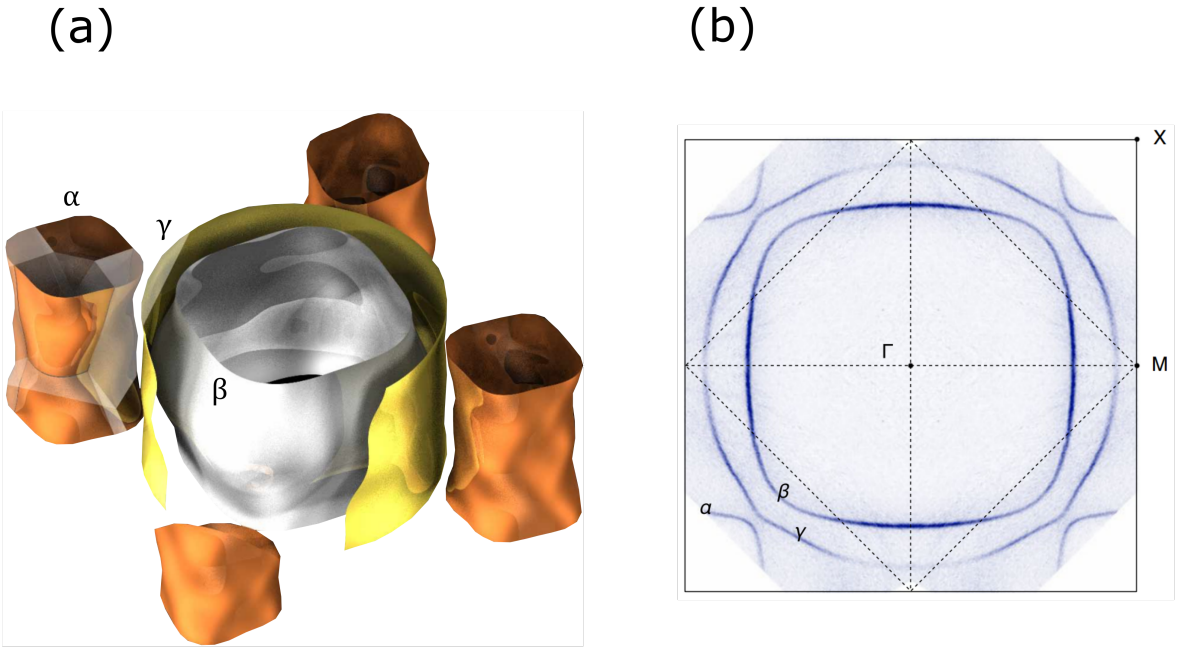

Figure 2.2: **(a)** Fermi surface of Sr_2RuO_4 constructed from quantum oscillation data. The quasi-1D $d_{xz,yz}$ bands hybridize to form two open sheets (α, β) with roughly square cross section, while the quasi-2D d_{xy} sheet (γ) is almost cylindrical. The z-axis warping of the each sheet is exaggerated by a factor of 15. Reproduced from [8] **(b)** Two dimensional slice of the Fermi surface at $k_z = 0$ measured via ARPES. Reproduced from [77].

The extremely low disorder achievable in single crystals have allowed these oscillations to be precisely measured [53, 50]. As such, the quasiparticle parameters of the three bands are known in great detail [8]. Independent measurements of the quasiparticle dispersions from angle resolved photoemmision (ARPES) data [17, 68, 77] also agree well with the results from quantum oscillations. Selected quasiparticle parameters are shown in Table 2.1, reproduced from [51], where m^* is the measured thermodynamic cyclotron mass from dHvA. The m^* are seen to be strongly enhanced over values obtained from band structure calculations which do not take into account electron correlations [57]. The measured Fermi wavevectors are also shown, defined as $k_F = \sqrt{A/\pi}$ where A is the cross section of the Fermi sheet.

Fermi Surface Sheet	α	β	γ
character	hole-like	electron-like	electron-like
$k_F(\text{Å}^{-1})$	0.304	0.622	0.753
$m^*(m_e)$	3.3	7.0	16.0
m^*/m_{band}	3.0	3.5	5.5

Table 2.1: Quasiparticle parameters for Sr_2RuO_4, reproduced from [51]. Quantities are defined in the text.

2.2.3 Proximity to Magnetism

A close structural relative, $SrRuO_3$, is known to have a ferromagnetic ground state [14]. Ferromagnetic fluctuation were thought to be important in Sr_2RuO_4 as well, which would be expected to stabilize an odd parity superconducting order parameter. However, inelastic neutron scattering experiments have found the dominant spin fluctuations are actually antiferromagnetic, with $\mathbf{q_0} \approx (0.6\pi, 0.6\pi)$ corresponding to the incommensurate nesting wavevector of the quasi-1D Fermi surfaces [69, 73]. However, a smaller broad peak near $\mathbf{q} = 0$ has also been resolved [73]. Recently, evidence for a magnetic phase stabilized by applied uniaxial stress was reported in μSR measurements [21]. The magnetic signal is interpreted in

terms of an incommensurate spin density wave, but there has been no direct confirmation of the ordering wavevector.

2.2.4 Effect of Uniaxial Stress

The detailed experimental knowledge of the Fermi surface outlined above allow for very precise band structure calculations. A common feature of these calculations particularly important for this work is the appearance of van Hove singularities (vHs) in the density of states at the Brillouin zone boundary along the (100) and (010) directions. Intuitively, this is analogous to the vHs in a simple tight binding model on the square lattice. Moreover, tuning of the Fermi energy via Lanthanum doping has found E_F of the stoichiometric material to be only $\sim$ 13meV below the vHs energy [68]. This is close enough proximity that distorting the in-plane lattice via uniaxial stress can warp the γ band enough to pass through the singularity at the zone boundary [74, 76]. This zone boundary crossing also leads to a Lifshitz transition, where the connectivity of the Fermi surface sheet changes from closed to open. This has been confirmed directly via ARPES experiments performed under strained conditions, as shown in Figure 2.3. Tuning the applied stress so that E_F coincides with the vHs singularity is associated with remarkable changes in many physical properties, such as more than doubling of the superconducting critical temperature [74], as well as deviations from standard Fermi liquid transport behavior [5].

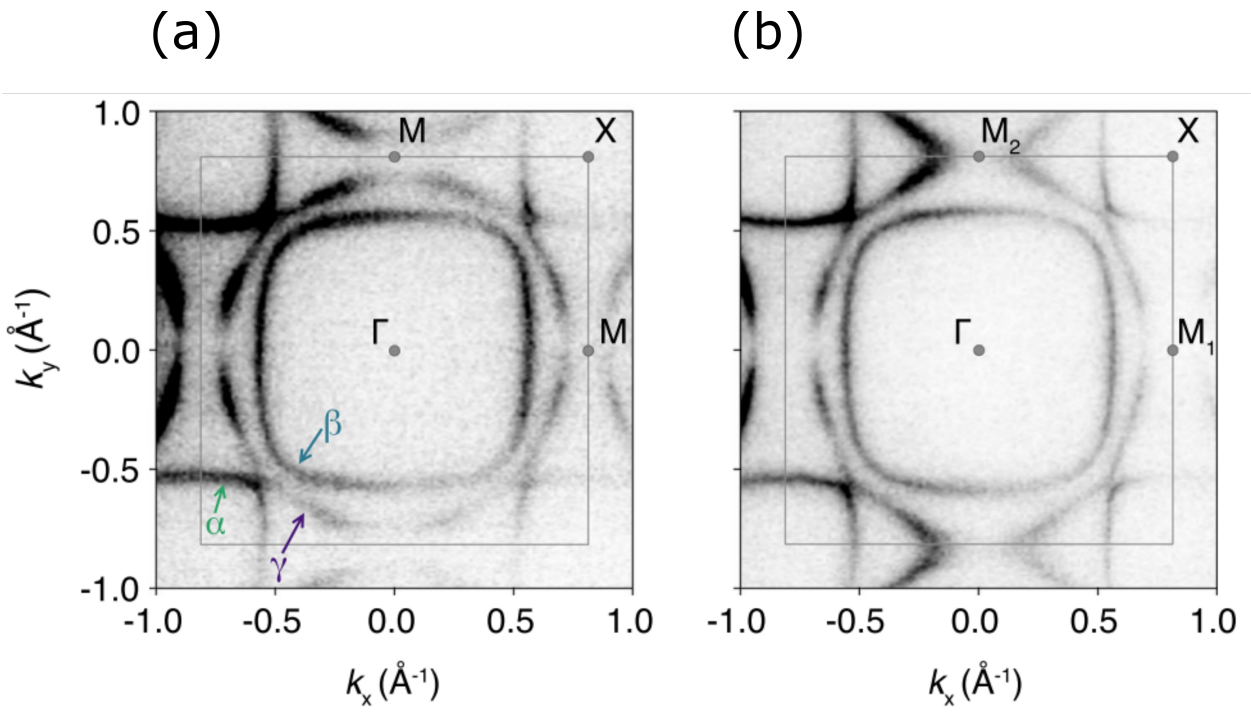

Figure 2.3: ARPES measurement of a $k_z = 0$ slice of the Fermi surface under **(a)** unstrained conditions as well as **(b)** applied uniaxial stress corresponding to an anisotropic strain of $\epsilon_{xx} - \epsilon_{yy} = -0.7\%$. Reproduced from [76].

2.3 Superconducting State

2.3.1 Superconducting Parameters

High quality single crystals of Sr_2RuO_4 undergo a superconducting transition at around $T_c = 1.5$K, while the thermodynamic critical field estimated from heat capacity data [60] is approximately $B_c \sim 0.02$T. However, the upper critical fields observed directly via transport are larger and highly anisotropic with $B_{c2||ab}(T = 0) = 1.5$T for fields orientated in the plane of the oxide layers, while $B_{c2||c}(T = 0) = 0.075$T for fields perpendicular to the layers [2]. This corresponds to dimensionless Ginzberg-Landau parameters $\kappa_{ab,c} = \frac{1}{\sqrt{2}}\frac{B_{c2||c,ab}}{B_c}$ [78] of ~ 2.5 for $B||c$ and ~ 50 for $B||ab$. As such, for in-plane fields Sr_2RuO_4 is strongly type-II, while for out-of-plane fields it is modestly so. The coherence lengths ξ_i and penetration depths λ_i for each crystallographic direction can also be calculated from the critical fields, assuming orbital-limiting [78]. These parameters are collected in Table 2.2, reproduced from [51]. However, it should be noted that the superconducting transition is actually first-order for fields aligned precisely in-plane [82] and $T < 0.8$K, contrary to the expectation for an orbitally limited type-II superconductor.

Parameter		ab	c
$B_{c2\|\|c}(0)$ (T)	0.075		
$B_{c2\|\|ab}(0)$ (T)	1.50		
B_c (T)	0.023		
$\xi(0)$ (Å)		660	30
$\lambda(0)$ (Å)		1520	30000
$\kappa(0)$		2.3	46
$\gamma(0) = \xi_{ab}(0)/\xi_c(0)$	20		

Table 2.2: Ginsberg-Landau Parameters for Sr_2RuO_4, Reproduced from [51].

2.3.2 Symmetry Allowed Pairing States

In the case of a conventional s-wave gap, the superconducting transition breaks only U(1) gauge symmetry. However, unconventional states (p-wave, d-wave, etc.) will also break symmetries of the lattice. This symmetry breaking can be precisely classified according to the irreducible representations of the underlying crystal point group. Sr_2RuO_4 is a member of the tetragonal D_{4h} point group, which admits 10 distinct irreducible representations for the superconducting order parameter [35]. These representations are listed in Table 2.3 along with example order parameters and expectations for their physical properties.

Irr. Rep.	Gap Function	Ang. mom.	Spin	Nodes	TRSB
A_{1g}	$\psi = 1$	s-wave	0	None	No
A_{2g}	$\psi = k_x k_y (k_x^2 - k_y^2)$	g-wave	0	Vertical	No
B_{1g}	$\psi = k_x^2 - k_y^2$	d-wave	0	Vertical	No
B_{2g}	$\psi = k_x k_y$	d-wave	0	Vertical	No
E_g	$\psi = k_z(k_x \pm ik_y)$	d-wave	0	Horizontal	Yes
A_{1u}	$\mathbf{d} = \hat{\mathbf{x}}k_x + \hat{\mathbf{y}}k_y$	p-wave	1	None	No
A_{2u}	$\mathbf{d} = \hat{\mathbf{x}}k_y - \hat{\mathbf{y}}k_x$	p-wave	1	None	No
B_{1u}	$\mathbf{d} = \hat{\mathbf{x}}k_x - \hat{\mathbf{y}}k_y$	p-wave	1	None	No
B_{2u}	$\mathbf{d} = \hat{\mathbf{x}}k_y + \hat{\mathbf{y}}k_x$	p-wave	1	None	No
E_u	$\mathbf{d} = \hat{\mathbf{z}}(k_x \pm ik_y)$	p-wave	1	None	Yes
	$\mathbf{d} = k_z(\hat{\mathbf{x}} \pm i\hat{\mathbf{y}})$	p-wave	1	Horizontal	Yes

Table 2.3: Symmetry classified order parameters for Sr_2RuO_4.

2.3.3 Disorder Sensitivity

The superconductivity of Sr_2RuO_4 is extremely sensitive to disorder and impurities, with residual resistivities of only $\sim 1\mu\Omega$cm enough to destroy it entirely [48]. Furthermore, the

impurities were shown to be non-magnetic, judging from the lack of line broadening in NMR or NQR [31]. This behavior is not consistent with a conventional s-wave superconductor, as the effect of impurity scattering is to average the gap around the fermi surface, leaving it essentially unchanged [1]. For higher order angular momentum pairing, however, the gap average must be zero by symmetry, so scattering will destroy the superconductivity. The observed impurity effect is thus strong evidence for an unconventional superconducting ground state. Quantitatively, the remarkably stringent purity criterion can be understood considering the massive in-plane coherence length, which is over 60 times that of typical cuprate superconductors [56]. The pair wavefunction extends over hundreds of unit cells and requires a correspondingly long mean free path to remain in the clean limit (cuprate pair wavefunctions contain only a few unit cells, allowing them to remain superconducting even after heavy doping).

2.3.4 Spin Susceptibility

Both NMR Knight shift and polarized neutron scattering experiments initially reported no change in the spin susceptibility between the normal and superconducting states for in-plane applied field [33, 19]. This result is inconsistent with an even parity order parameter (such as s-wave or d-wave), where the Pauli susceptibility must compete with the condensation energy of the Cooper pairs. The spin susceptibility should instead vanish at low temperatures and fields, a qualitatively different result. These experiments were interpreted as confirming unconventional odd parity superconductivity in Sr_2RuO_4. In particular, a constant susceptibility is possible only if the vector order parameter is perpendicular to the applied field, as discussed in Chapter 1.2. Given the possible symmetry allowed states, these reports were consistent only with the $\mathbf{d} = \hat{\mathbf{z}}(k_x \pm ik_y)$ (E_u) "chiral p-wave" state, a superconducting analog to the ABM phase in superfluid Helium-3. If accurate, this is lynch-pin evidence for odd parity superconductivity– it would be difficult to rationalize this behavior for any even parity order parameter. However, the work presented in this thesis contradicts these reports

and shows the behavior of the spin susceptibility is in fact incompatible with odd parity superconductivity.

2.3.5 Gap Nodes and Minima

The existence of low energy excitations corresponding to nodes or deep minima in the superconducting gap was confirmed early on by multiple experimental probes [60, 47, 12, 32, 18]. However, conclusions about the specific nodal structure of the gap have been inconsistent. Thermal conductivity measurements reported evidence for nonzero c-axis quasiparticle velocity at zero temperature, implying horizontal line nodes [23]. However, specific heat measurements found a four-fold oscillation as a function of in-plane field, which did not change sign at the lowest temperatures [38]. They concluded this was evidence for *vertical* line nodes, contrary to the interpretation of a previous specific heat measurement [18]. Most recently, quasiparticle interference measurements corroborated evidence for vertical line nodes, finding nodes along the $(k_x, k_y) = (\pm\frac{\pi}{a}, \pm\frac{\pi}{a})$ directions [67].

2.3.6 Multi-component Superconductivity

Signs of time reversal symmetry breaking (TRSB) have been observed in both muon spin relaxation (μSR) [45] and polar Kerr effect measurements [80]. This has strong implications on the superconducting state as it can be explained only by an order parameter with a two-dimensional irreducible representation (multi-component). Historically, this was supporting evidence for the chiral p-wave order parameter, which is multi-component and should exhibit TRSB. The μSR signal proved to be robust and was reproduced by another group [21] who found that the TRSB temperature splits from T_c under in-plane strain. Two recent ultrasound experiments using different techniques have also confirmed multi-component superconductivity [20, 7] by resolving a jump in the C_{66} elastic modulus, which is forbidden by symmetry for a single component state. The reproducibility and variety of these experiments

suggest that a successful theory of superconductivity in Sr_2RuO_4 must account for a multi-component order parameter.

2.3.7 Chiral p-wave as the candidate OP

Before the results presented in this thesis, the chiral p-wave state with $\mathbf{d} = \hat{\mathbf{z}}(k_x \pm k_y)$ was the most widely accepted proposal for the superconducting order parameter. It was unconventional with d-vector along the crystal c-axis, explaining the impurity sensitivity and apparently constant spin susceptibility for in-plane fields. The state was also multi-component and broke time-reversal symmetry. Additionally, it lined up well as an analog to the A-phase of spin triplet superfluid Helium-3. However, there were already serious problems with this interpretation. First, the superconducting transition at low temperatures was first-order for in-plane field and $B_{c2}(T \to 0)$ was smaller than expected, both indicating Pauli spin limiting. This is a worrying observation as a triplet order parameter with $\mathbf{d} \parallel c$ should have no such limiting for the same reasons that lead to constant susceptibility [49]. Furthermore, the $\mathbf{d} = \hat{\mathbf{z}}(k_x \pm k_y)$ state has no symmetry protected nodes, contrary to the strong evidence for excitations surviving to zero temperature. Explaining this would require accidental gap nodes or extremely deep gap minima. Another cause for concern was the inability to detect edge currents that were expected for a chiral state [26] or a cusp in the superconducting transition temperature under strain [25]. These inconsistencies warranted continual experimental interest in Sr_2RuO_4 and motivated the use of NMR spectroscopy coupled with applied stress detailed in the following chapters.

CHAPTER 3

Experimental Methods

3.1 Pulsed NMR Methods

3.1.1 Basic Principles

Nuclear magnetic resonance measurements rely on manipulating the spin angular momentum of atomic nuclei. Because the nucleus is charged, this intrinsic angular momentum creates a proportional magnetic moment according to its gyromagnetic ratio:

$$\boldsymbol{\mu} = \gamma_n \mathbf{I} \tag{3.1}$$

This magnetic moment will then interact with magnetic fields via the Zeeman Hamiltonian. For an isolated spin:

$$H_Z = -\boldsymbol{\mu} \cdot \mathbf{B} = -\gamma_n \mathbf{I} \cdot \mathbf{B} \tag{3.2}$$

Conveniently, the quantum mechanical equations of motion for the expectation value of $\boldsymbol{\mu}$ are identical to the classical solution for a magnetic moment interacting with a field [71], specifically

$$\frac{d\langle \boldsymbol{\mu} \rangle}{dt} = \langle \boldsymbol{\mu} \rangle \times \gamma_n \mathbf{B} \tag{3.3}$$

For a time independent field the solution is straightforward. The component of $\langle \boldsymbol{\mu} \rangle$ perpendicular to $\mathbf{B}$ will rotate at an angular frequency $\omega = \gamma_n B$, called the Larmor precession frequency. Moreover, if the system is expanded to include N non-interacting spins, then

the total magnetic moment $\mathbf{M} = N\langle\boldsymbol{\mu}\rangle$ will behave similarly. This is the crux of the NMR technique: by applying a large external magnetic field $\mathbf{B_0}$ to the sample, a *macroscopic* precession of magnetic moment can be measured experimentally.

However, in equilibrium, $\mathbf{M}$ will tend to align parallel with the applied field, so it must somehow be rotated away from $\mathbf{B_0}$ in order to observe a Larmor precession. This is accomplished by placing the sample in a wire solenoid oriented perpendicular to the external field. Defining $\mathbf{B_0} \parallel \hat{\mathbf{z}}$, the field of the solenoid can be written $\mathbf{B_1} = 2B_1\cos(\omega_c t)\hat{\mathbf{x}}$. Here ω_c is the carrier frequency of the voltage applied across the solenoid. Solving Equation 3.3 in this case is not trivial, but can be simplified by moving into a reference frame rotating at frequency ω_c about $\hat{\mathbf{z}}$. The trick is to rewrite the solenoid field oscillating along $\hat{\mathbf{x}}$ as a superposition of two oppositely rotating fields:

$$\mathbf{B_1} = B_1(\hat{\mathbf{x}}\cos(\omega_c t) + \hat{\mathbf{y}}\sin(\omega_c t)) + B_1(\hat{\mathbf{x}}\cos(\omega_c t) - \hat{\mathbf{y}}\sin(\omega_c t)) \tag{3.4}$$

In the rotating frame, one of these components will become static while the other will have its frequency doubled. Neglecting the frequency doubled component[1], the equation of motion in the rotating frame becomes

$$\frac{d\mathbf{M}}{dt} = \mathbf{M} \times [(-\omega_c + \gamma_n B_0)\hat{\mathbf{z}} + \gamma B_1 \hat{\mathbf{x}}] \tag{3.5}$$

Where the $(\mathbf{M} \times -\omega_c\hat{\mathbf{z}})$ term is needed to account for the time dependence of the new frame's basis vectors. Finally, if one chooses the carrier frequency such that $\omega_c = \gamma_n B_0$ only the term along $\hat{x}$ will remain, meaning $\mathbf{M}$ precesses around the *x-axis* in the rotating frame. As such, by applying voltage pulses with this frequency to the solenoid coil, the sample's magnetic moment can be rotated any desired angle away from the external field. The requisite frequency $\omega_0 = \gamma_n B_0$ is called the NMR resonance frequency. The basic steps of a pulsed NMR measurement can now be laid out. First, the sample is placed inside a wire coil arranged

[1]The magnitude of B_1 is much smaller than B_0 in practice so $2\omega_c \gg \gamma_n B_1$. The field component rotating at $2\omega_c$ thus traverses the xy-plane many times before $\mathbf{M}$ changes appreciably. Its net effect on $\mathbf{M}$ is negligible as a result.

perpendicular to a large external field. Then, an alternating voltage with carrier frequency ω_0 is applied to the wire coil in order to rotate the macroscopic magnetization away from the external field. Finally, the applied voltage is switched off and the Larmor precession is measured via an induced voltage in the same wire coil.

In this simple treatment, once the nuclear magnetization is manipulated into the xy-plane, it precesses indefinitely. In reality, coupling of the nuclear spins to the lattice as well as each other will tend to return the system to equilibrium. While the microscopic details of this process can be complicated, a phenomenological description by Bloch [10] introduces two relaxation times T_1 and T_2 to the equations of motion, which describe the return to equilibrium of the z and xy magnetization respectively:

$$\frac{dM_x}{dt} = \frac{M_x}{T_2} + \gamma(\mathbf{M} \times \mathbf{B})_x \tag{3.6}$$

$$\frac{dM_y}{dt} = \frac{M_y}{T_2} + \gamma(\mathbf{M} \times \mathbf{B})_y \tag{3.7}$$

$$\frac{dM_z}{dt} = \frac{M_0 - M_z}{T_1} + \gamma(\mathbf{M} \times \mathbf{B})_z \tag{3.8}$$

T_1 processes represent an exchange of energy of the nuclear spin system with the environment and are referred to as "spin-lattice relaxation". T_2 processes describe the loss of coherence of the precessing spins in the xy-plane, called "spin-spin relaxation". Both of these timescales are accessible experimentally by measuring the time evolution of the nuclear magnetization.

3.1.2 Pulse sequences

3.1.2.1 Free Induction Decay

The simplest NMR pulse sequence is a free induction decay (FID) measurement. Here, a single radiofrequency (RF) pulse is applied to the sample coil and the induced voltage (free induction) signal is recorded immediately afterwards, just as described in the previous section. A "$\frac{\pi}{2}$-pulse" is typically used, where the duration of the pulse $d_{\frac{\pi}{2}}$ is chosen such that $\mathbf{M}$ is rotated $\pi/2$ radians away from the z-axis defined by the external field. This

maximizes the change in magnetic flux through the cross section of the NMR coil from the Larmor precession. Using Equation 3.5, with the carrier frequency exactly on resonance, this condition is satisfied when $d_{\frac{\pi}{2}}\gamma_n B_1 = \frac{\pi}{2}$. For off-resonance signals, the effective field in the rotating frame is tilted away from the xy-plane according to the ratio of γB_1 to $\omega - \omega_c$, which constrains the bandwidth of measurable frequencies. The magnitude of B_1 can be adjusted by tuning the amplitude of the RF pulse, and is typically chosen such that $d_{\frac{\pi}{2}} \sim 1\mu$s. However, in the experiments on the superconducting state of Sr_2RuO_4 described later, it is found that standard $\pi/2$ pulses introduce too much incident energy to the sample. Thus, it was necessary to perform FID experiments using smaller B_1 fields and lower pulse durations, leading to correspondingly small magnetization tip angles.

3.1.2.2 Spin Echo

The FID signal from a single pulse can be extremely short lived, owing to inhomogeneity of the applied external field in a real experiment. In this case, the precession frequency of nuclei in different parts of the sample are not identical and the phase coherence of $\mathbf{M}$ in these regions is lost on timescales of order $\sim 50 - 100$ μs. This is a serious problem in practice, because the high power RF incident on the sample circuit cannot be perfectly isolated from the signal receiver. As a result the preamplifiers before the receiver (see Chapter 3.1.4 for details) will be saturated for a substantial dead time relative to the FID duration. This is especially problematic when signal-to-noise is a constraint, because the FID signal strength decays exponentially in time. To circumvent these issues, a spin echo or Hahn echo is employed, named after its discovery by Erwin Hahn in 1950 [22]. By applying a π-pulse t_1 seconds after the initial $\frac{\pi}{2}$-pulse the magnetization will be reflected across the x or y axis of the rotating frame, depending on the phase of the second pulse. In either case, after waiting another t_1 seconds, the magnetization of the inhomogeneously broadened parts of the sample refocuses and precesses together before finally dephasing again. This refocusing results in a revival of the NMR signal $2t_1$ seconds after the initial $\frac{\pi}{2}$-pulse. A schematic of the rephasing of $\mathbf{M}$ by

a spin echo pulse sequence is show in Figure 3.1 **(b)**. This procedure allows the detection of NMR signal at the spin echo formation, which is separated in time from the firing of the high power RF pulses.

3.1.3 RF Power Transmission

Typical resonance frequencies for a commercial NMR magnet lie within the radiofrequency range of 10-100MHz. As such, successfully transmitting power to the sample coil, which can be meters away from the driving source, requires a resonant tank circuit that is appropriately matched with the source impedance. Ideally this is done with reactive matching elements placed as close to the sample coil as possible. Such an arrangement maximizes the quality factor of the resonant circuit. However, for experiments covering a wide range of applied fields or with limited mechanical access to the sample chamber (such as in a dilution refrigerator), a top-tuning configuration is required. In this setup the reactive elements are placed outside of the experimental cryostat with some length of transmission line leading to the sample coil, illustrated in Figure 3.2. This will lower the quality factor but allows much more freedom in swapping out the reactive elements in order to match desired frequencies. The optimal reactance values for power transfer can then be calculated using standard transmission line theory. The input impedance of a lossless line of length ℓ terminated by sample coil of inductance L and resistance r is given by :

$$Z_e = \frac{(r + i\omega L) + iZ_0 \tan(2\pi\ell/\lambda)}{Z_0 + i(r + i\omega L)\tan(2\pi\ell/\lambda)} \tag{3.9}$$

where Z_0 is the characteristic impedance of the line and λ is the wavelength at frequency ω. The total impedance of the tank circuit presented to the RF transmitter, including the reactive elements outside the cryostat, is then:

$$Z_{tank}(\omega) = \frac{1}{i\omega C_1} + \frac{1}{i\omega C_2}//Z_e \tag{3.10}$$

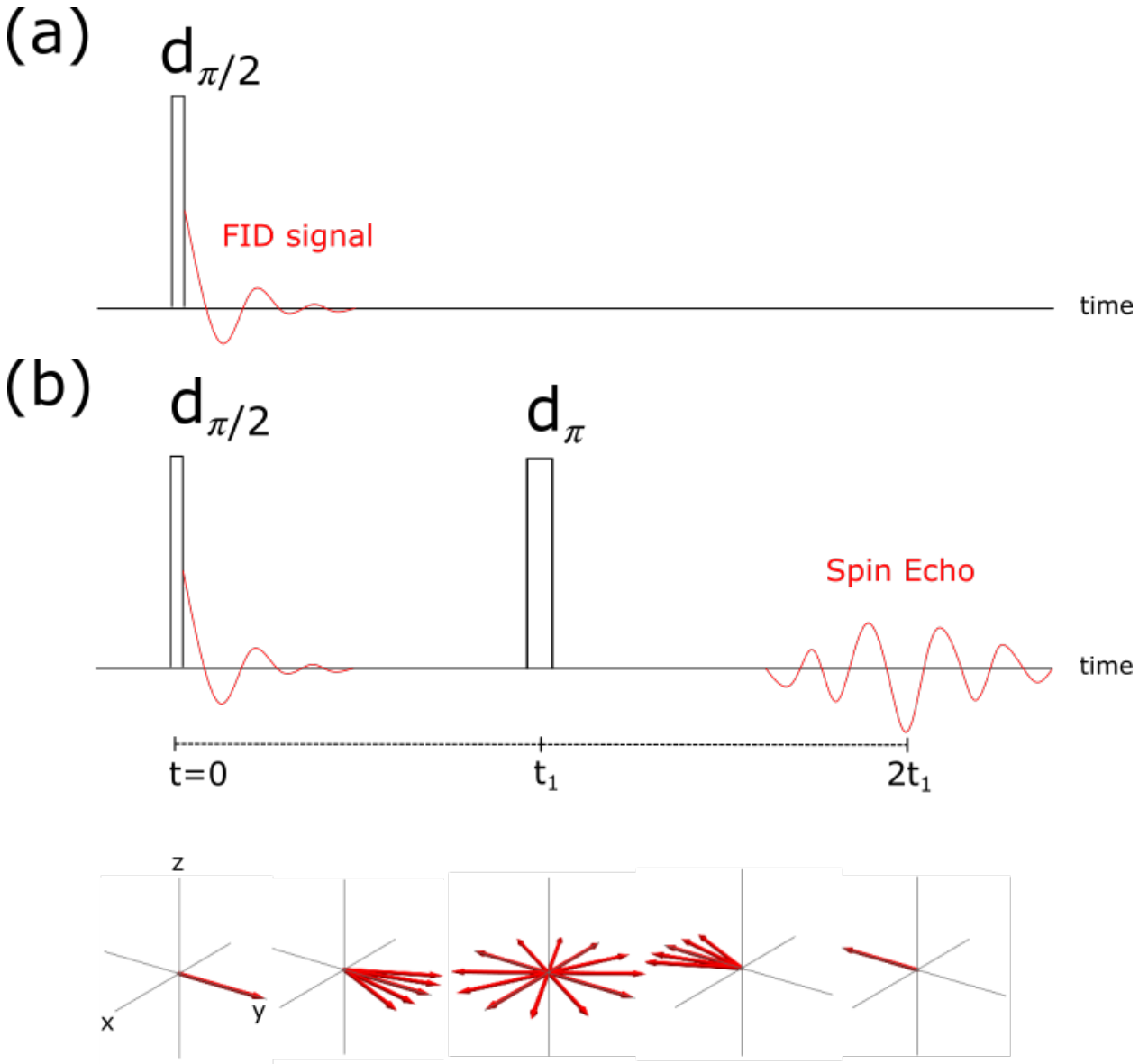

Figure 3.1: **(a)** NMR free induction decay (FID) pulse sequence. The NMR signal is collected directly after a single $\frac{\pi}{2}$ pulse of arbitrary phase. **(b)** Example NMR Spin echo pulse sequence using two x-phase pulses. After the initial $\frac{\pi}{2}$-pulse, the nuclear magnetization is aligned along the y-axis of the rotating frame but quickly loses coherence in the case of inhomogenous fields. A time t_1 later, a π-pulse is used to reflect all the spins across the x-axis. Finally, the magnetization is refocused along the negative y-axis at a time $2t_1$ following the first pulse. This evolution of the nuclear spins is sketched below the pulse sequence.

In order to maximize the power transmission, we look for a tank impedance such that:

$$\Gamma = \frac{Z_{tank} - Z_0}{Z_{tank} + Z_0} = 0 \tag{3.11}$$

where Γ is the reflection coefficient. This can be satisfied for any desired carrier frequency ω_0 by choosing the values of C_1 and C_2 such that $Z_{tank}(\omega_0) = Z_0$.

3.1.4 Spectrometer

The full experimental measurement circuit including both pulse transmission and signal detection is shown Figure 3.3. First, a low power continuous wave (CW) RF source is cut into microsecond length pulses with phase shifters allowing for selection of four different pulse phases ($+x$,$+y$,$-x$,$-y$). This is then directed to a 100W RF amplifier in series with resistive attenuators to produce a typical 10-20W NMR pulse. A duplexer consisting of two double diodes and a $\lambda/4$ cable ensures the high amplitude RF is incident only on the sample, while the resulting low amplitude NMR signal is directed to the receiver. The signal is then amplified and mixed with two 90° components of the original CW source for down-conversion and quadrature detection. For appropriate choice of carrier frequency the frequency of the mixed output is only $\sim 0 - 100$kHz, allowing for tight bandwidth control using low pass filters.

3.1.5 NMR Observables

3.1.5.1 Knight Shift

The most straightforward NMR observable is the measurement of the experimental resonance frequency of a given nucleus under an applied external field. In metals, the observed resonance frequency ω is shifted significantly from the value expected when considering only the applied field, $\gamma_N B_0$. Here γ_N is defined by the resonance frequency of the same nucleus in an insulating

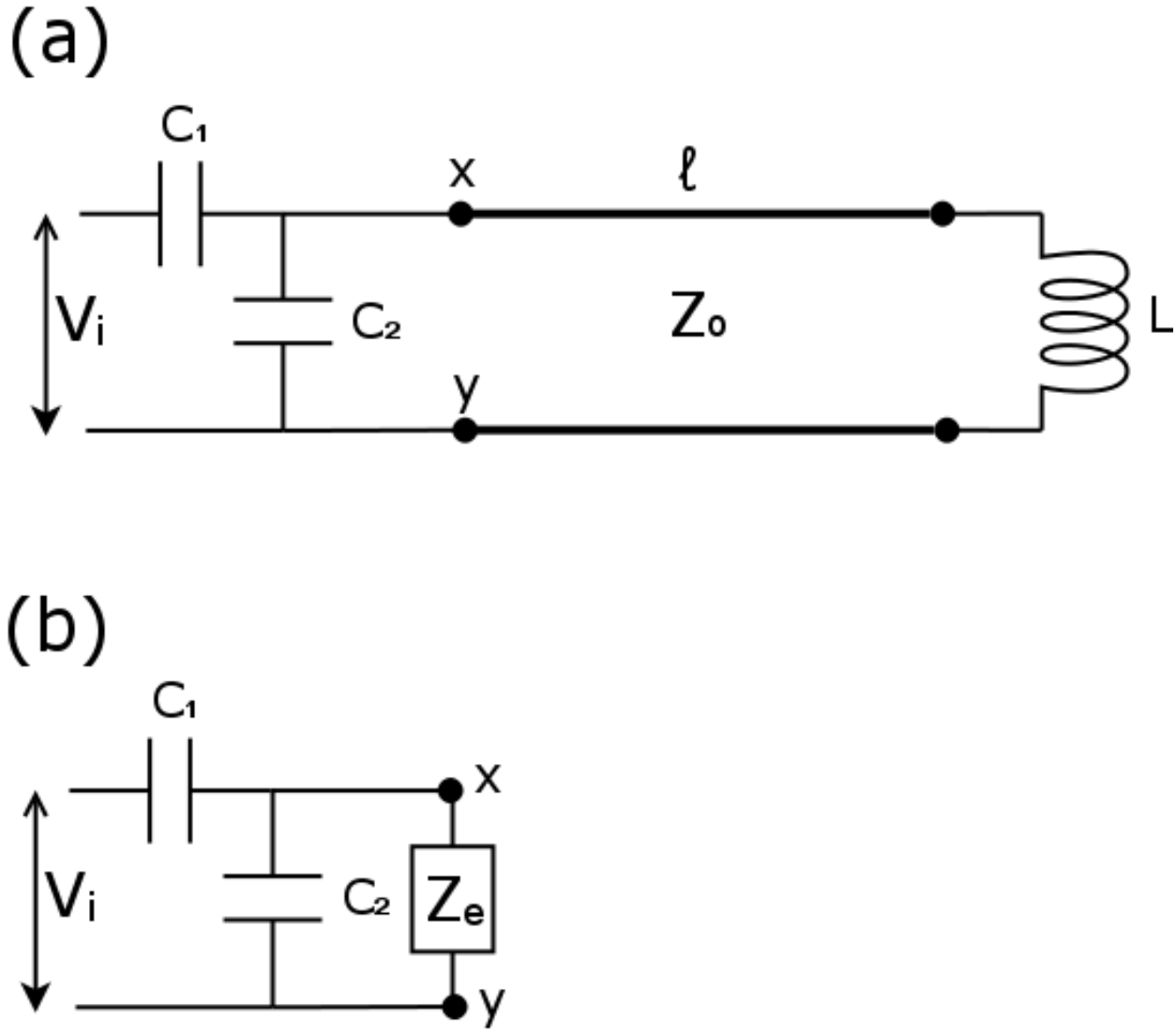

Figure 3.2: **(a)** Transmission line diagram for a top tuning configuration. The NMR sample coil of inductance L is placed at the bottom of the probe below a length ℓ of transmission line. Z_0 is the characteristic impedance of the line. Capacitors at a the top of the probe allow impedance matching with the source. **(b)** The transmission line and inductive load can be replaced by an effective impedance Z_e given in the text.

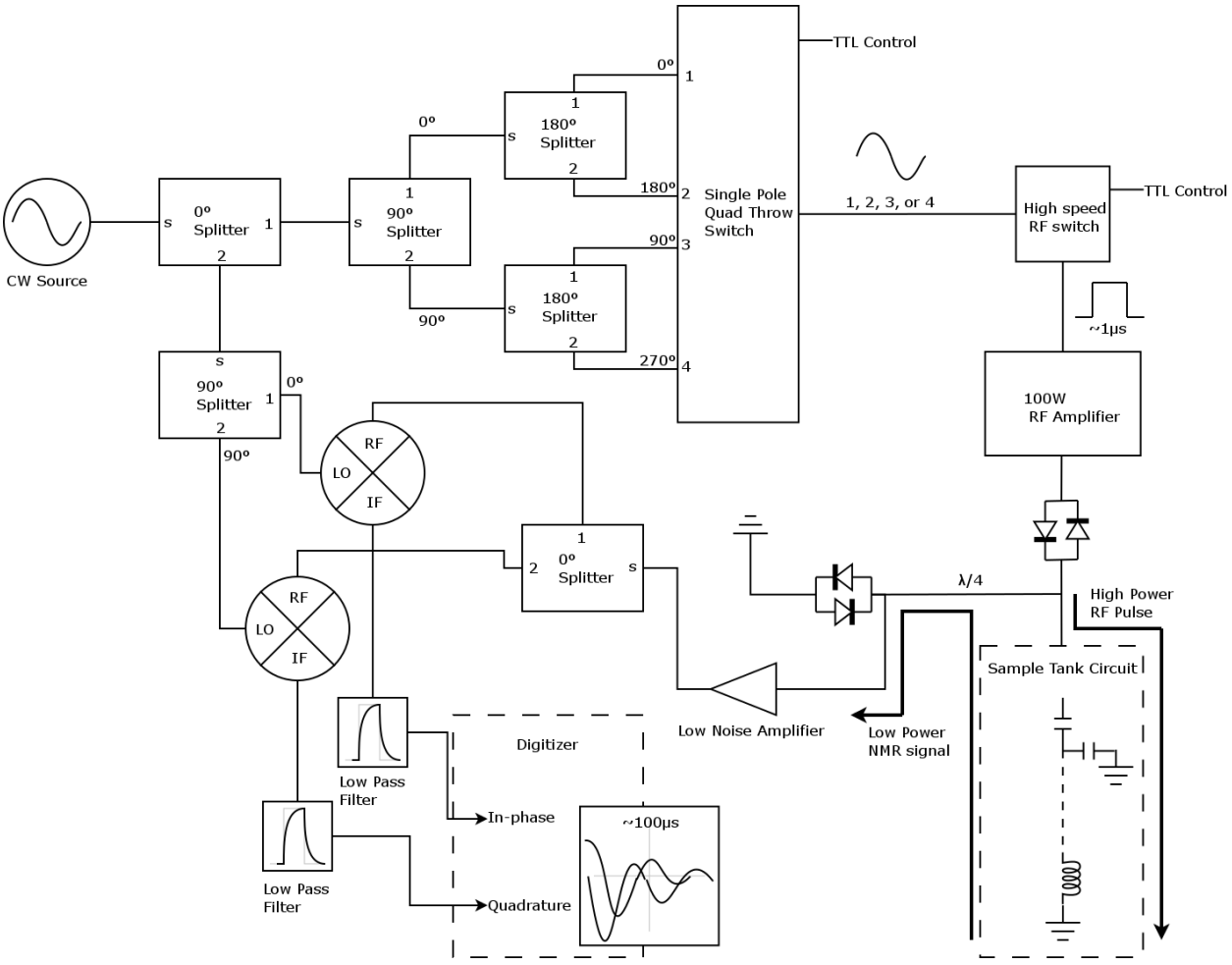

Figure 3.3: NMR spectrometer diagram including both transmit and receive circuits. NMR signal is detected in quadrature for Fourier analysis after high power RF pulse irradiation.

reference material. The percentage shift is called the Knight shift K, given by:

$$K = \frac{\omega - \gamma_N B_0}{\gamma_N B_0} \tag{3.12}$$

In simple metals K is typically of order $1 - 2\%$, increases with atomic number, and is independent of both field and temperature.

Physically, the origin of the shift is in the polarization of free conduction electron spins due to the applied field. This electron spin then produces an additional hyperfine field which is seen by the nucleus. The hyperfine shift is largest for electrons with high s-orbital character as the wavefunction remains nonzero at the nucleus. This wavefunction overlap, also known as the Fermi contact interaction, produces the dominant contribution to the hyperfine field and is parallel with the applied field. For a single band metal, considering only Fermi contact coupling, in cgs units it can be shown that [71]:

$$K^s = \frac{8\pi}{3}\langle|u_k(0)|^2\rangle_{E_F}\chi^s = \langle A_c\rangle\chi^s \tag{3.13}$$

where $\langle|u_k(0)|^2\rangle_{E_F}$ is the electron probability density at the nucleus averaged around the Fermi surface and χ^s is the electron spin susceptibility. The superscript indicates that only the interaction with the electron spin (not orbital effects) are considered. The Fermi contact interaction constant $\langle A_c\rangle$ is positive and isotropic, in good agreement with observations of shifts in elemental s-block metals. Thus, in the simplest case, $K \propto \chi^s$, allowing the spin susceptibility to be experimentally accessed via NMR.

However, for the study of ^{17}O nuclei in Sr_2RuO_4 specifically, the important atomic orbitals at the Fermi surface are the oxygen 2p-orbitals. In this case the electron does *not* make contact with the nucleus ($u_k(0) = 0$) and the hyperfine field is instead dominated by dipolar coupling. In contrast to the Fermi contact field, the hyperfine dipole field is not isotropic in $\mathbf{B_0}$ but varies according to:

$$\mathbf{B_{dip}} = \frac{\mu_0}{4\pi}\left(\frac{3\mathbf{r}(\boldsymbol{\mu_e}\cdot\mathbf{r})}{r^5} - \frac{\boldsymbol{\mu_e}}{r^3}\right) \tag{3.14}$$

where $\boldsymbol{\mu_e} \parallel \mathbf{B_0}$ is the induced magnetic moment of the electron and $\mathbf{r}$ is its position relative to the nucleus. Additionally, for a multi-band metal like Sr_2RuO_4 the coupling can be different for each band that crosses the Fermi surface. In this case, the shift and hyperfine coupling become second rank tensors and Equation 3.13 must be modified to the general form:

$$K^s_{\mu\nu} = \sum_i \langle A_{\mu\nu} \rangle_i \, \chi^s_i \tag{3.15}$$

where the index i runs over all the bands. However, a coordinate system can always be found in which the shift tensor is diagonal, leaving only three independent entries. Labeling these axes x, y, and z gives:

$$\mathbf{K^s} = \begin{pmatrix} K^s_{xx} & 0 & 0 \\ 0 & K^s_{yy} & 0 \\ 0 & 0 & K^s_{zz} \end{pmatrix} \tag{3.16}$$

Measuring the shift for applied fields along the principle axes then determines the entire shift tensor. Thus, combining experimental determination of the Knight shift tensor with knowledge of the band structure allows for extraction of the various spin susceptibilities via Equation 3.15. This makes Knight shift data crucial for investigating unconventional superconductors, where predictions for the behavior of the χ^s depend drastically on the order parameter symmetry (see Chapter 1.2).

3.1.5.2 Spin-Lattice Relaxation

The discussion of the Knight shift in the previous section was implicitly dealing with only the time-averaged hyperfine field experienced by the nucleus during the measured NMR transient. For discussing relaxation behavior, however, it becomes necessary to consider explicitly the microscopic fluctuations which can induce transitions in the spin state of the nuclei. The dominant interaction in metals is typically with the conduction electron spins, just as in the preceding section. In the simplest treatment, this interaction can be thought of as a scattering of a Bloch electron from $|k\sigma\rangle \rightarrow |k'\sigma'\rangle$ along with a nuclear spin transition from

$|I_z = m\rangle$ to $|I_z = n\rangle$. Assuming only a Fermi contact coupling and applying Fermi's golden rule, the relaxation rate for a single nucleus can be calculated as [71]:

$$\frac{1}{T_1 T} = \frac{16}{9}\pi^3 \hbar^3 \gamma_N^2 \gamma_e^2 k_b \langle |u_k(0)|^2 \rangle_{E_F}^2 g(E_F)^2 \tag{3.17}$$

This inverse dependence of T_1 on the temperature is robust in simple metals and is a general result even for more complex interactions. The product of $T_1 T$ and the square of the Knight shift from Equation 3.13 gives a quantity that is independent of the field as well as the details of the band structure, famously referred to as the Korringa ratio:

$$R_K = \frac{K^2}{1/T_1 T} = \frac{\hbar}{4\pi k_b}\frac{\gamma_e^2}{\gamma_N^2} \tag{3.18}$$

where the relation $\chi = \mu_B^2 g(E_F) = (\frac{\hbar\gamma_e}{2})^2 g(E_F)$ for the non-interacting electron gas has been used. This allows comparison of the Knight shift and T_1 to assess the extent to which a metallic system deviates from single particle (non-interacting) behavior.

A more general expression for T_1 relaxation by Moriya relates it to the dynamical electron spin susceptibility at wavevector $\mathbf{q}$ and NMR resonance frequency ω_0 [58]:

$$\frac{1}{T_1 T} \sim \sum_{\mathbf{q}} |A_{\mathbf{q}}|^2 \frac{\chi''_\perp(\mathbf{q}, \omega_0)}{\omega_0} \tag{3.19}$$

where $\chi''_\perp$ is the imaginary part of the transverse dynamical electron spin susceptibility and $A_{\mathbf{q}}$ is the $\mathbf{q}$ dependent hyperfine coupling. In systems close to a ferromagnetic instability $\chi(\mathbf{q}, \omega_0)$ will be enhanced at $\mathbf{q} = 0$, while for antiferromagnetic instabilities it is enhanced at nonzero $\mathbf{q}$ (as is the case in Sr_2RuO_4). Thus, relaxation measurements can also probe the nature of the dominant magnetic fluctuations by investigating T_1 behavior of nuclei at different locations in the crystal lattice.

3.2 In-situ Strain Tuning

Probing samples under strain with NMR techniques is a main focus of this thesis. To accomplish this, single crystals of Sr_2RuO_4 were mounted on commercial CS120/CS130

piezoelectric strain devices from Razorbill Instruments [27]. The device consists of a titanium chassis holding three parallel Lead zirconium titanate (PZT) piezoelectric stacks, shown in Figure 3.4 **(a)**. The stacks are attached to two independent titanium blocks that move relative to each other upon the extension or compression of a stack. The Sr_2RuO_4 single crystal (typical dimension 3mm x 0.3mm x 0.15mm) bridges the two movable titanium blocks and is fixed using Loctite Stycast 2850FT epoxy with Loctite Catalyst #9. In order to create a more homogeneous distribution of strains [4], each end of the sample is mounted symmetrically between a bottom and top plate, illustrated in Figure 3.4 **(b)**. to ensure the sample is held in the middle of the epoxy layer a small piece of 50μm diameter wire is placed on each bottom plate. A spacing washer of thickness 250μm then fixes the distance between the bottom and top plate. The sample ends are carefully placed over the copper wire on each bottom plate and covered with epoxy. Finally the top plates are added and screwed into the cell chassis. A small hole in the top plate allows additional epoxy to be added, making sure the space between the mounting plates is totally filled. Typically, the plates are positioned such that around 1mm of sample is exposed between the two clamps. Once mounted, uniaxial stress is applied to the sample by compressing the outer two piezoelectric stacks while extending the inner stack. The commercial cells are rated for displacements of $13 - 17\mu$m, corresponding to well over 1% strain for a 1mm sample bridge. In practice these limits can be exceeded and the achievable strain is ultimately limited by the sample integrity, which can collapse well before this depending on the quality of mounting. The displacement of the stacks (and therefore the strain) is estimated via a calibrated parallel plate capacitor below the sample.

3.3 Dilution Refrigeration

The low superconducting critical temperature of Sr_2RuO_4 (1.5K) makes typical liquid Helium-4 based cooling designs inadequate. Instead, a Helium-3/Helium-4 dilution refrigerator is

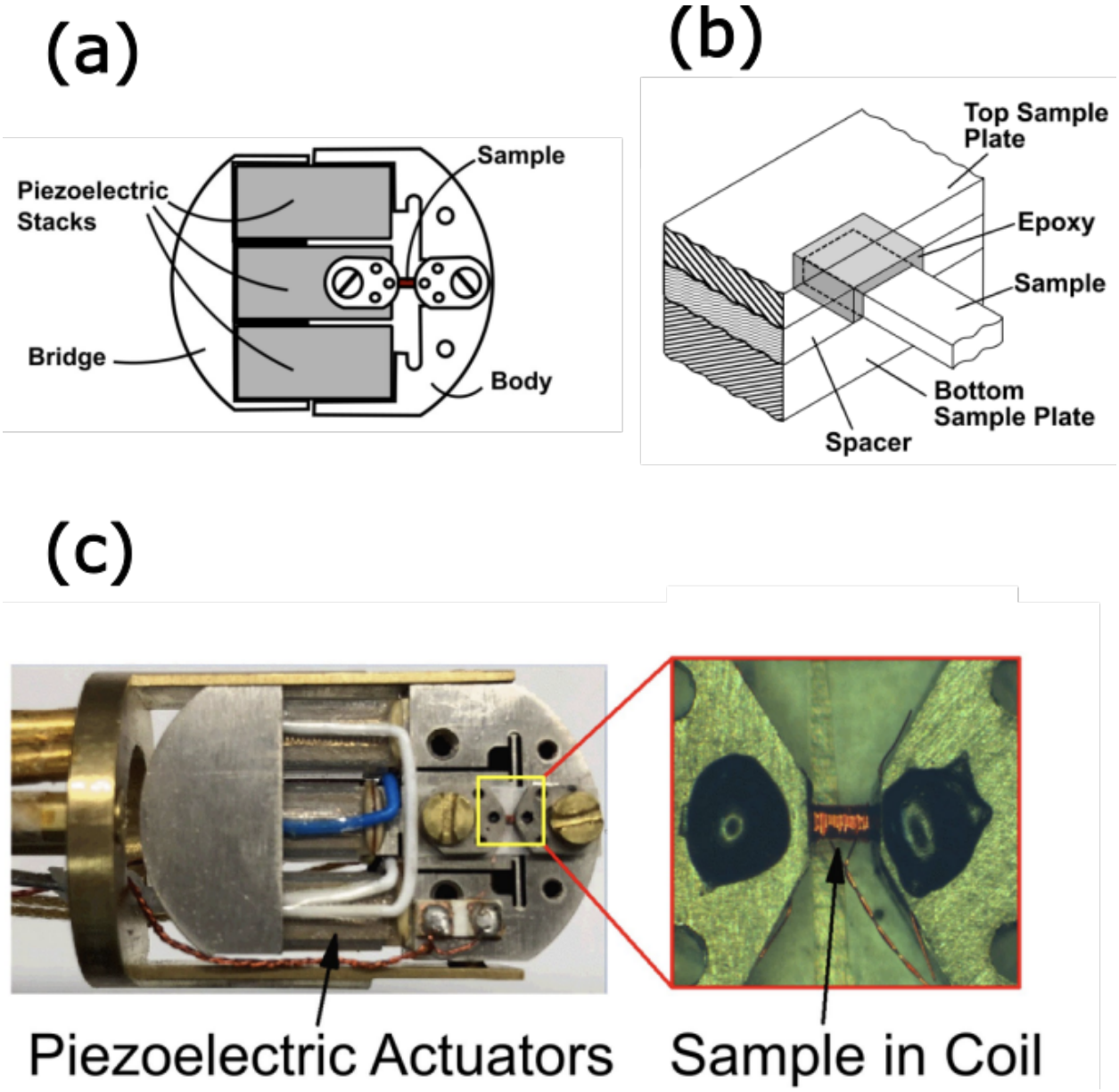

Figure 3.4: **(a)** Schematic of a uniaxial strain device from [27]. **(b)** Sketch of the sample mount. Both ends of the sample are placed between a top and bottom plate held apart by a spacer and set with epoxy. **(c)** Left: Razorbill CS130 strain cell with loaded sample. Right: Enlarged view of sample mounting. Stycast epoxy (black) fixes the sample to the mounting plates. NMR coil is wound along the entire exposed length of sample.

used, a schematic of which is shown in Figure 3.5. Initially, a mixture of Helium-3 and Helium-4 gas is condensed into the mixing chamber where it naturally phase segregates into a lighter phase of concentrated Helium-3 and a heavier diluted phase of Helium-4 mixed with $\sim 6-7\%$ Helium-3. The Helium-4 is effectively inert and does not interact with the Helium-3 in the dilute phase. As a result, the system can be considered a phase boundary of pure liquid Helium-3 in the concentrated phase and Helium-3 "gas" dissolved in the dilute phase. Since the enthalpy of the concentrated phase is larger than that of the dilute phase, heat can be removed from the system by driving Helium-3 across the phase boundary via an osmotic pressure gradient. The gradient is created by pumping on the dilute phase in the still, which selectively removes Helium-3 due to its much larger vapor pressure [28]. For continuous operation, the Helium-3 is then cleaned and re-condensed at $\sim$ 1.3K via heat exchange with a low pressure Helium-4 chamber called the 1K-pot. The condensed Helium-3 is further cooled by a series of heat exchangers with the dilute phase before re-entering the mixing chamber. Unlike typical evaporative cooling approaches, this mechanism is operable down to absolute zero because the concentration of Helium-3 in the dilute phase (analogous to the vapor pressure for a liquid-gas boundary) remains finite. However, in practice the efficiency of heat exchange between the dilute and concentrated phases, along with heat leaks to the ambient environment, will determine the equilibrium temperature of the mixture. Taking this into account, the mixing chamber temperature T_{mc} can be shown to satisfy [9]:

$$T_{mc} = \sqrt{\frac{\dot{Q}_{HL}}{\dot{n}a} + \frac{bT_R^2}{a}} \tag{3.20}$$

where $\dot{Q}_{HL}$ is the heat flow from the environment, $\dot{n}$ is the molar circulation rate of Helium-3, and T_R is the temperature of the recirculated Helium-3 entering the mixing chamber. The constants a and b are the empirical low-temperature quadratic coefficients of the dilute phase enthalpy $H_d(T)$ and concentrated phase enthalpy $H_c(T)$ respectively [62]:

$$H_d(T) = aT^2 = (94\text{J/mol K}^2)T^2 \tag{3.21}$$

$$H_c(T) = bT^2 = (12\text{J/mol K}^2)T^2 \tag{3.22}$$

Taking feasible values of $\dot{Q}_{HL} = 20\text{nW}$, $\dot{n} = 10^{-5}\text{mol/s}$, and $T_R = 3T_{mc}$ gives a base temperature of $T_{mc} \sim 30\text{mK}$. Thus, dilution refrigeration allows access to much lower temperatures than cryostats that rely on the evaporation of Helium-4. Particular to this work, base temperatures of $T_{mc} \sim 20\text{mK}$ were achieved, enabling the study of Sr_2RuO_4 well below its superconducting critical temperature of $T_c = 1.5\text{K}$.

3.4 Radiofrequency AC Susceptibility

A measurement of the superconducting transition of the sample can be made utilizing the same circuitry already discussed for NMR signal detection. However, rather than high power RF pulses, an extremely low power CW excitation is transmitted to the sample coil. The reflected CW from the tank circuit is then circulated to the quadrature detection receiver. A diagram of the measurement circuit is shown in Figure 3.6 (A). The phase and amplitude of the reflected CW is a function of the reflection coefficient Γ of the tank circuit (discussed in Chapter 3.1.3), which depends on the inductance of the NMR coil. This inductance changes sharply when the enclosed sample goes superconducting and can be used to mark the transition. Thus, measuring the tank circuit reflected power using this setup as a function of either temperature or applied field allows for in-situ measurements of both T_c and B_{c2} on the NMR sample. In Chapter 4.1 the question of instantaneous sample heating from the NMR pulses themselves will be important. Figure 3.6 (B) shows a similar circuit used to measure the *time dependence* of Γ after an incident high power NMR pulse. A separate pulse transmit circuit, such as the one in Figure 3.3 is used to generate a microsecond high amplitude pulse. Immediately after transmitting this to the tank circuit a switch is used to perform the low amplitude reflected power measurement just discussed. However, the reflected power is now recorded as a function of time on a digitizer rather than just the average amplitude. This allows the state of the sample (superconducting or normal) to be monitored as a function of time after the NMR pulse.

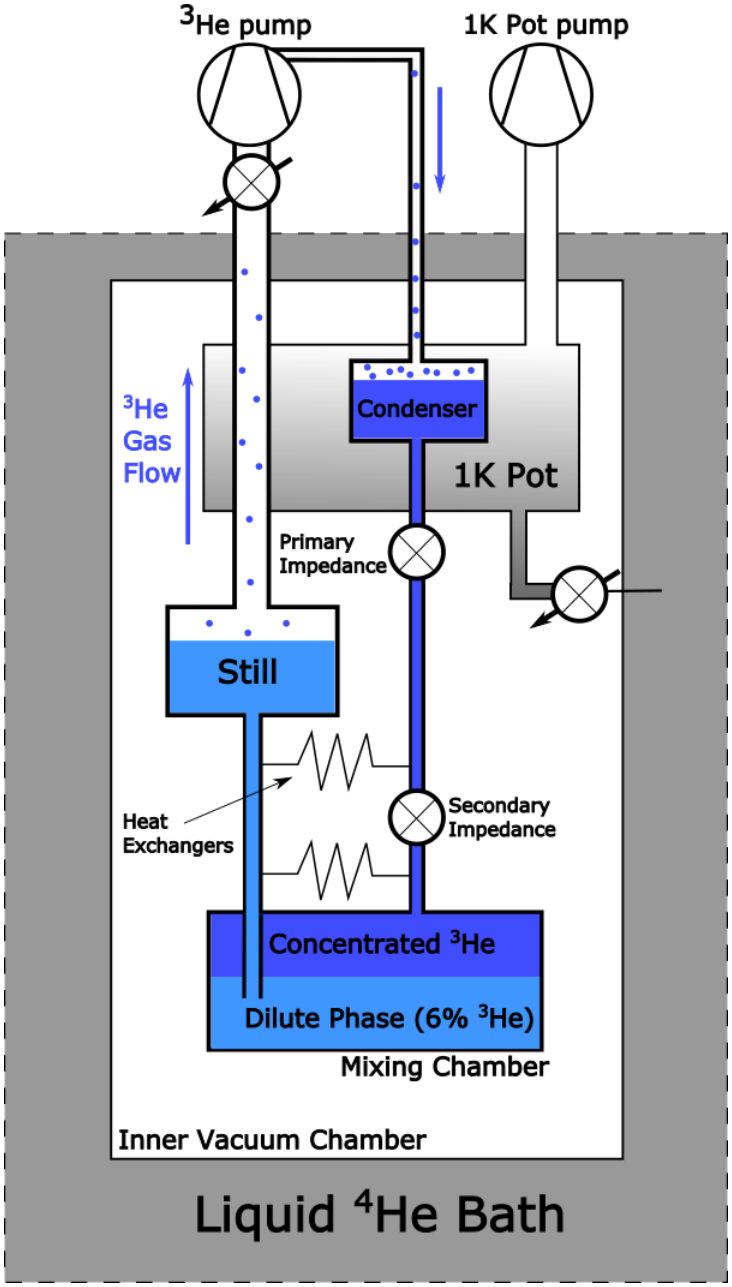

Figure 3.5: Basic schematic of a dilution refrigerator. Cooling power is provided by ^{3}He crossing the boundary between the concentrated phase and the dilute phase. The ratio of ^{3}He and ^{4}He in the mixture is chosen such that the phase boundary lies in the mixing chamber where the sample is mounted.

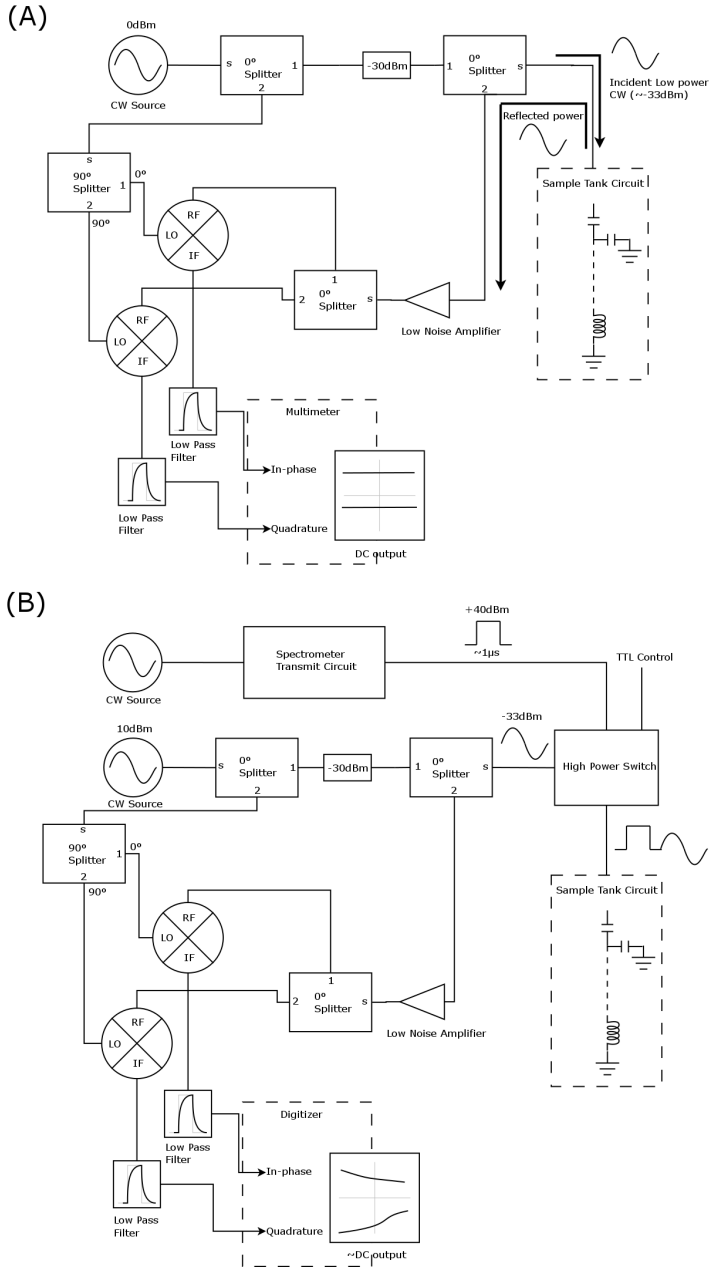

Figure 3.6: **(A)** Circuit diagram for equilibrium low power reflection measurements. The reflected power will have the same frequency as the CW source resulting in DC output after down-conversion and filtering. **(B)** Detection circuit for the time dependence of the reflection coefficient directly after an incident high power NMR pulse

CHAPTER 4

Experimental Results on the Superconducting State

4.1 Pronounced drop in ^{17}O Knight Shift

As discussed in detail in Chapter 2, the nature of superconductivity in Sr_2RuO_4 has been a subject of research for more than two decades now. In 2017, interest was reignited when measurements performed using a uniaxial strain device observed an impressive increase in the superconducting critical temperature as a function of in-plane anisotropic strain [74]. T_c more than doubled at a critical value of a-axis strain (ε_v), which was attributed to a singularity in the density of states as the Fermi surface undergoes a Lifshitz transition. The possibility of a change in the order parameter symmetry as a result of this anisotropic strain was of particular interest. Presented here are ^{17}O NMR Knight shift measurements covering the interval $\varepsilon_{aa} = [0, \varepsilon_v]$ used to probe the evolution of the superconducting state spin polarization leading up to the Lifshitz transition. A reduction of the Knight shift was found for all measured strains *including the unstrained case*, directly contradicting previous NMR reports [33]. The results are incompatible with a chiral p-wave state and rule out the most widely accepted superconducting order parameter.

4.1.1 Methods

4.1.1.1 Sample preparation

High quality Sr_2RuO_4 single crystals were grown by our collaborators at MPI CPfs Desden using the standard floating zone method [54]. The samples were cut and polished into

rectangular bars of typical dimension 3 x 0.3 x 0.15 mm^3 with long axis along the [100] direction. ^{17}O substitution was achieved via high temperature annealing at 1050°C in a 50% $^{17}O_2$-enriched atmosphere for two weeks. The sample preparation was performed by Eric Bauer at Los Alamos National Laboratory.

4.1.1.2 NMR under strain setup

The sample was mounted in a commercial Razorbill CS130 strain cell such that stress was applied along the [100] crystal direction. A coil of ~ 20 turns was wrapped around the sample inside the strain cell for the NMR measurements. The NMR tank circuit was constructed using the top tuning configuration outlined in Chapter 3.1, allowing the high amplitude RF to reach the sample coil. ^{17}O NMR measurements were then performed while the sample was strained in-situ by controlling the voltage across the strain cell's piezoelectric stacks. See Chapter 3.2 for details on the sample mounting and piezo control.

4.1.1.3 Cryostat

The experiments were carried out in an Oxford Instruments Kelvinox dilution refrigerator placed inside a 0-12T variable field superconducting magnet. A schematic and explanation of the dilution refrigerator is given in Chapter 3.3. The strain cell holding the sample was placed in the mixing chamber with $B||[010]$ and immersed in the dilute phase of the $^3He/^4He$ mixture. Cooling power from the evaporation of Helium-3 in the mixing chamber then allows the sample to reach a base temperature of 20mK. The temperature of the mixing chamber was verified by $^{63}T_1$ relaxation measurements on the copper NMR coil.

4.1.1.4 Reflected power measurements

In order to track the superconducting transition, as well as monitor the transient effect of pulse heating, the reflected power from a continuous RF source was measured. The amplitude

and phase of the reflection is sensitive to the coil inductance and loss, which changes abruptly when the sample goes superconducting. A schematic circuit diagram for this measurement is shown in Chapter 3.4.

4.1.1.5 Quadrupolar Shift Analysis

For nuclei with $I > 1/2$ such as ^{17}O there is an interaction between the electric crystal field and the non-spherical charge density of the nucleus. The total Hamiltonian can be written

$$H = H_Z + H_Q \tag{4.1}$$

$$= (1+K)^{17}\gamma \mathbf{B}\cdot\mathbf{I} + \frac{eQV_{zz}}{4I(2I+1)}[3I_z^2 - I^2 + \eta(I_x^2 - I_y^2)] \tag{4.2}$$

where the first term is the Zeeman interaction, including the Knight shift, and the second is the quadrupolar interaction. eQ is the quadrupole moment of the nucleus, $[I_x, I_y, I_z]$ are the nuclear spin operators, $[V_{xx}, V_{yy}, V_{zz}]$ are the principle axes of the electric field gradient, and $\eta = (V_{xx} - V_{yy})/V_{zz}$. The parameters of H_Q have been measured experimentally [46] and are used to calculate the quadropolar contribution to the resonance frequency numerically. In all the NMR shift data presented here the quadrupolar part has been subtracted out in order to isolate the hyperfine shifts. For details on the calculation and subtraction see Appendix 6.1.

4.1.2 Results

After subtraction of any quadrupolar contribution, the NMR Shift (K) is proportional to the microscopic magnetic field seen by the NMR active nucleus. In metals, polarization of the electron spins by the applied external field produces the dominant effect. The resulting hyperfine shift is labeled K_s and is proportional to the spin polarization M_s of the electrons: $K_s = AM_s/B_0$. This is typically written as a susceptibility ($K_s = A\chi_s$), but the general form allows for the possibility of a nonlinear response, which can arise both from field-induced quasiparticles as well as the effect of the proximate quasi-2D singularity in the DOS [46]. Magnetic fields from orbital motion of electrons can also produce a shift K_o, resulting in the

total NMR shift $K = K_s + K_o$. However, assuming the orbital shifts are small, K tracks the spin polarization of the sample, allowing a comparison of the superconducting state to that of the normal state.

First, the sample was tuned to the critical value of a-axis strain such that T_c and B_{c2} were maximized, shown in Figure 4.1. Figure 4.2 (a) then shows the central transition spectra at this critical strain for the three unique oxygen sites. The apical oxygen is labeled O(2), while the in-plane sites are labeled O(1) and O(1′) (see Appendix Figure 6.7). The measurements were taken with $B_0 = 1.9980$T ($B_0/B_{c2} \approx 0.45$) and the field was calibrated to within tens of μT via the NMR resonance frequency of ^{3}He inside the sample chamber. The critical temperature at this strain and field is approximately 2.6K, verified by a.c. susceptibility measurements shown in the lower inset of Figure 4.2 (b). As temperature is lowered below $T_c = 2.6$K there is a distinct change in the central transition frequency of all three oxygen sites. Each resonance peak moves away from the normal state frequency (black lines) towards the frequency corresponding to zero shift (dashed lines). Note that the zero shift positions are different for each site due to the quadrupolar contribution. This equates to a reduction in the magnitude of the NMR shift, which is plotted in the main panel of Figure 4.2 (b).

As the temperature approaches zero, the magnitude of K at the critical strain is seen to reduce by approximately 20-30% compared to its normal state value, which is qualitatively different from the behavior reported at zero strain [33] and incompatible with the chiral p-wave state. A possible explanation is a phase transition to a different order parameter symmetry as the critical strain is approached. To address this we also carried out measurements of the shifts over the entire strain interval from $[0, \varepsilon_v]$. The strain dependence of K for both in-plane oxygen sites is shown in Appendix 6.2, where a continuous evolution with strain is observed for all temperatures and fields. We therefore find no evidence for a change in order parameter symmetry between the high strain and zero strain conditions. Furthermore, consistent with the absence of an observed phase transition, a reduction in shift in the superconducting state is resolved even at zero strain where the results are found to depend sensitively on the

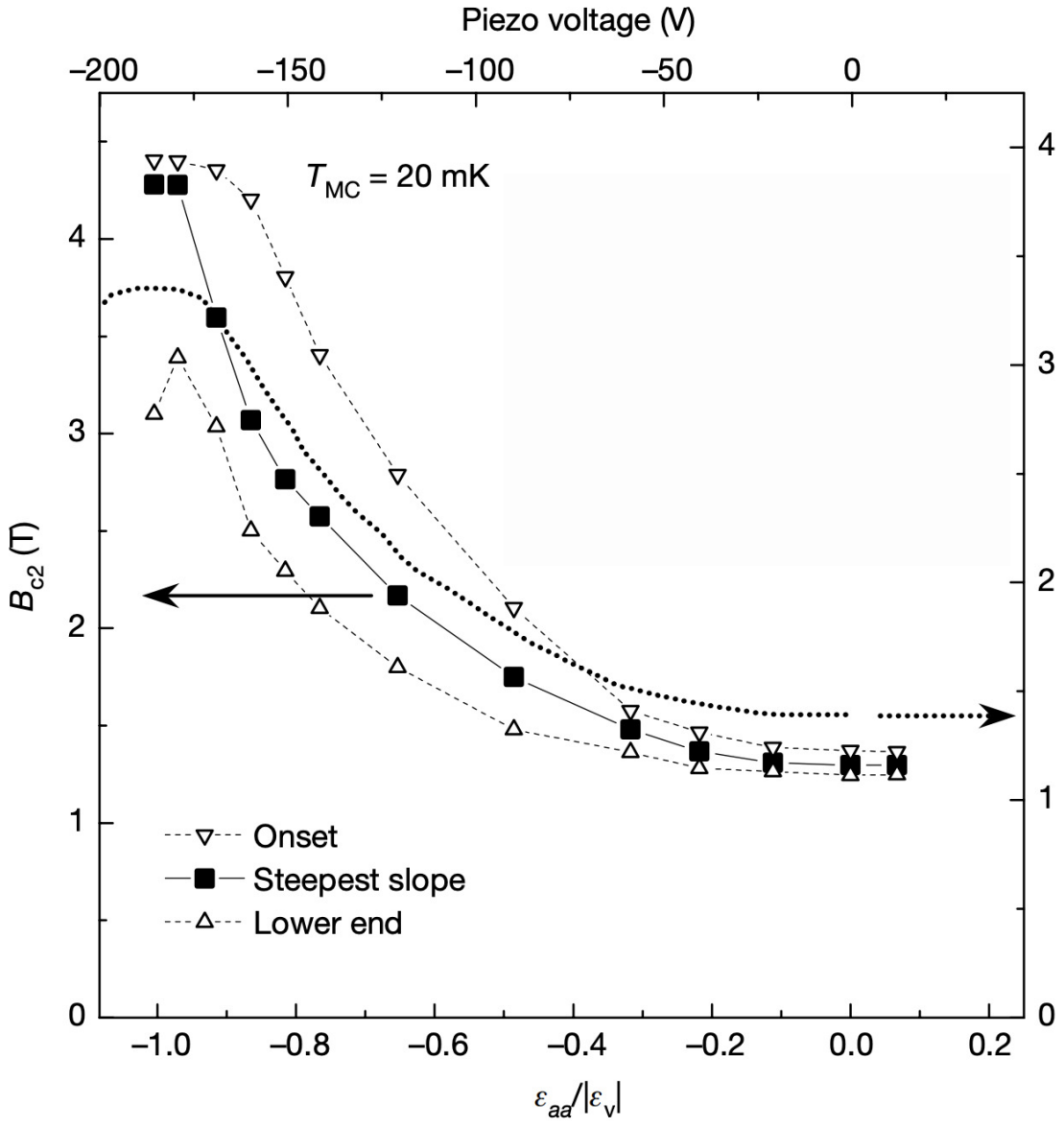

Figure 4.1: Upper critical field B_{c2} at $T = 20$mK as a function of a-axis strain measured with a.c. susceptibility. Solid squares denote the steepest slope, while open triangles mark the onset and end of the transition. The increase of B_{c2} with strain follows the trend of the critical temperature, reproduced from [74] as the solid black circles.

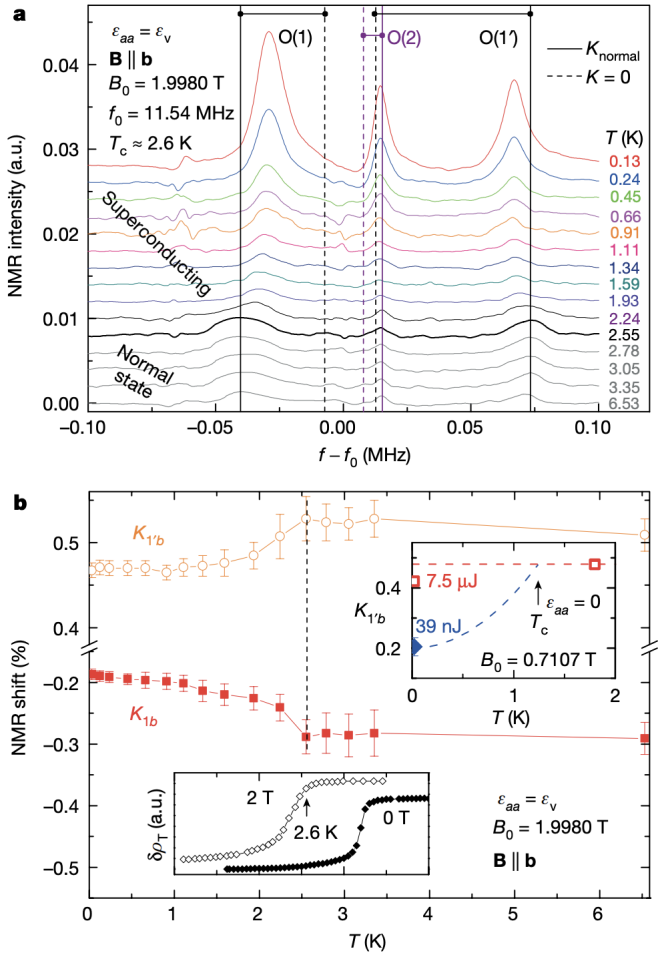

Figure 4.2: **(a)** Central transition spectra for the three oxygen sites O(1), O(2), and O(1') measured at $B_0 = 1.9980$T and carrier frequency $f_0 = 11.54$MHz. Solid black lines indicate the normal state line position and dashed lines indicate the zero shift line position. **(b)** A pronounced drop in the shift magnitude for both in-plane sites is observed upon lowering temperature through $T_c = 2.6$K. **(Lower inset)** Reflected power measurement used to identify T_c at the applied B_0. **(Upper Inset)** Shift measurements at $\varepsilon_{aa} = 0$ similarly show a decrease in K, but depend crucially on the pulse energy.

incident NMR pulse energy, shown in the upper inset of Figure 4.2 (b).

The zero strain spectra for FID sequences of varying pulse energy are presented in Figure 4.3 (a). The red and brown spectra are taken using a two pulse spin echo sequence and differ only slightly despite the brown curve corresponding to the normal state ($T = 1.8$K) and the red to the superconducting state ($T = 20$mK). Nevertheless, there is already a resolvable change in the central transition frequency of the O($1'$) site. When the incident pulse energy is lowered by using single pulse FID sequences of decreasing length and amplitude, the reduction in shift across all three sites becomes significant. The shifts are plotted as a function of pulse energy in Figure 4.3 (b). K increases rapidly with pulse energy above a crossover scale of $\sim 1\mu$J, before leveling out near the normal state values. This behavior is suggestive of instantaneous sample heating by the NMR pulse sequence. Such a process is possible via the dissipation of energy from the high amplitude RF field by eddy current formation in the sample. If this incident RF energy is too high, the sample could be driven out of the superconducting state for timescales comparable to the NMR transient ($\sim 50 - 100$ microseconds). The measured spectra would then correspond to the normal state regardless of the nominal temperature of the cryostat.

To test this interpretation, reflected power measurements were made on the RF tank circuit containing the sample coil. First, a high power RF pulse is applied to the sample as in the NMR experiments, then a low power CW source is transmitted to the tank circuit to make a phase sensitive measurement of the reflected power as a function of time, described in detail in Chapter 3.4. The results are shown in Figure 4.4 for different incident RF pulse energies. At the highest pulse energies, there is initially a rapid change in both in-phase and quadrature parts of the reflected power for about 100 microseconds. Smaller changes then persist for a few milliseconds before the transient response disappears completely. For incident pulse energies less than $\sim 1\mu$J the time and energy dependence is much weaker and the curves overlap, consistent with the behavior of the NMR shifts. From this we conclude that the sample is indeed driven into the normal state after a sufficiently high power RF

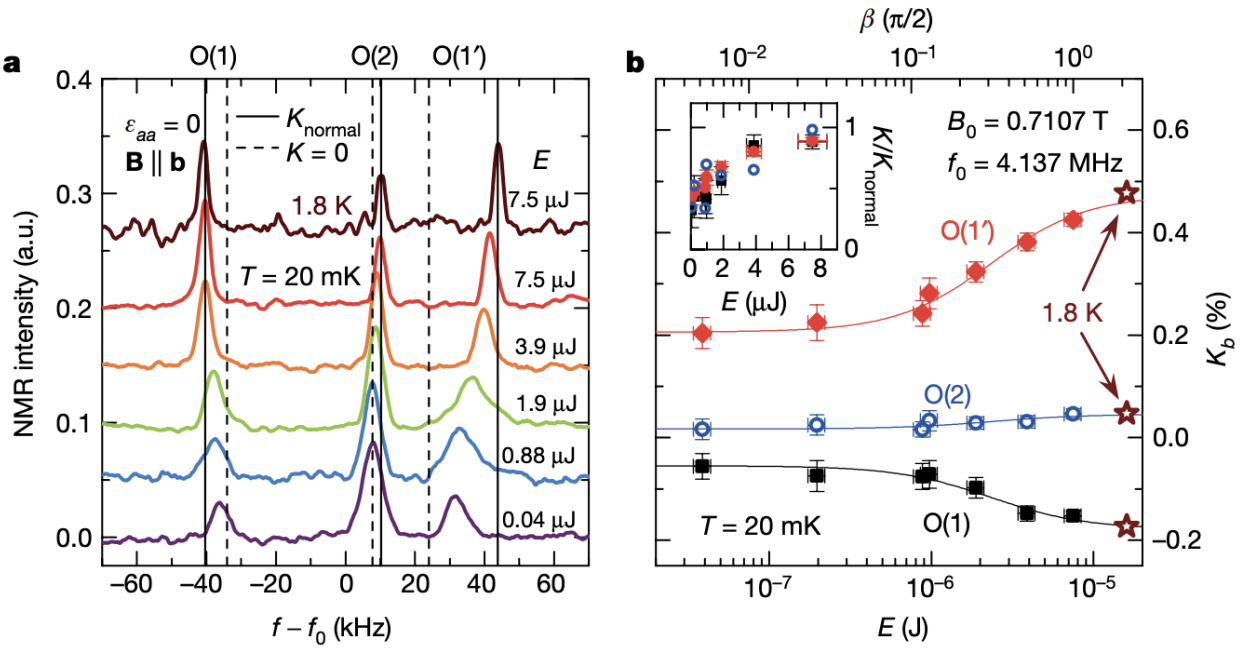

Figure 4.3: **(a)** Zero strain FID spectra as a function of incident pulse energy carried out at 20mK with $B_0 = 0.7107$T and $f_0 = 4.137$MHz. Solid black lines indicate the normal state position and dashed lines indicate the zero shift position. The magnitude of the shift for all three sites decreases with lower pulse energy **(b)** Dependence of the shifts on pulse energy E and tip angle β. **(Inset)** Shift versus pulse energy normalized to each site's normal state value. The decrease is consistent between the sites.

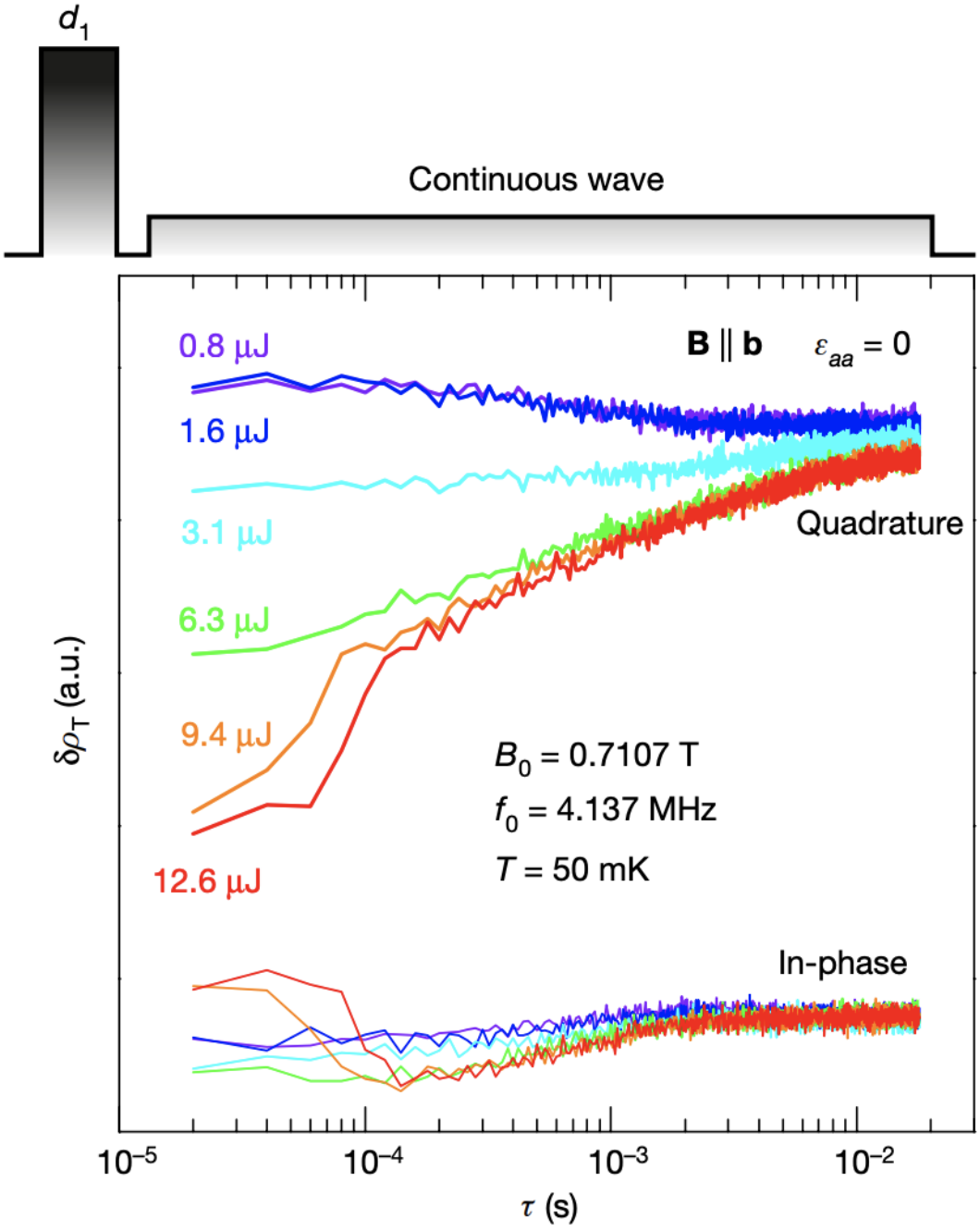

Figure 4.4: Time dependence of in-phase and quadrature components of the reflected CW power after a high amplitude RF pulse. Strong transient behavior is seen in both channels for approximately 100μs after pulses of sufficient energy. A more gradual transient follows, lasting about 1ms.

pulse and stays there for about 100 microseconds. A second period of relaxation occurs in the superconducting state for another millisecond, which we attribute to vortex dynamics. Furthermore since the timescale for relaxation to the normal state is comparable to the NMR transient, this is consistent with the observation of normal state K even for temperatures nominally lower than T_c when using standard NMR pulse lengths.

4.1.3 Discussion

In summary, by way of the ^{17}O NMR shift, a reduction in the spin polarization of Sr_2RuO_4 is detected upon entering the superconducting state for the entire range of strain $\varepsilon_{aa} = [0, \varepsilon_v]$, notably including the unstrained condition. A reduction in the shift of about 50% is observed in unstrained samples with $B_0/B_{c2} = 0.55$, while a reduction of 75% is observed at the critical strain with $B_0/B_{c2} = 0.17$. This contradicts a previous body of NMR work [33] and is inconsistent with chiral p-wave superconductivity in Sr_2RuO_4. Furthermore, no evidence of a first-order phase transition is found as a function of strain, implying the symmetry of the order parameter is not changed as the Fermi surface approaches the Lifshitz transition and T_c is maximized.

In addition to the chiral p-wave state, any odd parity state with $\mathbf{d} \parallel c$ is expected to have no reduction in spin polarization for in-plane applied field, incompatible with our findings. States with $\mathbf{d} \parallel ab$ on the other hand are expected to have a drop in polarization of 50%, neglecting Fermi liquid effects. These states are not ruled out by our measurements, which observed a drop of roughly the same magnitude. However, due to signal strength constraints, the zero strain measurements were done at a significant fraction of B_{c2}, where a sizable magnetic response from field-induced quasiparticles is expected regardles of the order parameter symmetry. This implies that the actual condensate spin polarization is even smaller than the measured reduction in shift would suggest. However, difficulty in estimating this quasiparticle background prohibits eliminating the possibility of odd parity superconductivity on the basis of this data alone, necessitating more sensitive measurements

performed at lower fields.

4.2 Evidence for Even Parity Unconventional Superconductivity

The results of the previous experiment were shown to rule out the most popular odd parity order parameter proposed for Sr_2RuO_4, the chiral p-wave $\mathbf{d} = \hat{\mathbf{z}}(k_x \pm k_y)$ state. However, alternative odd parity proposals with in-plane d-vector remained a possibility and were subsequently discussed theoretically [66, 65]. The results presented now go further, extending the shift measurements down to much lower fields by using larger samples and higher percentage of ^{17}O substitution. Comparison of these measurements to reported specific heat data [60] then allows a quantitative analysis of the quasiparticle background induced by the applied field. By doing this we place an upper bound on the magnetic response of the superconducting condensate of less than 10% that of the normal state, enough to rule out all possible pure p-wave states in Sr_2RuO_4.

4.2.1 Methods

4.2.1.1 Sample preparation

Samples were grown using the same methods detailed in Chapter 4.1.1. The single crystal under test had dimensions 3.5 x 1 x 0.2 mm^3 with the longest dimension along [100]. The annealing process was also repeated but with higher purity 90% $^{17}O_2$ gas.

4.2.1.2 NMR setup

NMR measurements were performed using an Oxford Instruments Kelvinox dilution refrigerator placed inside a 0-12T superconducting magnet. The sample was wrapped inside a coil of wire along its entire length and mounted onto a piezoelectric rotator. The rotation axis was aligned such that the angle between the applied field and the ab crystal plane could be

varied.

4.2.1.3 In-plane field calibration

Using the reflected power circuit described in Chapter 3.4, the the upper critical field was measured as a function of out-of-plane angle and compared to published values [81]. This allowed the applied field to be oriented parallel to the ab plane to within $\pm 0.2^{\circ}$.

4.2.1.4 Analysis of angle-dependent quadrupolar effects

The quadrupolar contribution to the shifts were extracted by numerical diagonalization of the nuclear Hamiltonian. At the lowest fields studied, the dependence of this contribution on in-plane angle becomes the dominant source of uncertainty. A detailed analysis of the angular dependence allowed a determination of the in plane angle to within $\pm 0.4^{\circ}$. For more details see Appendix 6.3.

4.2.2 Results

The previous experiment identified heating by the RF pulses as a major problem in correctly extracting NMR shifts in the superconducting state. As such, understanding the pulse energy requirements for measuring the true superconducting response is key. Figure 4.5 (B-C) shows central transition spectra for the three oxygen sites using different incident pulse energies E_p recorded at $B_0 = 1.38$T and $B_0 = 1.50$T, which are just below and just above the upper critical field $B_{c2} = 1.42$T respectively. With $B_0 > B_{c2}$ the spectra are independent of pulse energy and consistent with the normal state positions. With $B_0 < B_{c2}$, a normal state spectra is still recorded at high pulse energies due to heating of the sample, but a second line appears for each site at low pulse energies corresponding to the superconducting state. This coexistance of superconducting and normal state phases is expected very close to the transition, which is known to be first-order [82]. For fields lower than B_{c2} the shift identified

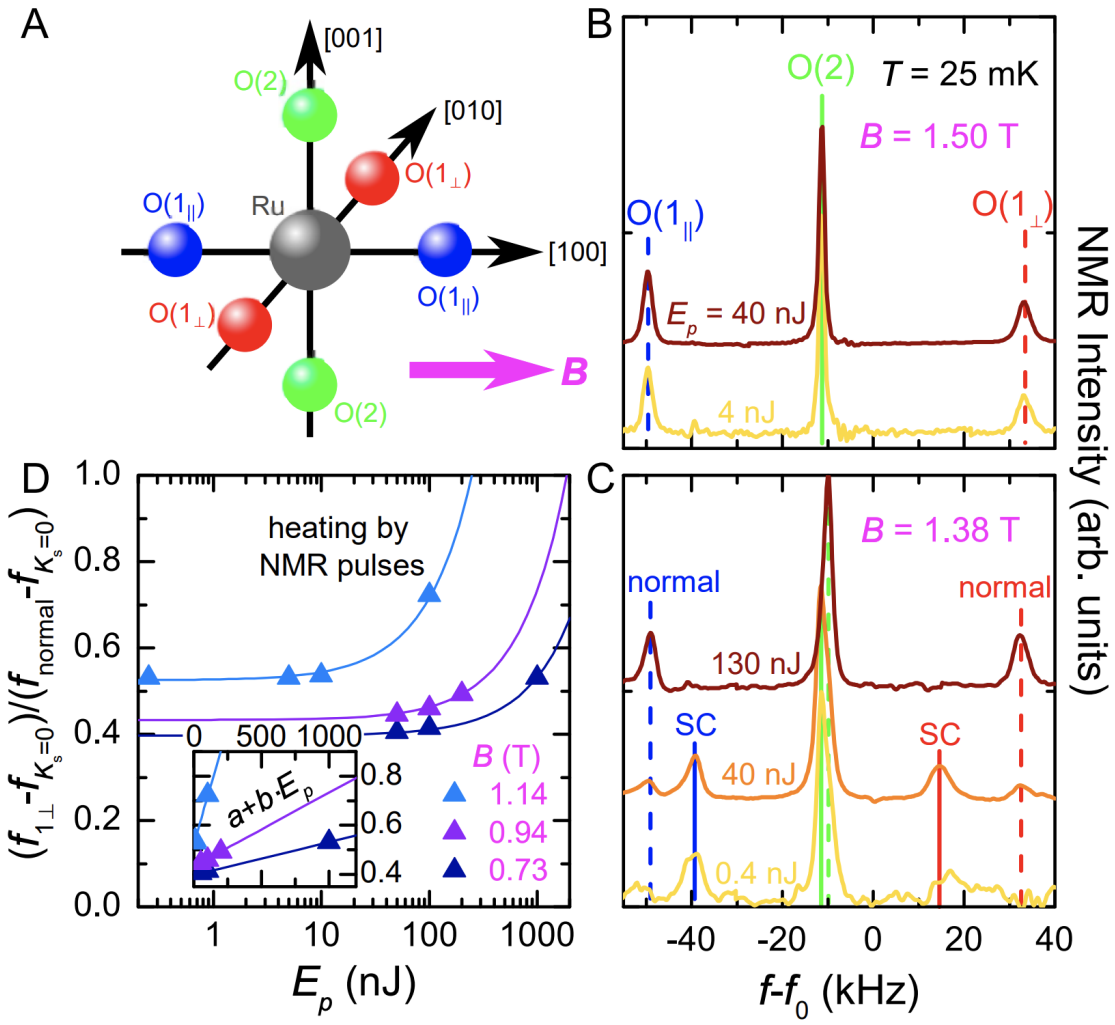

Figure 4.5: **(A)** Orientation of the three oxygen sites relative to the applied field. **(B)** The central transition spectra are independent of pulse energy at $B = 1.50\text{T} > B_{c2}$. **(C)** At $B = 1.38\text{T} < B_{c2}$ a normal state sprectrum is still observed for $E_p \geq 130\text{nJ}$. A second line appears for each site upon reducing to $E_p \geq 130\text{nJ}$, which we attribute to coexistence of the superconducting and normal phases. Even lower power reveals the pure superconducting spectrum. **(D)** Central transition frequency of the $\text{O}(1_\perp)$ relative to the zero shift position as a function of pulse energy for different applied fields. The critical temperature is reduced at higher fields requiring lower pulse energy to avoid perturbing the superconducting state.

with the superconducting state is determined by lowering the incident energy until the the measured shift no longer depends on E_p, as shown in Figure 4.5 (D). Fields closest to the transition require the lowest pulse energies to achieve this condition, which is expected as T_c approaches zero when $B_0 \to B_{c2}$. This procedure is repeated for all shift values and spectra reported here in order to ensure the systematic effect of RF heating is eliminated.

Figure 4.6 shows the ^{17}O central transition spectra recorded at $T = 25$mK as a function of decreasing in-plane field. The overlaid solid markers are the calculated normal state line positions using the known shift and quadrupolar parameters, and the open markers correspond to the calculated $K_s = 0$ peak position. Note the orbital shift for each site is now considered explicitly, using values determined in [33]. For details on the orbital shifts see Appendix 6.4. The difference between these markers is then proportional to K_s and thus the hyperfine field. Above B_{c2} the transition frequencies agree very well with the normal state expectations. Once the field is lowered below B_{c2} and the sample becomes superconducting, the central transitions of all three sites move towards the dashed lines, meaning the K_s is reduced. Figure 4.7 (A) shows the extracted total shift ($K = K_s + K_o$) excluding the quadrupolar part, where the dotted lines show the $K_s = 0$ value for each site. Figure 4.7 (B) plots only the hyperfine part of the shift K_s, normalized to that of the normal state. As discussed in Chapter 3.1.5, it is this contribution to the shift that is proportional to the spin polarization. From Figure 4.7 (B) we see a discontinuous drop in K_s across B_{c2} for all sites as expected from the first order superconducting transition. As the field is lowered further, there is a consistent monotonic reduction in K_s for fields along both the [100] and [110] directions. Additionally, the K_s measured with $\varepsilon_{aa} = \varepsilon_v$ in the previous section is plotted in cyan and is consistent with the unstrained data when normalized to the strain enhanced B_{c2}.

At the lowest field measured ($B = 0.24$T) K_s is reduced to approximately 20% of its normal state value. Lowering the field even further was not feasible, as the hyperfine shift becomes too small and uncertainty in the angle dependent quadrupolar effect begins to dominate. However, a quantitative estimate of the quasiparticle background can be inferred by comparison to

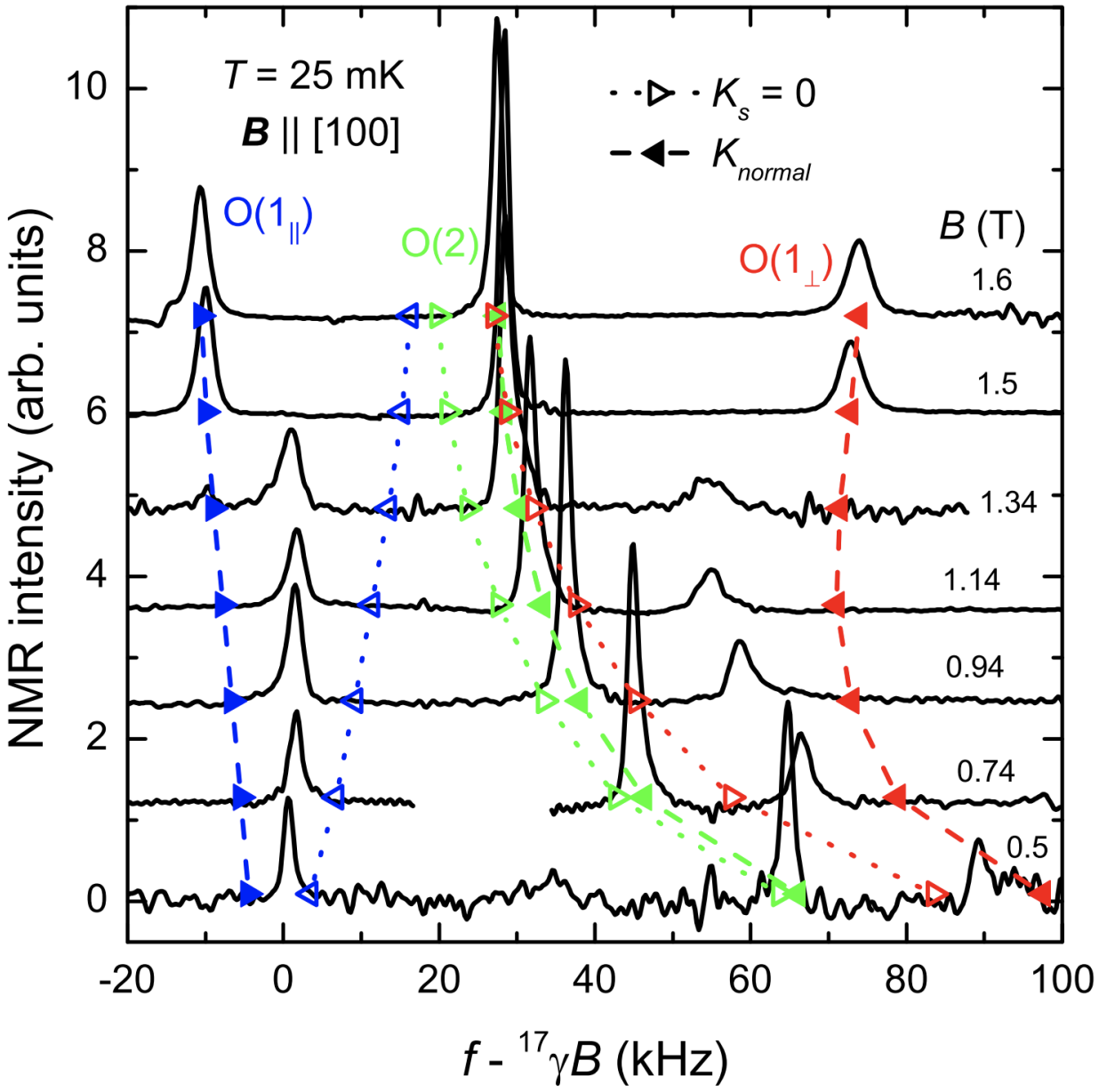

Figure 4.6: ^{17}O central transition intensity versus $f - {}^{17}\gamma B$, measured at 25mK with field applied along [100]. The three spectral lines correspond to the O($1_{||}$), O(2), and O($1_{\perp}$) sites from left to right. Each spectra is recorded at sufficiently low pulse energy to ensure a response associated with the superconducting state. Solid symbols and open symbols for each site indicate the normal shift and zero shift positions respectively.

reported specific heat data [60] that has been extrapolated to zero temperature, plotted as the magenta line in Figure 4.7 (B). See Appendix 6.5 for details of this extrapolation. Such a comparison is particularly useful because the superconducting condensate gives no contribution to the specific heat regardless of the order parameter symmetry– the specific heat is sensitive only to quasiparticles. On the other hand, the NMR shift is sensitive to both the magnetic response of quasiparticles, as well as a possible response from the condensate (which is expected only for the odd parity case). From inspection of Figure 4.7 (B), the field dependence of the shift data is indistinguishable from that of the heat capacity over the entire field range measured. As such we find no resolvable contribution to the spin polarization from the superconducting condensate. Taking into account experimental uncertainties associated with the field orientation (see Appendix 6.3), a conservative upper bound can be placed on the condensate magnetic response of less than 10% that of the normal state.

4.2.3 Discussion

To summarize, after carefully eliminating the effect of systematic RF heating we find the reduction of the spin part of the NMR shift in the superconducting state to be $\approx 20\%$ of its normal state value at the lowest fields measured. Comparison of the normalized K_s as a function of applied in-plane field to that of reported specific heat finds no systematic difference. From this we conclude a maximum possible magnetic response from the superconducting condensate of only 10% the normal state value. Odd parity states with $\mathbf{d} \parallel c$ were ruled out by the strain dependent shift measurements detailed in the last section, but the data presented here allows us to place even stronger constraints on possible order parameters. Helical states with in-plane d-vector are expected to have a condensate polarizability of 50% compared to the normal state, which is further reduced to $\sim 30\%$ when the Fermi liquid corrections appropriate to Sr_2RuO_4 are considered [34]. However, this is still significantly larger than the maximum condensate response consistent with our observations. More extreme proposals, such as a d-vector that spontaneously aligns along one of the in-plane axes or is

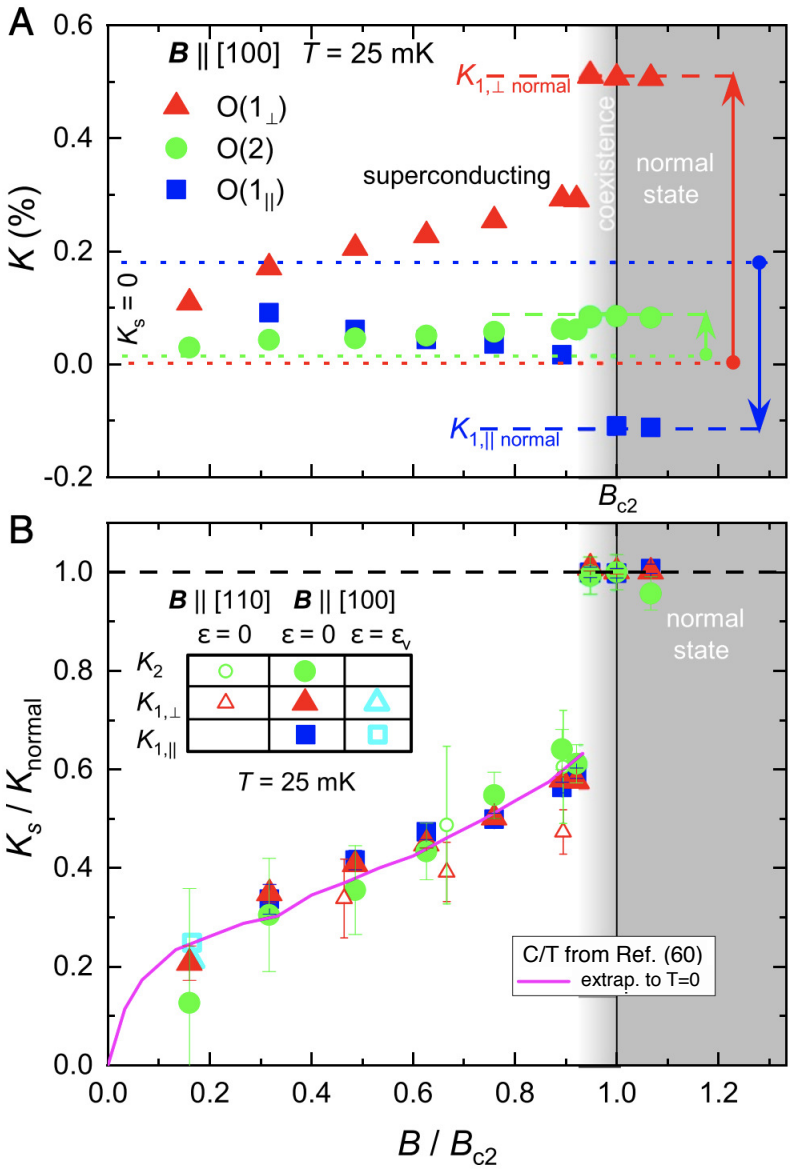

Figure 4.7: **(A)** NMR shifts $K = K_o + K_s$ determined from Figure 4.6 after subtraction of the quadrupolar contribution, plotted as a function of normalized field B/B_{c2}. The $K_s = 0$ position is indicated by dotted lines at finite shift values due to the orbital contribution at each site. **(B)** The field dependent reduction in NMR Knight shift magnitude $|K_s|$ compared to specific heat data [60] that has been extrapolated to $T = 0$ (see Appendix for details), where all quantities are normalized to the normal state. Data taken with **B** $\parallel$ [100], **B** $\parallel$ [110] as well as $\varepsilon_{aa} = \varepsilon_v$ all coincide with the normalized heat capacity.

completely free to rotate, are also excluded by our measurements using both [100] and [110] field directions. We therefore assert that our measurements have ruled out all possible pure triplet order parameters for superconducting Sr_2RuO_4.

4.3 Final Conclusions and Outlook

The assumption of a chiral odd parity superconducting state in Sr_2RuO_4 has colored the interpretation of experimental reports for over two decades. As such, this work represents a large step forward for the community in resolving the mystery of superconductivity in Sr_2RuO_4. The NMR results presented in these two experiments are fundamentally incompatible with not only the chiral state, but all other pure p-wave states, demanding a complete reevaluation of the possible superconducting order parameters. Indeed, abandoning odd parity superconductivity does relieve some tension in the collection of experimental reports detailed in Chapter 2.3, but a single order parameter that can account for all observations is still not obvious.

Evidence for TRSB and multi-component superconductivity has been found using multiple different experimental approaches. Therefore, a successful theory of superconductivity in Sr_2RuO_4 should be able to account for this. Taking all triplet states out of consideration, only the E_g state from Table 2.3 is left which breaks TRS. However, the dependence on k_z in that state implies the pairing strength depends on the inter-layer coupling [20], making it an unappealing option for a quasi-2D material like Sr_2RuO_4. Despite this, it has been proposed that momentum dependent spin-orbit coupling may be able to stabilize a state with this symmetry [75]. The other way to achieve TRSB would require a degeneracy of two single-component order parameters belonging to different irreducible representations of the D_{4h} point group. Such a scenario has also been proposed [40], but necessitates that the transition temperatures of the two order parameters align accidentally. Relying on this fine-tuning is also unappealing; however, rich competition between phases is a hallmark of many body physics and perhaps such an "accidental" degeneracy is not out of the question. More

problematic for both of these proposed theories is incompatibility with recent specific heat measurements [44] which did not resolve a split superconducting transition under anisotropic strain, despite the high precision of their measurements. A possible route to TRSB without a thermodynamic double transition has been proposed focusing on line defects in a bulk $d_{x^2-y^2}$ superconductor [79]. This scenario would explain the lack of heat capacity anomaly as well as the μSR results and place Sr_2RuO_4 into the same class of d-wave superconductors as the cuprates.

Distinguishing between these possibilities will require even more careful experimentation from the community and promises another exciting era of research on Sr_2RuO_4. The development of in-situ strain techniques have been a powerful new tool for attacking the system, including being the starting point for our own project. Looking forward, a great deal could still be learned from phase sensitive measurements directly probing the order parameter symmetry, which were crucial in establishing the pairing symmetry of the cuprates. To conclude, Sr_2RuO_4 remains the cleanest and most well-characterized example of unconventional superconductivity to date. As such, identifying its pairing mechanism and symmetry is crucial for a holistic understanding of these exotic systems.

CHAPTER 5

Experimental Results on the Normal State

5.1 Tuning the Fermi Liquid Crossover via Uniaxial Stress

Controlling the Fermi energy relative to the van Hove singularity (E_{vHs}) in Sr_2RuO_4 has remarkable effects on the normal state properties, such as more than doubling the superconducting critical temperature and causing a breakdown of Fermi liquid behavior [74, 5]. The following results show by way of ^{17}O NMR Knight shift measurements that the Fermi liquid crossover scale in Sr_2RuO_4 can be smoothly tuned to vanishing temperature under applied uniaxial stress along [100]. The crossover scale is shown to be proportional directly to $E_F - E_{vHs}$ and this is rationalized in the context of well defined quasiparticles near a singularity in the density of states. This interpretation is supported by theoretical calculations performed by collaborators [15] via a quasiparticle model incorporating both renormalizations and enhanced spin-orbit coupling. The excellent agreement of the model with our measured data implies only a mild strain dependence of the quasiparticle mass enhancements even very close to the van Hove singularity, contrary to expectations for a quasi-2D correlated metal.

5.1.1 Methods

5.1.1.1 Sample Preparation

Samples from the first growth batch described in Chapter 4.1.1 were used here.

5.1.1.2 NMR under strain setup

The sample was mounted in a smaller Razorbill CS120 strain cell due to size constraints from the cryostat. Stress was applied along the [100] crystal direction. An NMR coil was wound around only the middle section of the sample between the clamps such that approximately half of it was covered in order to achieve higher strain homogeneity [4]. A top-tuning tank circuit configuration was constructed.

5.1.1.3 Cryostat

In order to cover a wide range of temperatures significantly higher than the boiling point of ^{4}He an Oxford Instruments Variable Temperature Insert (VTI) cryostat was employed, capable of operating between $\sim 2 - 300$K.

5.1.1.4 Quadrupolar Shift Analysis

As in the previous experiments, the quadrupolar contribution to the NMR shift has been subtracted out in the plotted data.

5.1.2 Results

Central transition ^{17}O Knight shift measurements were performed as a function of a-axis strain over a temperature range 1.5-50K and applied fields of $B = 3$T and $B = 8$T. All strains are referenced to the critical value ε_v corresponding to the vHs, at which the Knight shift goes through a pronounced maximum [46]. The results are shown in Figure 5.1, with the two in-plane oxygen sites labeled as in Chapter 4.1. Strain is seen to have a pronounced effect on the temperature dependence of the normal state shifts, especially for the O(1) site ($K_{1||}$). In the unstrained data (black), an extremum is observed for both sites around 40K before the shift becomes temperature independent, as expected for the Fermi liquid state below

$T_{FL} \sim 30$K. As a-axis stress is applied ($\varepsilon_{aa} = 0.60\varepsilon_v$, red), the crossover to temperature independent shift behavior is reduced to lower temperature. Then, at the critical value of strain corresponding to the Lifshitz transition ($\varepsilon_{aa} = \varepsilon_v$, green), the crossover extends to the lowest temperatures measured. Additionally, at $\varepsilon_{aa} = \varepsilon_v$ and sufficiently low temperature, the shifts develop strong non-linear field dependence shown in the inset as well as the blue data points, corresponding to Zeeman splitting of the singularity. Both the normal state

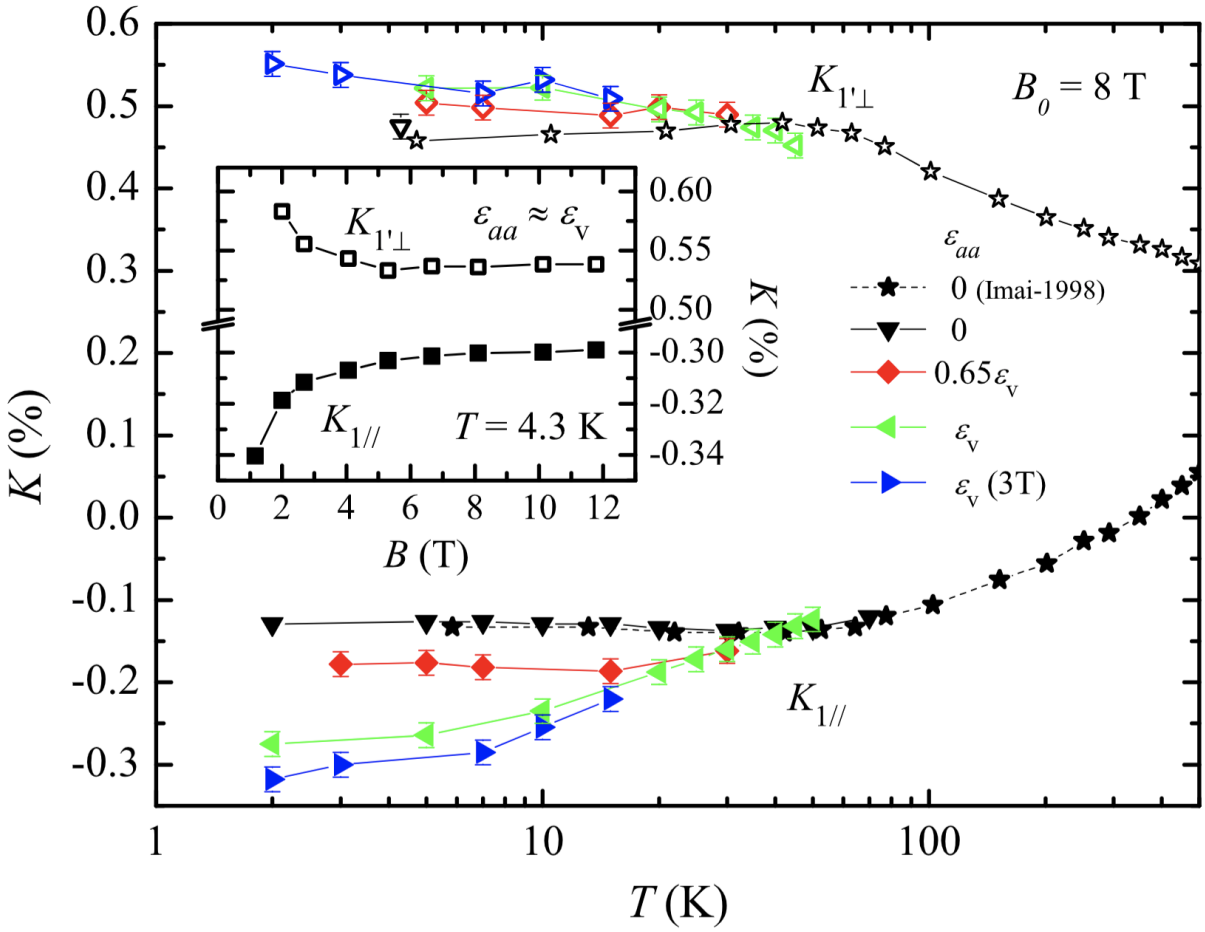

Figure 5.1: **(Main)** ^{17}O Knight shift for both in-plane sites as a function of temperature and strain. Shift data is taken at a field of 8T, except for the blue points which are measured at 3T. **(Inset)** Shift vs field data from [46]. Strong non-linear field dependence develops near critical strain and low field.

temperature dependence of the unstrained shifts and the behavior of the crossover scale under strain can be interpreted in terms of the γ band proximity to the vHs. For strains lower than the critical one, $E_{vHs} - E_F > 0$. Thus, if k_bT is smaller than this energy scale, states at the vHs are no longer thermally accessible and the effective DOS (and thus the magnetic response) becomes roughly constant in temperature. At the critical strain, $E_{vHs} = E_F$, which explains both the enhancement of the shift magnitude and the vanishing of the crossover scale. The approximately logarithmic temperature dependence above T_{FL} can then be understood as a consequence of the logarithmic singularity in the DOS expected from the two-dimensional square lattice.

5.1.3 Theory Collaboration

For a more quantitative analysis, our theory collaborators Manuel Zingl, Jernej Mvralje, and Antoine Georges analyzed a quasiparticle Hamiltonian using renormalized 3-band Wannier models constructed from DFT calculations, taking into account the temperature dependent quasiparticle renormalizations $Z(T)$ [41] as well as enhanced spin-orbit coupling. The non-interacting spin susceptibility χ^{qp} for each of the t_{2g} orbitals in the model is then calculated by adding a magnetic field term in the linear response regime. Results at different strains are obtained by directly changing the lattice parameters of the structure. Importantly, strain dependence of the renormalizations or the Fermi liquid interactions are not considered. Only the effect of strain on the quasiparticle dispersion is included. For specifics on the DFT calculation, see the methods section of [15]. The main results are shown in Figure 5.2 (a). The computed xz and yz susceptibilities, associated with the α and β band, are only weakly strain and temperature dependent due to their featureless DOS. In contrast χ^{qp}_{xy}, associated with the γ band, depends strongly on both temperature and strain as expected from its close proximity to the van Hove singularity. As temperature is lowered, χ^{qp}_{xy} increases before leveling off at a low temperature plateau for all strains except the critical one. The temperature of this crossover is seen to get progressively lower as ε_{aa} approaches ε_v, mirroring the NMR

shifts.

5.1.4 Discussion

In order to make an appropriate comparison with the calculated spin susceptibility, the orbital contributions to the measured NMR shifts are also subtracted out. The resulting spin part of the shift K^s is due to dipolar coupling to the oxygen p-orbitals, and thus depends on the both the xy and xz/yz susceptibilites [30, 59]. For the unstrained geometry the dipole coupling to the xz/yz orbitals is identical for both in-plane sites, while for the xy orbital it is twice as large for the O(1′) site relative to the O(1) and has opposite sign. Thus, to isolate χ_{xy}, the $K^s_{1\perp}$ and $K^s_{1||}$ are subtracted, canceling the contribution from the out-of-plane orbitals. The experimentally measured $K^s_{1\perp} - K^s_{1||}$ is shown in Figure 5.2 (b). It should be noted, however, that under strained conditions the analysis becomes more complicated because the p_x and p_y orbitals are no longer equivalent. Due to the strongly momentum dependent DOS, the p_x orbitals have a far greater overlap with the γ band wavefunction at the $\mathbf{k} = (0, \pi)$ point in the Brillouin zone [46], resulting in the stronger response of $K_{1||}$ to strain (The inset accounts for the different dipolar coupling to χ_{xy} between the sites and thus represents an average of the γ band states near E_F). For more details see Appendix 6.6.

Comparing the calculated quasiparticle susceptibility χ^{qp}_{xy} to the measured $K^s_{1\perp} - K^s_{1||}$ in Figure 5.2 (a) and (b), we find good semi-quantitative agreement. At zero strain there is a crossover from approximately logarithmic temperature dependence to temperature independent behavior in both. In the unstrained case, the crossover to T-independent behavior (T_{FL}) is seen around 20K in the calculation compared to 40K in the measured data. However, this can be explained by an underestimation of $E_{vHs} - E_F \approx 7$meV inherent to the DFT calculation (experiments suggests a value of ~ 13meV [68]). The measurement and calculation also show the same qualitative behavior with strain: as ε_{aa} is increased the crossover temperature is reduced until vanishing at the critical strain where $E_F = E_{vHs}$. The low temperature enhancement of the xy susceptibility at the critical strain also has

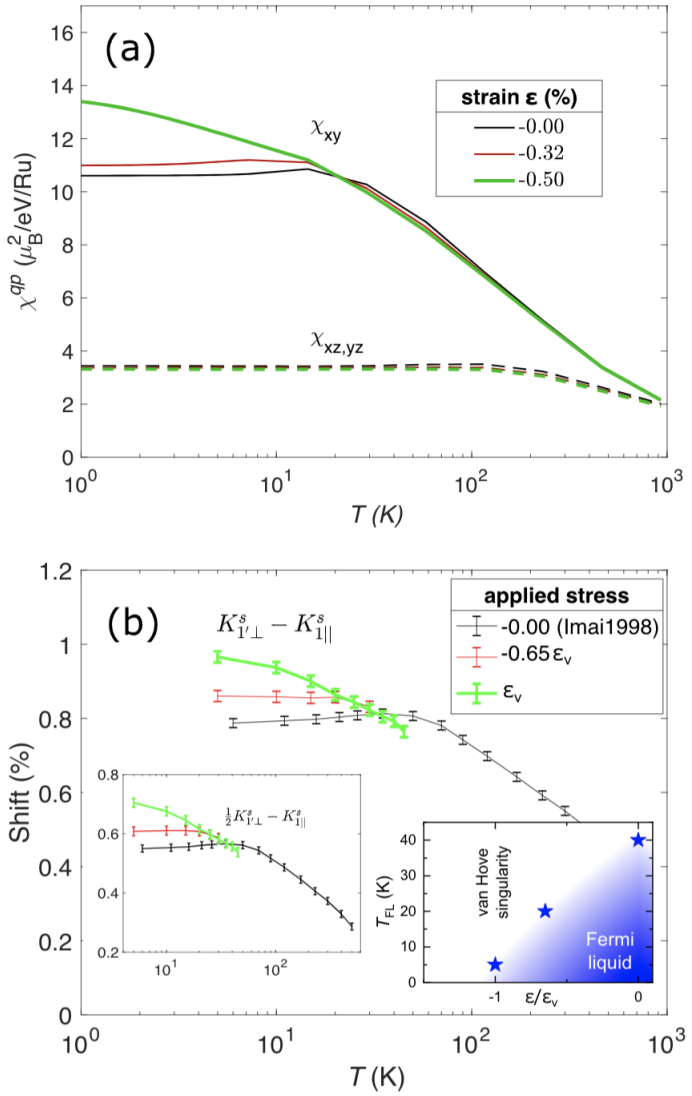

Figure 5.2: **(a)** Numerically calculated susceptibility evaluated from the quasiparticle Hamiltonian as a function of temperature and a-axis strain. The contributions from each of the t_{2g} orbitals are shown separately. $\varepsilon = -0.50\%$ corresponds to the critical strain of the model. **(b)** Experimentally determined $K^s_{1'\perp} - K^s_{1||}$ as a function of temperature and applied stress, where K^s denotes the spin part of the total shift. Interpolated shift data from Figure 5.1 was subtracted after removing the known orbital contribution. The lower right inset shows the evolution of the observed crossover to constant shift.

good quantitative agreement, with a 17% enhancement found in χ^{qp}_{xy} compared to a 23% enhancement in the measured $K^s_{1\perp} - K^s_{1||}$ at 4K.

5.1.5 Conclusion

All the salient qualitative behavior of the measured ^{17}O Knight shift data is reproduced by the theoretical quasiparticle model, including semi-quantitative predictions of the shift enhancement. This is strong evidence that the observed Fermi liquid crossover scale and the logarithmic temperature dependence of the shifts are dominated by the effect of a quasi-2D singularity in the DOS on the quasiparticle dispersions. Our analysis shows this picture is valid over a huge range of temperature and strain, applying even to the unstrained material. This idea is consistent with measurements of transport under strain [5], which were shown to be well described by a Boltzmann model of transport for quasiparticles near a vHs [24, 72]. Moreover, the success of the quasiparticle model despite ignoring the effects of strain on the mass enhancements is quite surprising, as they are expected to also grow logarithmically as the singularity is approached. A mild dependence of Z on strain was previously observed in studies on doped samples [68] and thin films [13], although both methods are expected to significantly broaden the singularity with introduced disorder. Here we find a similar result under anisotropic strain where the level of disorder is smaller and the vHs correspondingly sharper. Indeed, the observed dependence of the NMR shifts on applied field confirm the singularity remains sharp on energy scales comparable to the Zeeman splitting even at the critical value of applied stress. This unexpected result warrants further investigation by probes directly sensitive to the mass enhancement, such as quantitative specific heat measurements or ARPES under strain.

5.2 Magnetism Beyond the Lifshitz Transition

Unconventional superconductivity is typically associated with pairing mechanisms beyond the standard electron-phonon interaction of conventional superconductors. In particular spin fluctuations are thought to be important for the cuprate superconductors due to their antiferromagnetic ground states at low doping. Sr_2RuO_4 on the other hand is closely related to compounds which are ferromagnetic, such as $SrRuO_3$, which was original used as intuitive evidence for the case of odd parity pairing. Recently μSR measurements under anisotropic strain reported the onset of magnetic order at strains well past the Lifshitz transition, shown in Figure 5.3, consistent with the formation of an incommensurate spin density wave (SDW) [21]. We show by way of ^{17}O spin-lattice relaxation (T_1) data that there is an appreciable enhancement of fluctuations near the purported magnetic phase boundary. However, the enhanced relaxation does not extend near the superconducting dome in the temperature-strain phase space, making it unlikely to play an important role in the superconducting pairing. Furthermore, no evidence of longitudinal ordered moments is found in the NMR spectra for the applied field geometry, but the possibility of transverse moments is not excluded.

5.2.1 Methods

5.2.1.1 Sample Preparation

Samples from the second growth batch described in Section 4.2.1 were used here.

5.2.1.2 NMR under strain setup

The sample was mounted in the larger Razorbill CS130 strain cell model with stress applied along [100]. This allowed easier access to the higher strains. An NMR coil was then wound around the middle section of the sample between the clamps, such that approximately half of

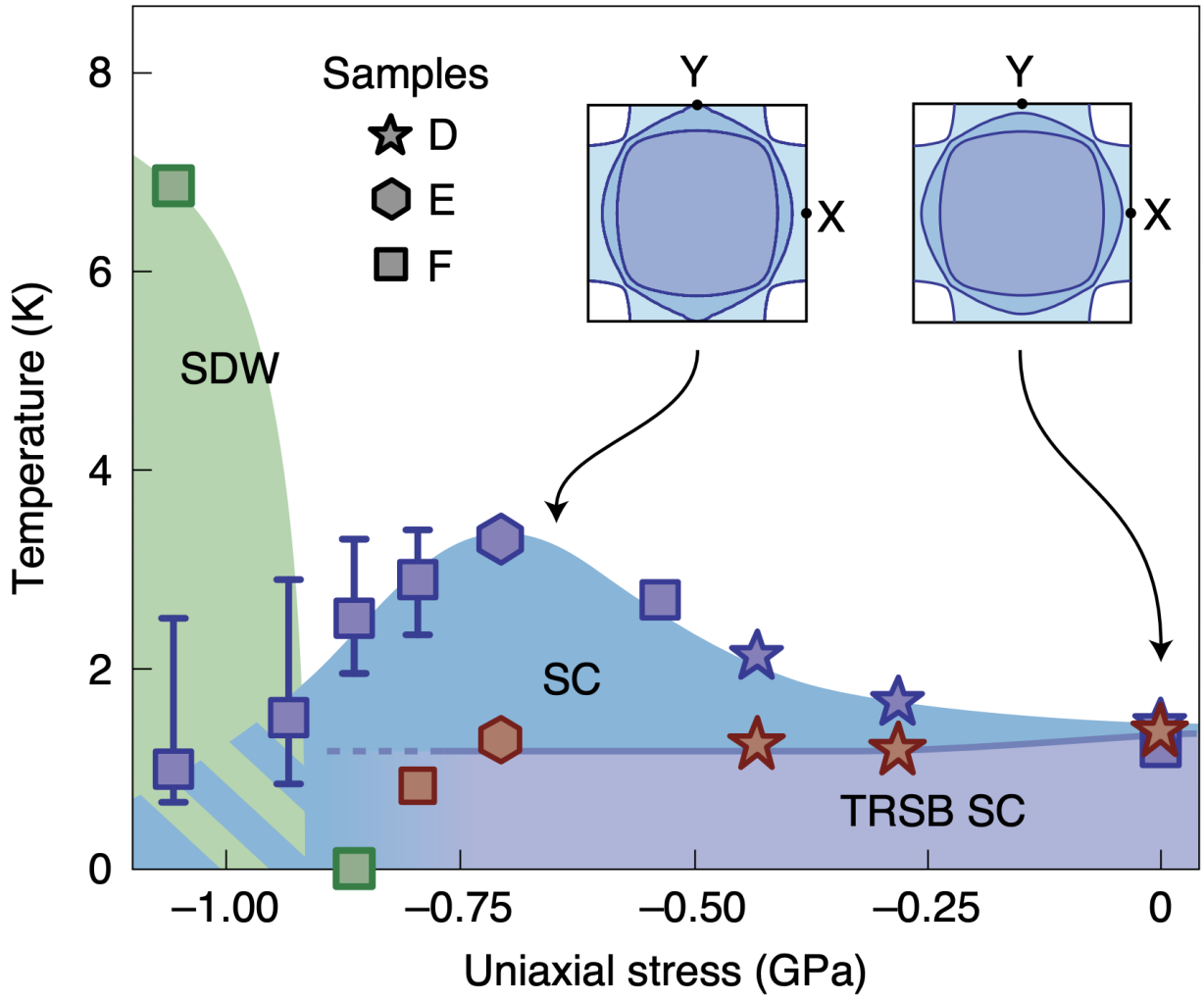

Figure 5.3: Phase diagram deduced from μSR measurements, reproduced from [21]. Blue points mark the superconducting critical temperature, red points the onset of TRSB, and green points the appearance of magnetic order. The Lifshitz transition is observed at an applied stress of about 0.7GPa, evidenced by the maximum in T_c.

it was covered. A top-tuning match configuration was constructed.

5.2.1.3 Cryostat

In order to reach the high strain ordered phase the piezoelectric stacks were subject to voltages exceeding 200V. This presented a risk of dielectric breakdown through the low pressure helium gas found in typical variable temperature inserts. As such an Oxford Instruments Heliox cryostat was employed allowing the sample and strain cell to be mounted in vacuum. The cell was thermally anchored to the bottom of a closed Helium-3 space, which was then coupled to the main Helium-4 bath through a needle valve. A heater on the Helium-3 pot then allowed temperature control between $1.5 - 10$K.

5.2.2 Results

^{17}O Knight shift and T_1 relaxation measurements were taken at variable strains and temperatures with $B = 8.1$T applied along the crystal b-axis. The upper panel of Figure 5.4 shows the shift of the central transition for both in-plane oxygen sites as a function of a-axis strain at a constant temperature of $T = 2.1$K. An initial maximum in the shift magnitude is observed around $\varepsilon_v \sim -0.6\%$ corresponding to passing through the van Hove singularity [46]. As strain is increased further the shift magnitude decreases rapidly before becoming roughly constant at high strain. $1/T_1T$ for the O(1) site is plotted for the same values of a-axis strain in the lower panel of Figure 5.4. A peak in the relaxation rate is first seen around ε_v, also observed in a previous report [46]. A second sharp maximum in $1/T_1$ is then found at a strain higher than those achieved in previous NMR experiments, near $\varepsilon = -0.85\%$. Figure 5.5 shows the temperature dependence of $1/T_1T$ at fixed values of strain. For $\varepsilon = -0.26\%$ (yellow), constant $1/T_1T$ is observed as expected for the Fermi liquid state. For $\varepsilon = -1.00\%$ (orange) the relaxation rate goes through a maximum before returning to the unstrained value. For even higher strains (blue), constant $1/T_1T$ is observed for all the temperatures measured. The

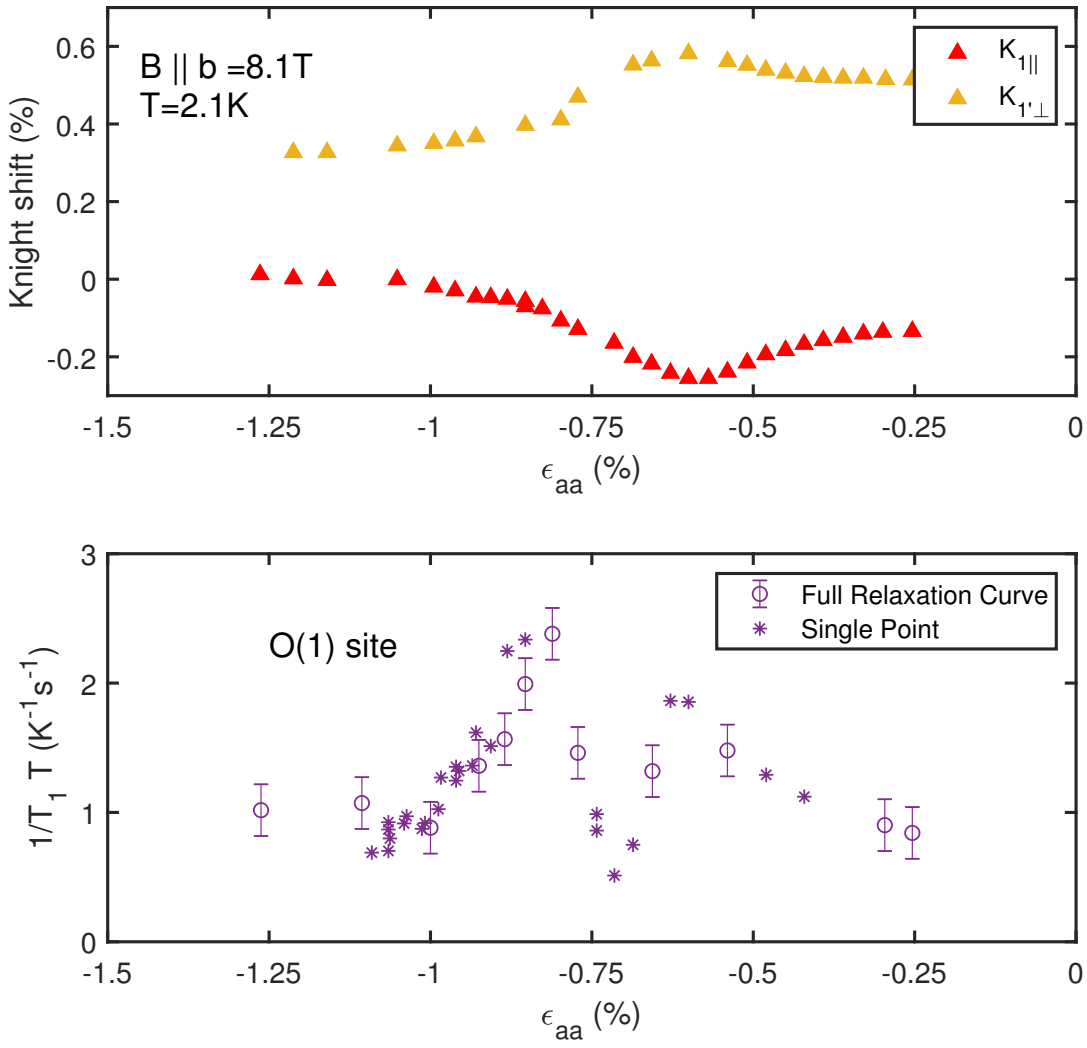

Figure 5.4: **(Top)** NMR Shift as a function of ε_{aa} for both in-plane oxygen sites with field along the b-axis and stress applied along the a-axis. The maximum at $\varepsilon_{aa} = -0.6\%$ corresponds to the γ band passing through the vHs. **(Bottom)** $1/T_1T$ as a function of ε_{aa} for the O(1) site under the same temperature and field conditions as above. The first maximum coincides with the $\varepsilon_{aa} = \varepsilon_v$, while a second singular maximum is seen at $\varepsilon_{aa} = -0.85\%$. The empty symbols correspond to full relaxation curve measurements while the stars are inferred T_1 values from the FFT amplitude after a fixed recovery time.

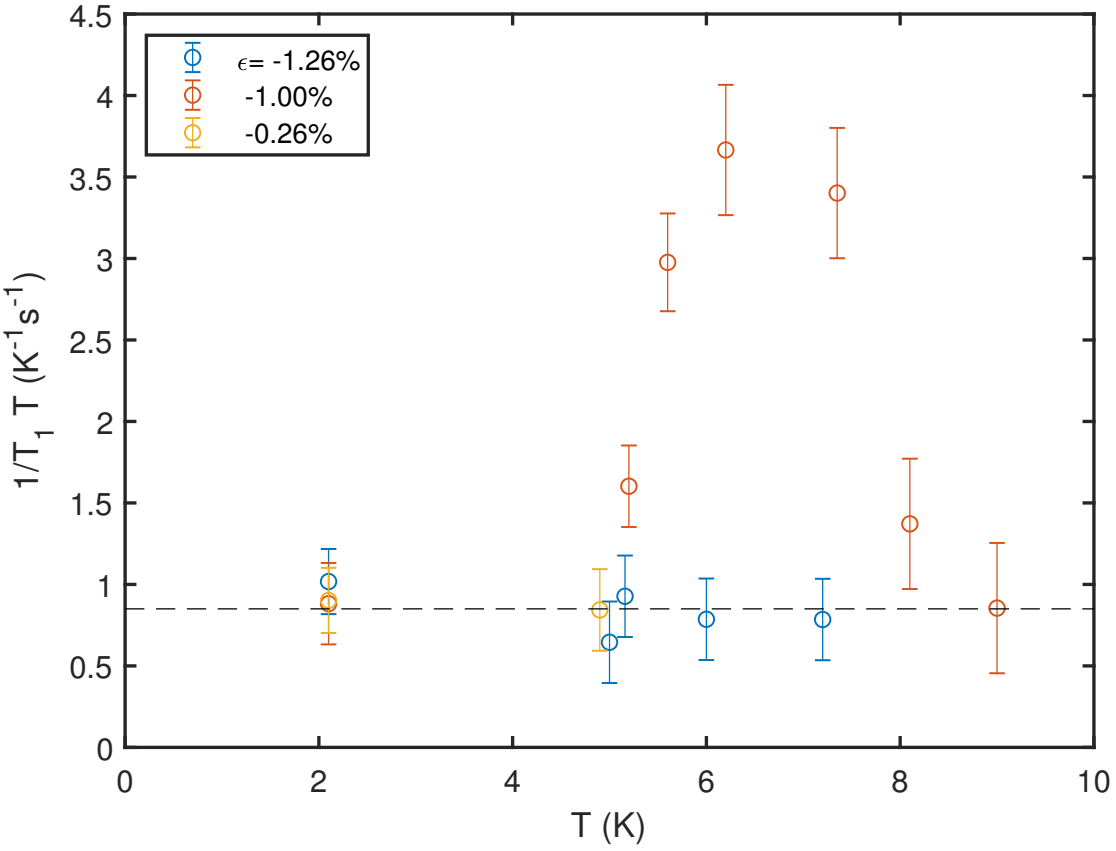

Figure 5.5: $1/T_1T$ data on the O(1) site as a function of temperature at three fixed values of ε_{aa}. An enhancement is found around 7K for $\varepsilon_{aa} = -1.00\%$ (orange), while constant T_1T behavior is seen in this temperature range at both lower (yellow) and higher strains (blue).

temperature and strain conditions of the two observed peaks in $1/T_1T$ are consistent with the magnetic transition boundary reported in μSR as well as elastocaloric measurements [21, 43]. As such, we associate them with enhanced fluctuations originating from the novel high strain phase. However, the characteristic line broadening associated with the onset of magnetic order is not seen, shown in Figure 5.6. The linewidth of the O(1) central transition at the highest strain measured has a full-width at half maximum (FWHM) of 7kHz. This is only slightly broader than the FWHM of 4kHz found in the unstrained spectra. It should be noted that for $0.4\% \lesssim |\varepsilon| \lesssim 1\%$, the linewidths do broaden significantly, seen in the middle spectra of Figure 5.6. However, it is unlikely for this broadening to be magnetic in origin as it is reduced as strain is increased further. Instead, it is consistent with the effects of strain inhomogeneity coupled with the rapidly varying $K(\varepsilon)$ in this region.

5.2.3 Conclusion

The NMR phase diagram concluded from the O(1) $1/T_1T$ data is shown in Figure 5.7. Enhanced relaxation is observed only close to the high strain phase boundary and vanishes well outside the superconducting dome. This suggests that regardless of the origin of the ordered phase, the associated fluctuations are not crucial for the superconducting pairing mechanism. Interestingly, beyond the line of transitions, $1/T_1T$ returns to the temperature independent behavior characteristic of a Fermi liquid. The magnitude of $1/T_1T$ observed at high strains is also equivalent to that found in the unstrained material. This suggests the itinerant quasiparticles dominating relaxation of the unstrained material are still present in the novel phase. No direct evidence for the magnetic transition is found in the NMR spectra and the weak line broadening is consistent only with an exceptionally small ordered moment. However, given the dipolar coupling of the oxygen p-orbitals, the experimental geometry used here would not be sensitive to possible transverse moments, as the corresponding hyperfine fields would be also transverse. Future experiments with the field tilted away from the in-plane axis are necessary to investigate such a scenario.

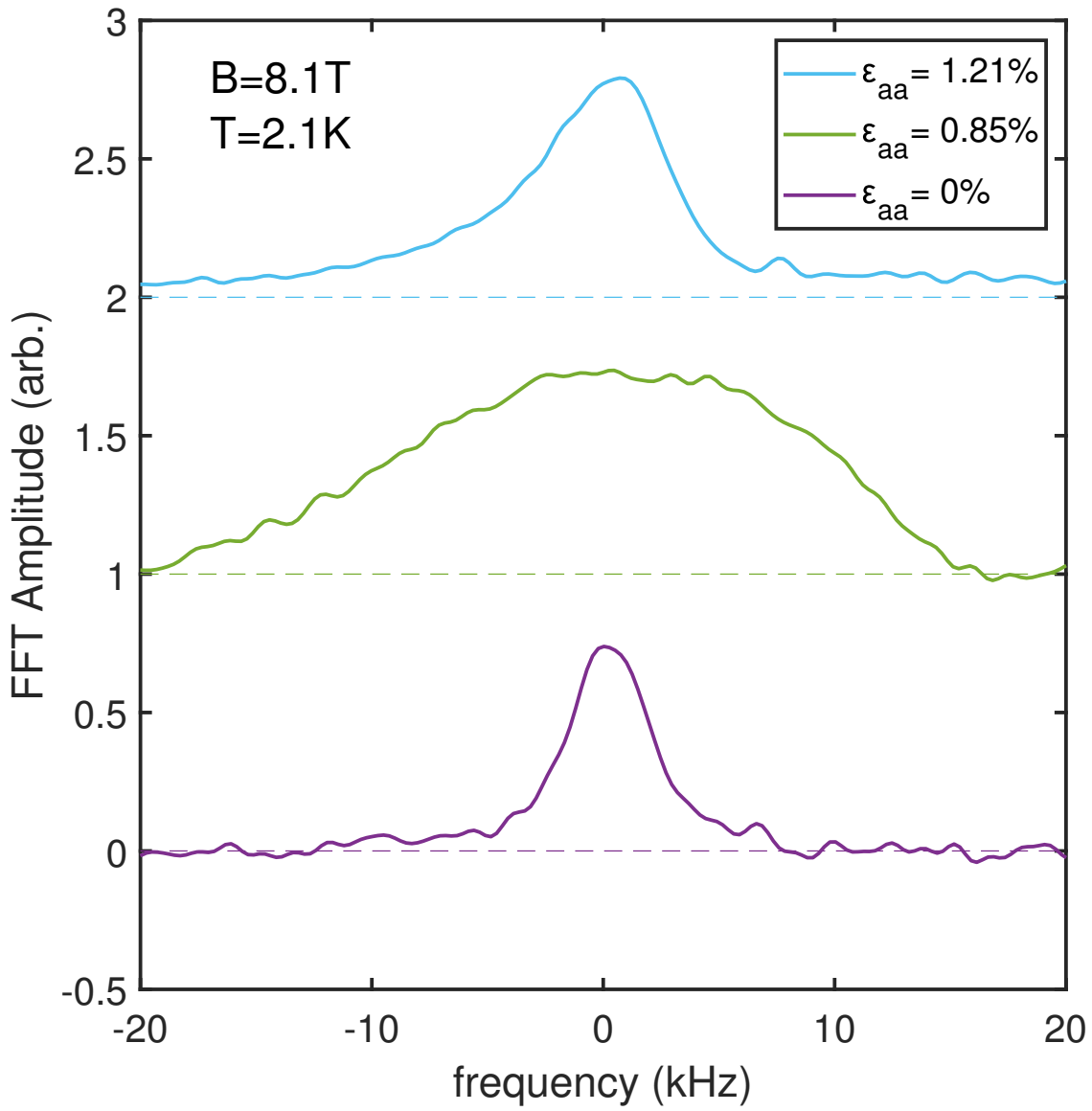

Figure 5.6: O(1) central transition spectra for three characteristic strains. Only a modest broadening of the central transition is seen between the unstrained (purple) material and $\varepsilon_{aa} = -1.21\%$ (blue), despite the latter being far beyond the phase boundary characterized by enhanced $1/T_1T$. The broader spectra at intermediate strains (green) is attributable to strain inhomogeneity.

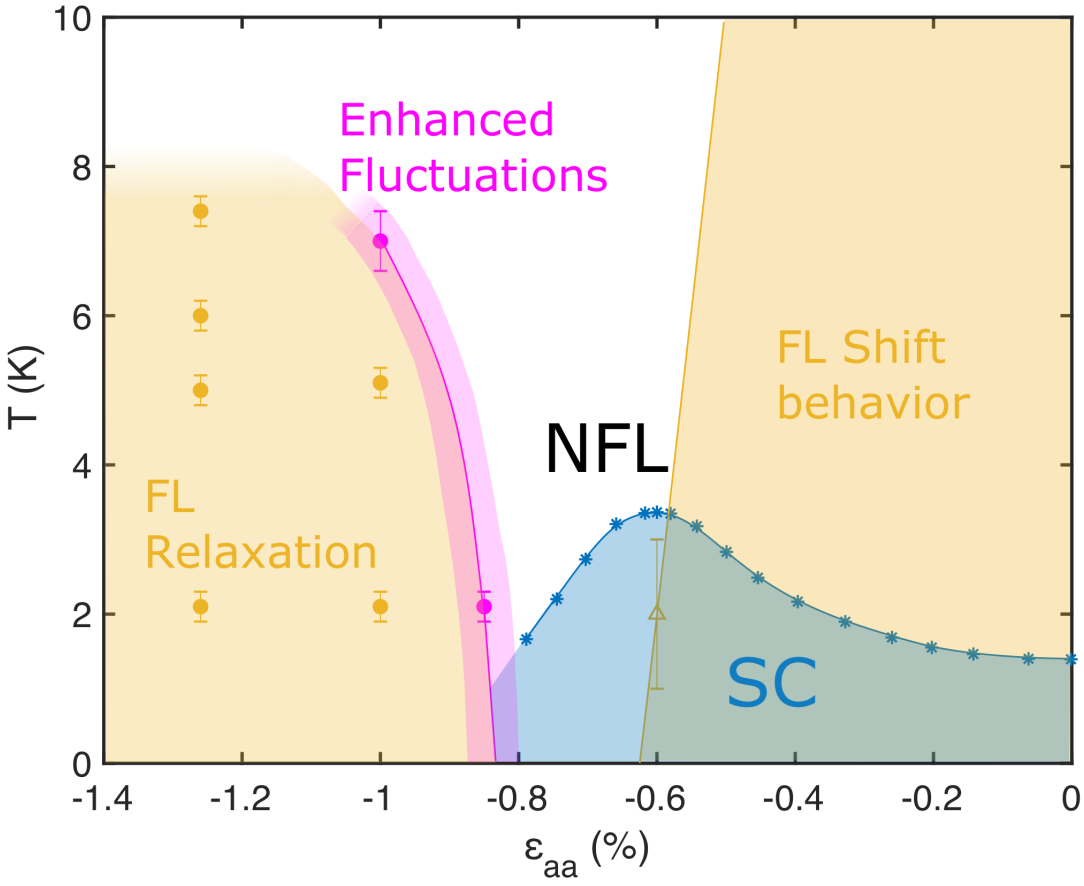

Figure 5.7: Temperature-strain phase diagram of Sr_2RuO_4 deduced from NMR measurements. Yellow triangles are the Fermi liquid (FL) crossover temperature inferred from Knight shift measurements in Chapter 5.1. Purple circles are peaks in $1/T_1T$ relaxation, while yellow circles correspond to constant $1/T_1T$ Fermi liquid behavior. For reference, superconducting transition temperature data (blue stars) has been reproduced from [74].

CHAPTER 6

Appendices

6.1 Numerical Diagonalization of the Nuclear Hamiltonian

The general form of the NMR Hamiltonian of Chapter 4.1.1.5 is given by:

$$H = \gamma \mathbf{I} \cdot (1 + \mathbf{K}) \cdot \mathbf{B} + \frac{eQ}{2I(2I-1)\hbar} \mathbf{I} \cdot \mathbf{V} \cdot \mathbf{I} \tag{6.1}$$

where $\mathbf{I} = [I_x, I_y, I_z]$, $\mathbf{K}$ is the shift tensor, $\mathbf{V}$ is the electric field gradient tensor (EFG), and eQ is the quadrupole moment of the nucleus. Transforming to the principle axis frame of the EFG simplifies this to:

$$H = \gamma \mathbf{I} \cdot (1 + \mathbf{K}) \cdot \mathbf{B} + \frac{\nu_Q}{6} [3I_z^2 - \mathbf{I}^2 + \eta(I_x^2 - I_y^2)] \tag{6.2}$$

where $\nu_Q = \frac{3eQV_{zz}}{2I(2I-1)\hbar}$, $\eta = (V_{xx} - V_{yy})/V_{zz}$, and V_{zz} is defined to be the largest diagonal element of $\mathbf{V}$. The I_i spin operators can be written out explicitly in terms of the Pauli spin matrices, which for a $I = 5/2$ nucleus are given by:

$$I_x = \hbar \begin{pmatrix} 0 & \frac{\sqrt{5}}{2} & 0 & 0 & 0 & 0 \\ \frac{\sqrt{5}}{2} & 0 & \sqrt{2} & 0 & 0 & 0 \\ 0 & \sqrt{2} & 0 & \frac{3}{2} & 0 & 0 \\ 0 & 0 & \frac{3}{2} & 0 & \sqrt{2} & 0 \\ 0 & 0 & 0 & \sqrt{2} & 0 & \frac{\sqrt{5}}{2} \\ 0 & 0 & 0 & 0 & \frac{\sqrt{5}}{2} & 0 \end{pmatrix} \tag{6.3}$$

$$I_y = \hbar \begin{pmatrix} 0 & -i\frac{\sqrt{5}}{2} & 0 & 0 & 0 & 0 \\ i\frac{\sqrt{5}}{2} & 0 & -i\sqrt{2} & 0 & 0 & 0 \\ 0 & i\sqrt{2} & 0 & -i\frac{3}{2} & 0 & 0 \\ 0 & 0 & i\frac{3}{2} & 0 & -i\sqrt{2} & 0 \\ 0 & 0 & 0 & i\sqrt{2} & 0 & -i\frac{\sqrt{5}}{2} \\ 0 & 0 & 0 & 0 & i\frac{\sqrt{5}}{2} & 0 \end{pmatrix} \tag{6.4}$$

$$I_z = \hbar \begin{pmatrix} \frac{5}{2} & 0 & 0 & 0 & 0 & 0 \\ 0 & \frac{3}{2} & 0 & 0 & 0 & 0 \\ 0 & 0 & \frac{1}{2} & 0 & 0 & 0 \\ 0 & 0 & 0 & -\frac{1}{2} & 0 & 0 \\ 0 & 0 & 0 & 0 & -\frac{3}{2} & 0 \\ 0 & 0 & 0 & 0 & 0 & -\frac{5}{2} \end{pmatrix} \tag{6.5}$$

This allows Equation 6.2 to be computed in matrix form, parameterized by ten quantities: ν_Q, η, the six independent elements of $\mathbf{K}$, and two angles describing the direction of $\mathbf{B}$ in the EFG frame, θ and ϕ. Numerical diagonalization of the nuclear Hamiltonian in Matlab then gives the six eigenstates and corresponding eigenenergies. For the typical fields used in NMR measurements the Zeeman term will dominate the quadrupolar term, so the full eigenstates will be very nearly eigenstates of $\hat{\mathbf{B}} \cdot \mathbf{I} = I'_z$, where z' is taken to be the direction of the magnetic field in the lab frame. Since the rotating B_1 field of the NMR coil is perpendicular to z', only transitions with nonzero matrix elements $\langle j | I'_\pm | k \rangle$ are allowed. This selection rule enforces $\Delta m' = \pm 1$ where m' is the eigenvalue of I'_z. Thus, for each distinct spin 5/2 nucleus, five observable NMR transition frequencies can be calculated by taking the difference between adjacent eigenenergies of the full Hamiltonian (these will be the only transitions to satisfy the selection rule).

Before application of the magnetic field there are two distinct oxygen sites in Sr_2RuO_4 labeled O(1) for the planar oxygen and O(2) for the apical one. The principle axes of the EFG

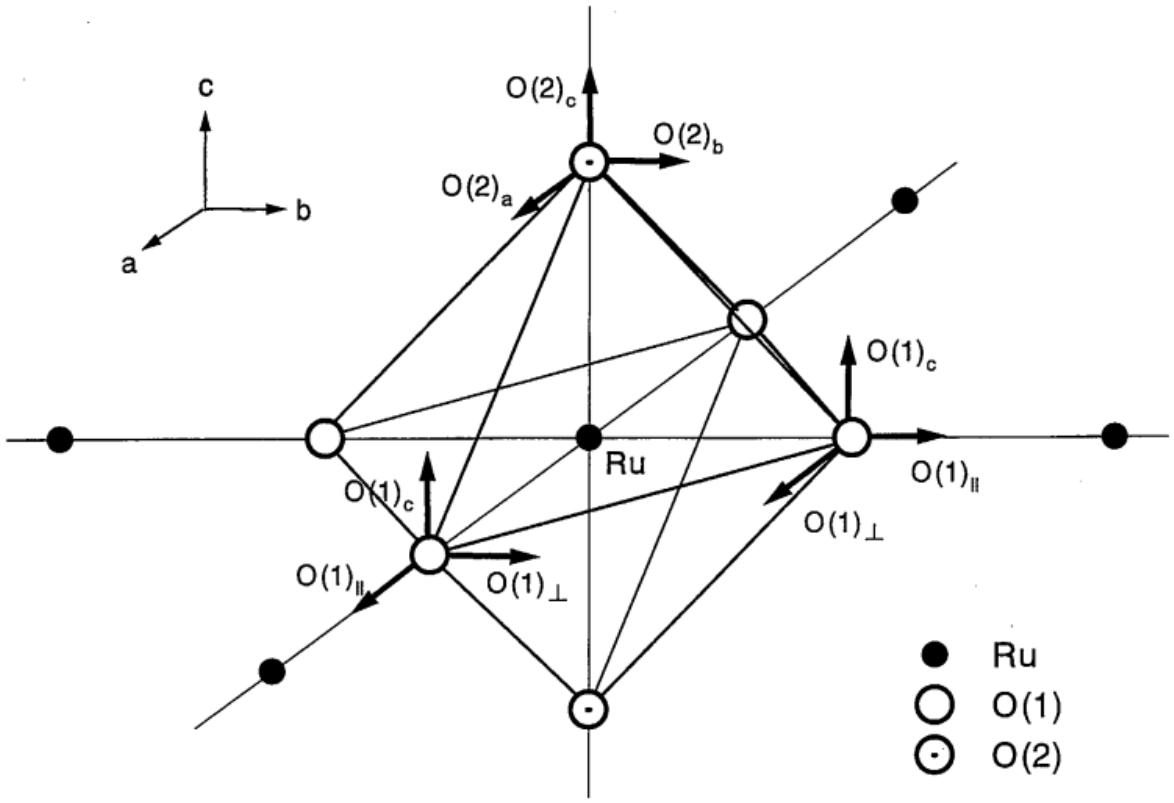

Figure 6.1: Principle axes of the shift and EFG tensors for the two distinct oxygen sites in Sr_2RuO_4. The axis corresponding to V_{zz} points along the out-of-plane direction for the O(2) site and along the Ru-O bond direction for the O(1) site. Reproduced from [59].

and shift tensor are known to be co-linear, shown in Figure 6.1, with V_{zz} along the Ru-O bond direction for the O(1) site and along the out-of-plane direction for the O(2) site [59]. The shift and quadrupolar parameters specific to each site have also been determined previously [59, 46]. The strain dependence of these parameters is also known [46] and is reproduced in Figure 6.2. For fields applied in the Ru-O planes, only one component of the shift tensor K_{2ab} is necessary for the axially symmetric apical site and only two ($K_{1\parallel}$, $K_{1\perp}$) for the in-plane site. The actual parameters used in the calculation of the normal state transition frequencies in Chapters 4 and 5 were verified experimentally by fitting the numerical calculation to the full measured spectrum of 15 lines and are given in Table 6.1.

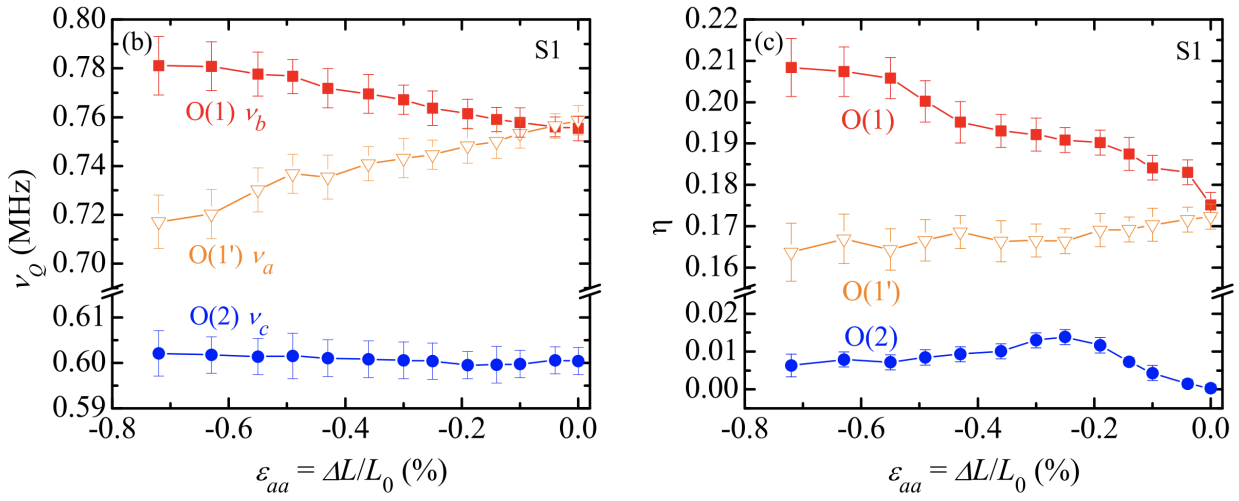

Figure 6.2: Evolution of ν_Q **(left)** and η **(right)** for the oxygen sites in Sr_2RuO_4 as a function of a-axis strain. The subscript of ν denotes the crystal axis corresponding to V_{zz} for each site. The Lifshitz transition was estimated as $\varepsilon_{aa} = -0.6\%$ in this work. Reproduced from [46].

6.2 Strain Dependence of Superconducting ^{17}O Knight shift

The central transition Knight shift for the two in-plane oxygen sites measured as a function of a-axis strain in the interval $[0, \varepsilon_{aa}]$ is shown in Figure 6.3 for both the normal and superconducting state. The strain dependent parameters of Figure 6.2 were used to subtract

	Shift (%)	NQR frequency (MHz)	Asymmetry
O(1)	$K_{1\|\|} = -0.120$ $K_{1\perp} = +0.509$	$\nu_Q = 0.765$	$\eta = 0.174$
O(2)	$K_{2ab} = +0.082$	$\nu_Q = 0.6065$	$\eta = 0$

Table 6.1: Nuclear Hamiltonian parameters for the two distinct oxygen sites in unstrained Sr_2RuO_4 used to compute the quadrupolar shift contribution.

out the quadrupolar contribution at each value of ε_{aa}. A reduction in the magnitude of the Knight shift in the superconducting state compared to that of the normal state is resolved as the critical strain is approached. This data was taken using full $\pi/2$-π echo pulses, which were shown in Chapter 4 to cause significant heating of the sample. As such, the shift reduction is only resolved near ε_v where T_c becomes sufficiently large to probe the superconducting state. Nevertheless, despite this systematic uncertainty in the magnitude, the evolution of the superconducting shifts is smooth over the entire range of strain with no evidence for a first order phase transition.

6.3 Determining Uncertainty in the Shifts at Low Fields

At typical applied magnetic field strengths greater than about 1T, angular uncertainties in the field direction of a few degrees are negligible. However, at the lowest fields measured in Chapter 4.2 ($B_0 = 0.24$T), the strength of the Zeeman coupling to the oxygen nucleus is only around $\gamma B_0 \sim 1.4$MHz. In this regime the quadrupolar coupling of $\nu_Q \sim 0.8$MHz is the same order of magnitude and thus represents a substantial contribution to the transition frequency.

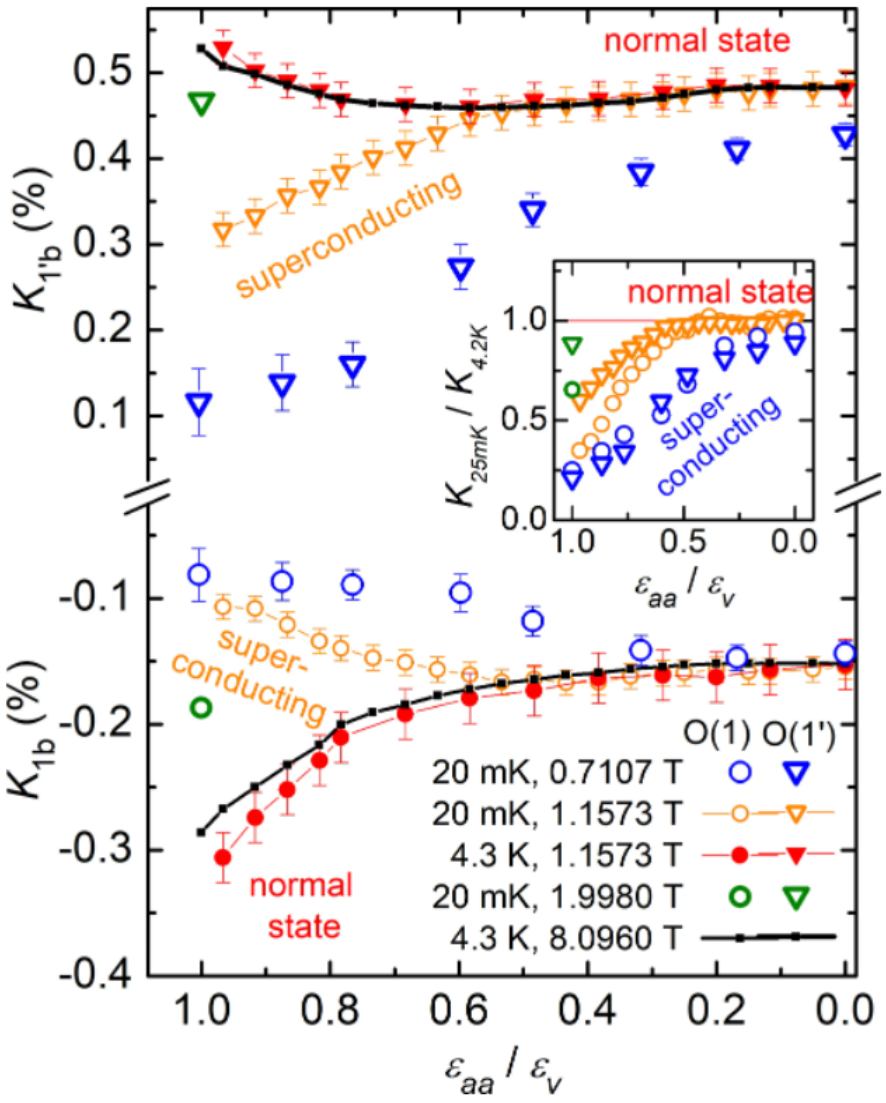

Figure 6.3: ^{17}O Knight shift for the in-plane sites as a function of a-axis strain comparing the normal and superconducting state responses. The red and black points are taken above T_c and show an enhancement of the shift magnitude approaching ε_v. The remaining points are taken at the base temperature of 20mK and show a reduction in shift compared to the normal state at equivalent strains. The reduction evolves smoothly as a function of strain without any signature of a first order phase transition.

As a result, the dominant source of uncertainty at these low fields is caused by uncertainty in the direction of the magnetic field relative to the quadrupolar principle axis frame.

The alignment of the magnetic field into the ab-plane of the crystal was done in-situ by mounting the sample on a piezoelectric rotator. The in-plane condition was then found by measuring the upper critical field B_{c2} as a function of angle, which is known to be maximized for $B \parallel ab$ [81]. A comparison of this calibration with previously reported angular dependent B_{c2} measurements is shown in Figure 6.4.

An initial estimate of the field angle within the ab-plane was done *a posteriori* by inspecting the sample inside the NMR coil, with a deviation of about $\phi = 3 \pm 1^\circ$ found between the field and the crystal a-axis. The extracted K/K_{normal} for various assumed in-plane angles near 3° are shown in Figure 6.5, where the difference between the curves is due to the angle dependence of the quadrupolar contribution that is being subtracted out. $K_{1\parallel}$ has a sensitive dependence on ϕ, with unphysical values observed for $\phi = 0$ and $\phi = 5^\circ$ where it exceeds the normal state value and changes sign respectively. Additionally, further constraining $K_{1\parallel}$ to decrease monotonically over the entire range of measured fields produces a tight constraint on the allowed angles of $\phi = [2.5^\circ, 3.3^\circ]$. $K_{1\perp}$ is much less sensitive to variations in ϕ but still has unphysical behavior for angles deviating far from 3°. Using the angle bounds inferred from the $K_{1\parallel}$ site, $K_{1\perp}$ is very robust with variations of only about 5% the normal state value. It should also be noted that the shift of the O(2) site, not plotted here, is axially symmetric and thus does not depend on the in-plane angle at all. Good agreement between the shifts of the three sites is found only for $\phi = 2.9 \pm 0.4^\circ$, imposing an uncertainty in the magnetization of at most 10%.

6.4 Determining ^{17}O Orbital Shifts

After removing any quadrupolar contribution to the NMR transition frequency, the total shift is given by $K = K_o + K_s$ where K_o is a result of conduction electron orbital motion and K_s

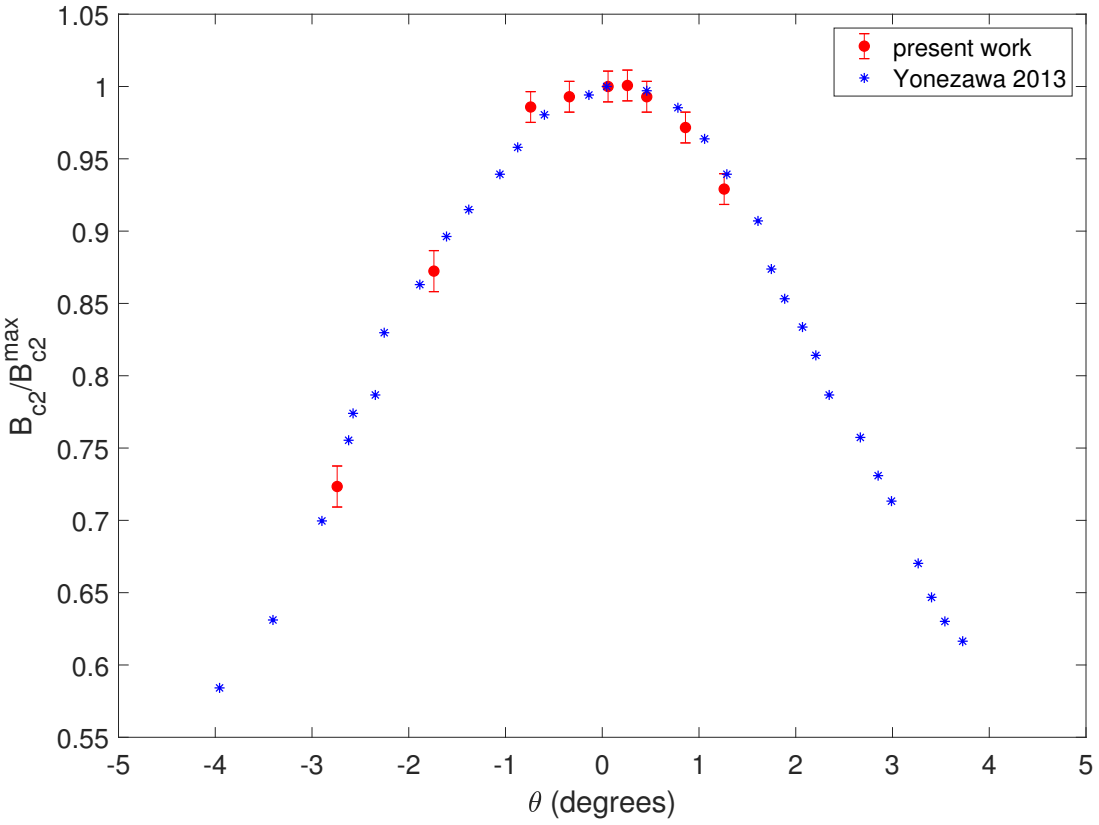

Figure 6.4: B_{c2} normalized to $B_{c2}^{\max} = 1.42$T plotted as a function of out-of-plane angle θ. The superconducting transition was measured using the ac susceptibility method described in Chapter 3.4. There is good agreement with data from [81], which had $B_{c2}^{\max}$ ranging from $1.41 - 1.45$T depending on the sample and field sweep conditions. The uncertainty in the in-plane alignment is estimated as $\pm 0.2^{\circ}$

.

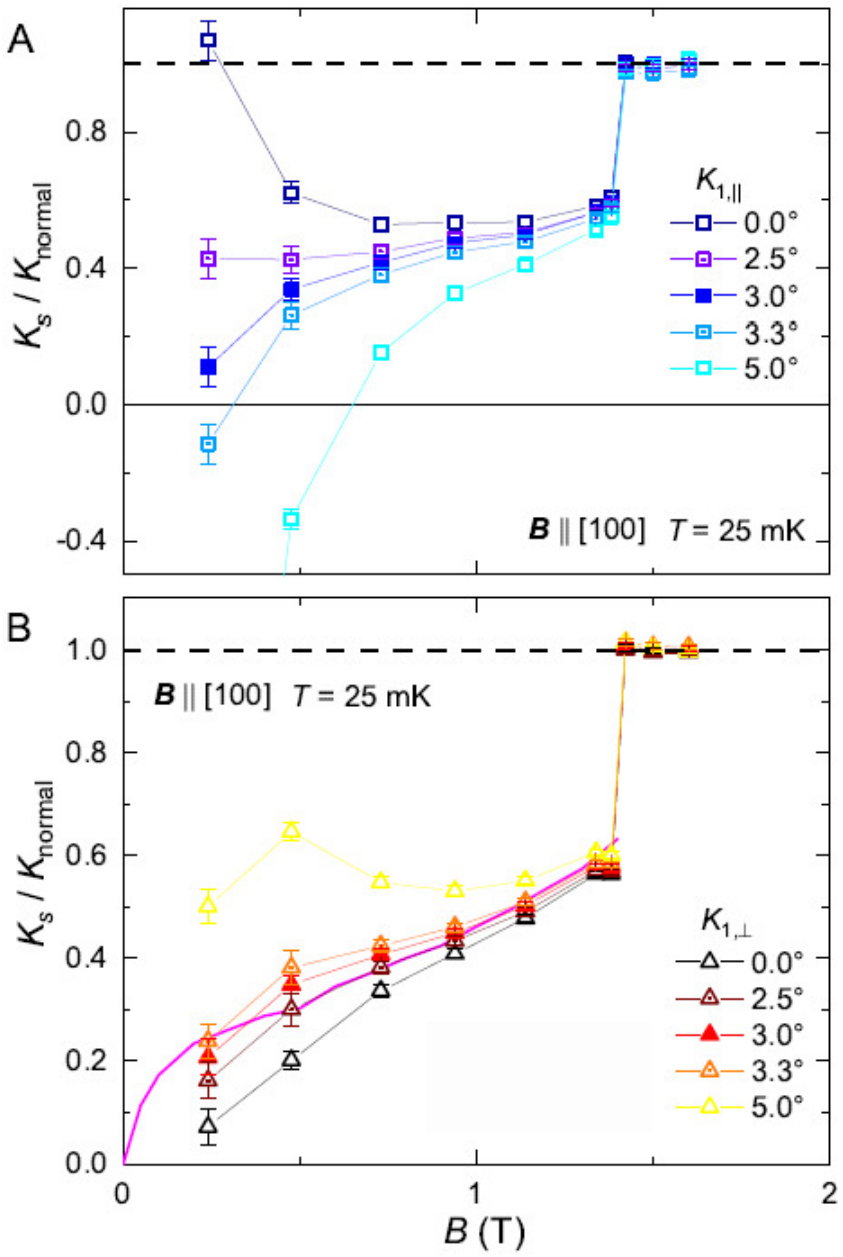

Figure 6.5: Calculated K_s/K_{normal} using various values of in-plane angle ϕ relative to $B \parallel [100]$. **(A)** $K_{1\parallel}$ is extremely sensitive to ϕ with unphysical behavior ($K_s > K_{\text{normal}}$ or $K_s < 0$) seen for $\phi = 0$ and $\phi = 3.3°$. **(B)** $K_{1\perp}$ is more robust due to the larger magnitude of K_s. The magenta line is the $T = 0$ extrapolation of C/T from [60] described in the text.

is the hyperfine shift from which we infer the spin polarization. Orbital shifts are typically measured by plotting the total shift as a function of the spin part of the bulk susceptibility χ_{bulk}. K_o is then extracted by a linear fit via $K = A\chi_{bulk} + K_o$. The results of this procedure reported in [33] found $K_o(1 \perp) \approx 0$ and $K_o(1 \parallel) \approx +0.18\%$, which were used to extract K_s from the total shift in Chapter 4.2. A similar determination was not made for the O(2) site, but has been assumed negligibly small in previous NMR work [30]. Here we take it to be $+0.02\%$, about a quarter of the normal state hyperfine shift, in order to get good agreement of K_s with the in-plane sites.

6.5 Heat Capacity Extrapolation

in Chapter 4.2, the measured Knight shifts are compared to an extrapolation of field dependent specific heat data taken from Nishizaki, et al. [60]. In Figure 6 of that work, C/T is measured as a function of temperature for various values of applied in-plane field. The temperature variation is linear to good approximation and we use this fact to extrapolate the data to zero temperature, plotted as the open magenta squares in Figure 6.6 **(A)**. Also plotted in **(A)** are field dependent specific heat data at various fixed temperatures reproduced from [60]. This plot is inverted in Figure 6.6 **(B)** as a secondary way of extracting the temperature dependence at fixed field. Extrapolating this data to zero temperature is used to create the magenta line plotted in **(A)**. The two methods agree well and this magenta line is plotted in Figure 4.6 of Chapter 4.2.

6.6 Effect of Momentum Dependent DOS on ^{17}O Knight Shift

The effect of applying uniaxial stress in the plane of the Ru-O layers on the band structure is shown in Figure 2.3. The α and β bands are essentially unaffected, while the γ band is

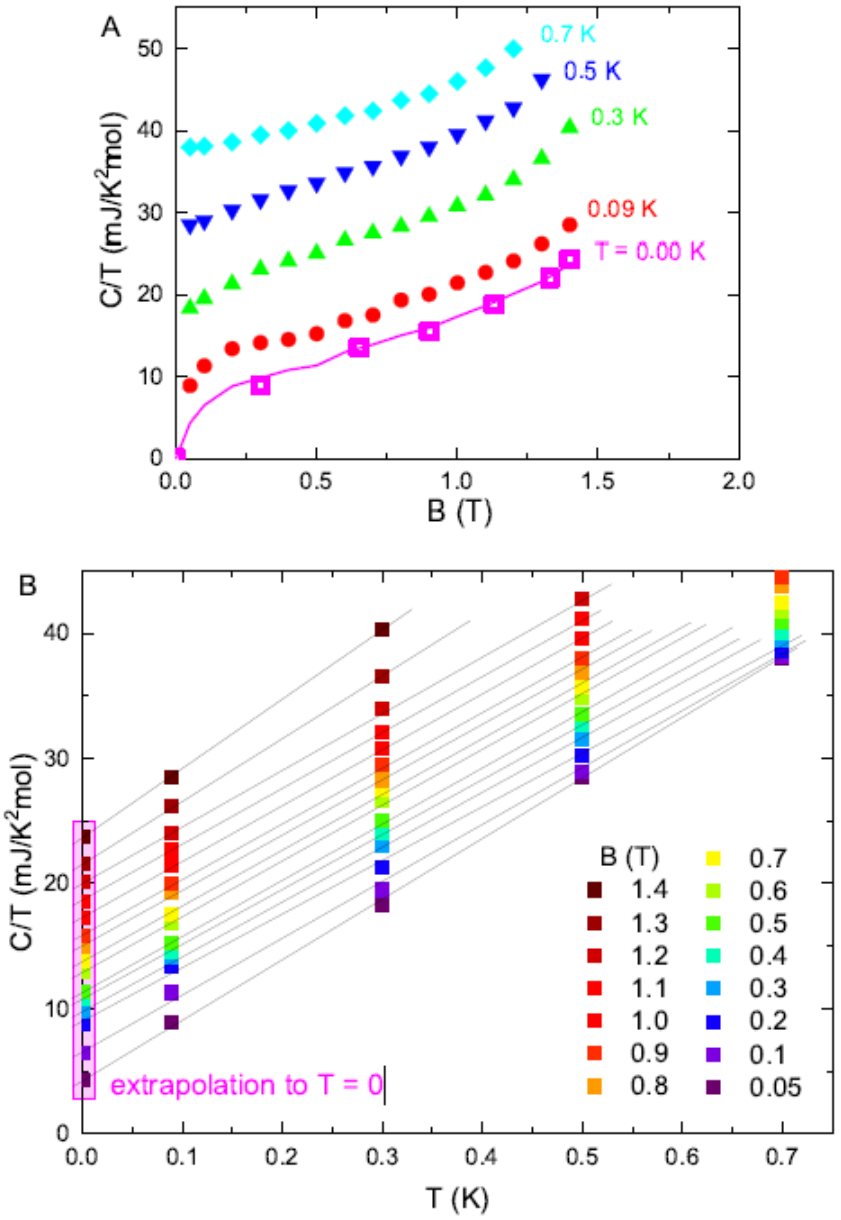

Figure 6.6: The quasiparticle background is determined by a linear extrapolation of specific heat data to $T = 0$. **(A)** C/T versus magnetic field at fixed temperatures reproduced from [60]. The open magenta square are extrapolations to $T = 0$ of specific heat data from Figure 6. of [60]. **(B)** The data points of panel (A) inverted and plotted as a function of temperature. The linear extrapolation of these points to $T = 0$ produces the solid magenta line shown in (A).

distorted through the zone boundary at two points, breaking the C_4 symmetry. The resulting γ DOS then becomes strongly momentum dependent owing to the van Hove singularities at the zone boundary. However, the hybridization of the ruthenium d-orbitals and the oxygen p-orbitals making up the γ band is also momentum dependent. The orbital hybridization at

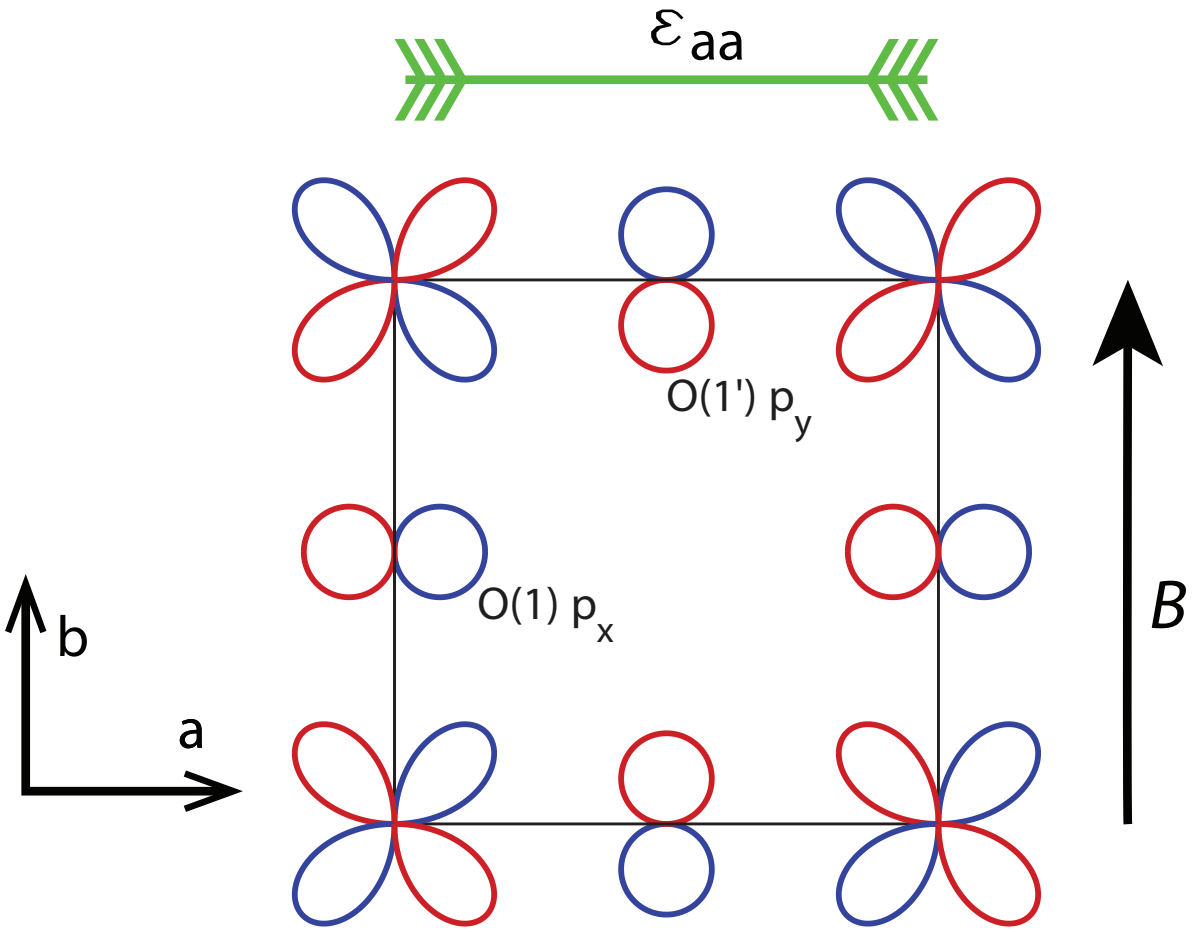

Figure 6.7: Sketch of a Ru-O layer showing the orbital hybridization of the quasi-2D γ band at the $k = (0, \pi)$ point in the Brillouin zone. Phases of the orbitals are marked by the coloring. The overlap of the Ru-d_{xy} and O(1)-p_x is constructive while for the O(1′)-p_y it is destructive.

the $k = [0, \pi]$ point in the Brillouin zone, shown in Figure 6.7, consists of O(1)-p_x orbital

lobes with the same phase the neighboring ruthenium orbitals and O(1′)-p_y orbitals with opposite phase. As a result, the γ band has much less O(1′)-p_y weight at the van Hove singularity and $K_{1'\perp}$ is less sensitive to the effect of tuning to the critical strain, evident in Figure 5.1. This effect is not taken into account in Equation 3.15, which assumes the two sites differ only by the hyperfine dipole coupling to each susceptibility. To account for this, let the γ-band overlap with the p-orbital of each site be given by $b_{\mathbf{k}} = \langle O_{2p}|u^{\gamma}_{\mathbf{k}}\rangle$. Then the full expression for the dipolar contribution to the oxygen shifts (from the γ band) becomes:

$$\begin{aligned} K^{\gamma}_{1\parallel} &= \frac{-Ag\mu_B}{2B}\int dE_{\mathbf{k}}dA_{\mathbf{k}}|b(1)_k|^2 \\ &\quad\times[g(E_{\mathbf{k}\downarrow},A_{\mathbf{k}})f(E_{\mathbf{k}\downarrow}) - g(E_{\mathbf{k}\uparrow},A_{\mathbf{k}})f(E_{\mathbf{k}\uparrow})] \\ &= -A\int dE_{\mathbf{k}}dA_{\mathbf{k}}|b(1)_k|^2\chi^{xy}_{\mathbf{k}} \end{aligned} \tag{6.6}$$

$$\begin{aligned} K^{\gamma}_{1'\perp} &= \frac{2Ag\mu_B}{2B}\int dE_{\mathbf{k}}dA_{\mathbf{k}}|b(1')_k|^2 \\ &\quad\times[g(E_{\mathbf{k}\downarrow},A_{\mathbf{k}})f(E_{\mathbf{k}\downarrow}) - g(E_{\mathbf{k}\uparrow},A_{\mathbf{k}})f(E_{\mathbf{k}\uparrow})] \\ &= 2A\int dE_{\mathbf{k}}dA_{\mathbf{k}}|b(1')_k|^2\chi^{xy}_{\mathbf{k}} \end{aligned} \tag{6.7}$$

where A is the dipolar coupling constant, $g(E_{\mathbf{k}\sigma},A_{\mathbf{k}})$ is the density of states, $f(E_{\mathbf{k}\sigma})$ is the Fermi function, and $\chi^{xy} = \int dE_{\mathbf{k}}dA_{\mathbf{k}}\chi^{xy}_{\mathbf{k}}$. The two linear combinations shown in Figure 5.2 **(b)** then become:

$$K^{s}_{1'\perp} - K^{s}_{1\parallel} = \frac{Ag\mu_B}{2B}\int dE_{\mathbf{k}}dA_{\mathbf{k}}\big(2|b(1')_k|^2 + |b(1)_k|^2\big)\chi^{xy}_{\mathbf{k}} \tag{6.8}$$

and

$$\frac{1}{2}K^{s}_{1'\perp} - K^{s}_{1\parallel} = \left[\frac{Ag\mu_B}{2B}\int dE_{\mathbf{k}}dA_{\mathbf{k}}\big(|b(1')_k|^2 + |b(1)_k|^2\big)\chi^{xy}_{\mathbf{k}}\right] + \frac{1}{2}C\chi^{xz/yz} \tag{6.9}$$

where C is the total coupling to the xz/yz orbitals. The first combination isolates the effect of the γ-band but is not directly proportional to the total susceptibility due to the momentum dependent $b_{\mathbf{k}}$ factors. The second combination represents an average of the response of the two oxygen sites along with an effectively constant offset due to coupling to the xz/yz bands.

Bibliography

[1] P.W. Anderson. "Theory of dirty superconductors". In: *Journal of Physics and Chemistry of Solids* 11.1 (1959), pp. 26–30.

[2] Takashi Ando et al. "Upper Critical Fields of the 3-K Superconducting Phase of Sr_2RuO_4". In: *Journal of the Physical Society of Japan* 68.5 (1999), pp. 1651–1656.

[3] K Andres, JE Graebner, and HR Ott. "4 f-Virtual-Bound-State Formation in $CeAl_3$ at Low Temperatures". In: *Physical Review Letters* 35.26 (1975), p. 1779.

[4] Mark E Barber. "Uniaxial stress technique and investigations into correlated electron systems". PhD thesis. University of St Andrews, 2017.

[5] Mark E Barber et al. "Resistivity in the vicinity of a van Hove singularity: Sr_2RuO_4 under uniaxial pressure". In: *Physical review letters* 120.7 (2018), p. 076602.

[6] John Bardeen, Leon N Cooper, and J Robert Schrieffer. "Microscopic theory of superconductivity". In: *Physical Review* 106.1 (1957), p. 162.

[7] Siham Benhabib et al. "Ultrasound evidence for a two-component superconducting order parameter in Sr_2RuO_4". In: *Nature physics* 17.2 (2021), pp. 194–198.

[8] C Bergemann et al. "Quasi-two-dimensional Fermi liquid properties of the unconventional superconductor Sr_2RuO_4". In: *advances in Physics* 52.7 (2003), pp. 639–725.

[9] David Sheridan Betts. "Refrigeration and thermometry below one Kelvin". In: (1976).

[10] Felix Bloch. "Nuclear induction". In: *Physical review* 70.7-8 (1946), p. 460.

[11] Felix Bloch. "Über die quantenmechanik der elektronen in kristallgittern". In: *Zeitschrift für physik* 52.7 (1929), pp. 555–600.

[12] I Bonalde et al. "Magnetic penetration depth and the symmetry of the order parameter in Sr_2RuO_4". In: *Physica C: Superconductivity* 341 (2000), pp. 1695–1696.

[13] Bulat Burganov et al. “Strain control of fermiology and many-body interactions in two-dimensional ruthenates”. In: *Physical review letters* 116.19 (2016), p. 197003.

[14] Alan Callaghan, Carl W Moeller, and Roland Ward. “Magnetic interactions in ternary ruthenium oxides”. In: *Inorganic Chemistry* 5.9 (1966), pp. 1572–1576.

[15] Aaron Chronister et al. *Tuning the Fermi Liquid Crossover in Sr_2RuO_4 with Uniaxial Stress*. 2021. arXiv: `2111.05570 [cond-mat.str-el]`.

[16] Leon N Cooper. “Bound electron pairs in a degenerate Fermi gas”. In: *Physical Review* 104.4 (1956), p. 1189.

[17] A Damascelli et al. “Fermi surface, surface states, and surface reconstruction in Sr_2RuO_4”. In: *Physical review letters* 85.24 (2000), p. 5194.

[18] Kazuhiko Deguchi, Z Q. Mao, and Yoshiteru Maeno. “Determination of the superconducting gap structure in all bands of the spin-triplet superconductor Sr_2RuO_4”. In: *Journal of the Physical Society of Japan* 73.5 (2004), pp. 1313–1321.

[19] JA Duffy et al. “Polarized-neutron scattering study of the cooper-pair moment in Sr_2RuO_4”. In: *Physical review letters* 85.25 (2000), p. 5412.

[20] Sayak Ghosh et al. “Thermodynamic evidence for a two-component superconducting order parameter in Sr_2RuO_4”. In: *Nature Physics* 17.2 (2021), pp. 199–204.

[21] Vadim Grinenko et al. “Split superconducting and time-reversal symmetry-breaking transitions in Sr_2RuO_4 under stress”. In: *Nature Physics* 17.6 (2021), pp. 748–754.

[22] Erwin L Hahn. “Spin echoes”. In: *Physical review* 80.4 (1950), p. 580.

[23] Elena Hassinger et al. “Vertical line nodes in the superconducting gap structure of Sr_2RuO_4”. In: *Physical Review X* 7.1 (2017), p. 011032.

[24] Frantisek Herman et al. “Deviation from Fermi-liquid transport behavior in the vicinity of a Van Hove singularity”. In: *Phys. Rev. B* 99 (18 May 2019), p. 184107.

[25] Clifford W Hicks et al. "Strong increase of T_c of Sr_2RuO_4 under both tensile and compressive strain". In: *Science* 344.6181 (2014), pp. 283–285.

[26] Clifford W. Hicks et al. "Limits on superconductivity-related magnetization in Sr_2RuO_4 and $PrOs_4Sb_{12}$ from scanning SQUID microscopy". In: *Phys. Rev. B* 81 (21 June 2010), p. 214501.

[27] *https://razorbillinstruments.com/uniaxial-strain-cell*.

[28] YH Huang and GB Chen. "A practical vapor pressure equation for helium-3 from 0.01 K to the critical point". In: *Cryogenics* 46.12 (2006), pp. 833–839.

[29] NE Hussey et al. "Normal-state magnetoresistance of Sr_2RuO_4". In: *Physical Review B* 57.9 (1998), p. 5505.

[30] T Imai et al. "^{17}O NMR Evidence for Orbital Dependent Ferromagnetic Correlations in Sr_2RuO_4". In: *Physical review letters* 81.14 (1998), p. 3006.

[31] K Ishida et al. "Anisotropic pairing in superconducting Sr_2RuO_4: Ru NMR and NQR studies". In: *Physical Review B* 56.2 (1997), R505.

[32] K Ishida et al. "Anisotropic Superconducting Gap in the Spin-Triplet Superconductor Sr_2RuO_4: Evidence from a Ru-NQR Study". In: *Physical review letters* 84.23 (2000), p. 5387.

[33] K. Ishida et al. "Spin-triplet superconductivity in Sr_2RuO_4 identified by ^{17}O Knight shift". In: *Nature* 396.17 (Dec. 1998), pp. 658–660.

[34] Kenji Ishida et al. "Reduction of the ^{17}O Knight shift in the superconducting state and the heat-up effect by NMR pulses on Sr_2RuO_4". In: *Journal of the Physical Society of Japan* 89.3 (2020), p. 034712.

[35] S-O Kaba and D Sénéchal. "Group-theoretical classification of superconducting states of strontium ruthenate". In: *Physical Review B* 100.21 (2019), p. 214507.

[36] Heike Kamerlingh Onnes. "The superconductivity of mercury". In: *Comm. Phys. Lab. Univ. Leiden* 122 (1911), pp. 122–124.

[37] A Yu Kitaev. "Fault-tolerant quantum computation by anyons". In: *Annals of Physics* 303.1 (2003), pp. 2–30.

[38] Shunichiro Kittaka et al. "Searching for gap zeros in Sr_2RuO_4 via field-angle-dependent specific-heat measurement". In: *Journal of the Physical Society of Japan* 87.9 (2018), p. 093703.

[39] Charles Kittel and Paul McEuen. *Kittel's Introduction to Solid State Physics*. John Wiley & Sons, 2018.

[40] Steven Allan Kivelson et al. "A proposal for reconciling diverse experiments on the superconducting state in Sr_2 RuO_4". In: *npj Quantum Materials* 5.1 (2020), pp. 1–8.

[41] Fabian B Kugler et al. "Strongly Correlated Materials from a Numerical Renormalization Group Perspective: How the Fermi-Liquid State of Sr_2RuO_4 Emerges". In: *Physical Review Letters* 124.1 (2020), p. 016401.

[42] Lev Davidovich Landau. "The theory of a Fermi liquid". In: *Soviet Physics Jetp-Ussr* 3.6 (1957), pp. 920–925.

[43] You-Sheng Li et al. "Elastocaloric determination of the phase diagram of Sr_2RuO_4". In: *arXiv preprint arXiv:2201.04147* (2022).

[44] You-Sheng Li et al. "High-sensitivity heat-capacity measurements on Sr_2RuO_4 under uniaxial pressure". In: *Proceedings of the National Academy of Sciences* 118.10 (2021).

[45] GM Luke et al. "Unconventional superconductivity in Sr_2RuO_4". In: *Physica B: Condensed Matter* 289 (2000), pp. 373–376.

[46] Yongkang Luo et al. "Normal state ^{17}O NMR studies of Sr_2RuO_4 under uniaxial stress". In: *Physical Review X* 9.2 (2019), p. 021044.

[47] C Lupien et al. "Ultrasound attenuation in Sr_2RuO_4: An angle-resolved study of the superconducting gap function". In: *Physical review letters* 86.26 (2001), p. 5986.

[48] A. P. Mackenzie et al. "Extremely Strong Dependence of Superconductivity on Disorder in Sr_2RuO_4". In: *Phys. Rev. Lett.* 80 (1 Jan. 1998), pp. 161–164.

[49] Andrew P Mackenzie et al. "Even odder after twenty-three years: the superconducting order parameter puzzle of Sr_2RuO_4". In: *npj Quantum Materials* 2.1 (2017), pp. 1–9.

[50] Andrew P Mackenzie et al. "The Fermi Surface Topography of Sr_2RuO_4". In: *Journal of the Physical Society of Japan* 67.2 (1998), pp. 385–388.

[51] Andrew Peter Mackenzie and Yoshiteru Maeno. "The superconductivity of Sr_2RuO_4 and the physics of spin-triplet pairing". In: *Reviews of Modern Physics* 75.2 (2003), p. 657.

[52] AP Mackenzie et al. "Quantum Oscillations in the Layered Perovskite Superconductor Sr_2RuO_4". In: *Physical review letters* 76.20 (1996), p. 3786.

[53] AP Mackenzie et al. "Quantum Oscillations in the Layered Perovskite Superconductor Sr_2RuO_4". In: *Physical review letters* 76.20 (1996), p. 3786.

[54] Y Maeno et al. "Superconductivity in a layered perovskite without copper". In: *nature* 372.6506 (1994), pp. 532–534.

[55] Yoshiteru Maeno et al. "Two-dimensional Fermi liquid behavior of the superconductor Sr_2RuO_4". In: *Journal of the Physical Society of Japan* 66.5 (1997), pp. 1405–1408.

[56] Anton V Matasov. "Prediction of the critical temperature of unconventional superconductors based on the plasmon mechanism". In: *AIP conference proceedings*. Vol. 2163. 1. AIP Publishing LLC. 2019, p. 020005.

[57] GJ McMullan, MP Ray, and RJ Needs. "Comparison of the calculated and observed Fermi surfaces of Sr_2RuO_4". In: *Physica B: Condensed Matter* 223 (1996), pp. 529–531.

[58] Tôru Moriya. "The effect of electron-electron interaction on the nuclear spin relaxation in metals". In: *Journal of the Physical Society of Japan* 18.4 (1963), pp. 516–520.

[59] Hidekazu Mukuda et al. "Novel Character of Spin Fluctuations in Spin-Triplet Superconductor Sr_2RuO_4: ^{17}O-NMR Study". In: *Journal of the Physical Society of Japan* 67.11 (1998), pp. 3945–3951.

[60] Shuji NishiZaki, Yoshiteru Maeno, and Zhiqiang Mao. "Changes in the Superconducting State of Sr_2RuO_4 under Magnetic Fields Probed by Specific Heat". In: *Journal of the Physical Society of Japan* 69.2 (2000), pp. 572–578.

[61] David Pines. *Theory of Quantum Liquids: Normal Fermi Liquids*. CRC Press, 2018.

[62] R Radebaugh. "US National Bureau of Standards Technical Note". In: (1967).

[63] Nicholas Read and Dmitry Green. "Paired states of fermions in two dimensions with breaking of parity and time-reversal symmetries and the fractional quantum Hall effect". In: *Physical Review B* 61.15 (2000), p. 10267.

[64] TM Rice and M Sigrist. "Sr_2RuO_4: an electronic analogue of 3He?" In: *Journal of Physics: Condensed Matter* 7.47 (1995), p. L643.

[65] Henrik S Røising et al. "Superconducting order of Sr_2RuO_4 from a three-dimensional microscopic model". In: *Physical Review Research* 1.3 (2019), p. 033108.

[66] AT Rømer et al. "Knight shift and leading superconducting instability from spin fluctuations in Sr_2RuO_4". In: *Physical review letters* 123.24 (2019), p. 247001.

[67] Rahul Sharma et al. "Momentum-resolved superconducting energy gaps of Sr_2RuO_4 from quasiparticle interference imaging". In: *Proceedings of the National Academy of Sciences* 117.10 (2020), pp. 5222–5227.

[68] KM Shen et al. "Evolution of the Fermi surface and quasiparticle renormalization through a van Hove singularity in $Sr_{2-y}La_yRuO_4$". In: *Physical review letters* 99.18 (2007), p. 187001.

[69] Y Sidis et al. "Evidence for incommensurate spin fluctuations in Sr_2RuO_4". In: *Physical review letters* 83.16 (1999), p. 3320.

[70] Manfred Sigrist. "Introduction to unconventional superconductivity". In: *AIP Conference Proceedings*. Vol. 789. 1. American Institute of Physics. 2005, pp. 165–243.

[71] Charles P Slichter. *Principles of magnetic resonance*. Vol. 1. Springer Science & Business Media, 2013.

[72] Veronika C. Stangier, Erez Berg, and Jörg Schmalian. "Breakdown of the Wiedemann-Franz law at the Lifshitz point of strained Sr_2RuO_4". In: *Phys. Rev. B* 105 (11 Mar. 2022), p. 115113.

[73] P Steffens et al. "Spin fluctuations in Sr_2RuO_4 from polarized neutron scattering: implications for superconductivity". In: *Physical Review Letters* 122.4 (2019), p. 047004.

[74] Alexander Steppke et al. "Strong peak in T_c of Sr_2RuO_4 under uniaxial pressure". In: *Science* 355.6321 (2017), eaaf9398.

[75] Han Gyeol Suh et al. "Stabilizing even-parity chiral superconductivity in Sr_2RuO_4". In: *Physical Review Research* 2.3 (2020), p. 032023.

[76] Veronika Sunko et al. "Direct observation of a uniaxial stress-driven Lifshitz transition in Sr_2RuO_4". In: *npj Quantum Materials* 4.1 (2019), pp. 1–7.

[77] Anna Tamai et al. "High-resolution photoemission on Sr_2RuO_4 reveals correlation-enhanced effective spin-orbit coupling and dominantly local self-energies". In: *Physical Review X* 9.2 (2019), p. 021048.

[78] Michael Tinkham. *Introduction to superconductivity*. Courier Corporation, 2004.

[79] Roland Willa et al. "Inhomogeneous time-reversal symmetry breaking in Sr_2RuO_4". In: *Physical Review B* 104.2 (2021), p. 024511.

[80] Jing Xia et al. “High resolution polar Kerr effect measurements of Sr_2RuO_4: Evidence for broken time-reversal symmetry in the superconducting state”. In: *Physical review letters* 97.16 (2006), p. 167002.

[81] Shingo Yonezawa, Tomohiro Kajikawa, and Yoshiteru Maeno. “First-order superconducting transition of Sr_2RuO_4”. In: *Physical review letters* 110.7 (2013), p. 077003.

[82] Shingo Yonezawa, Tomohiro Kajikawa, and Yoshiteru Maeno. “Specific-heat evidence of the first-order superconducting transition in Sr_2RuO_4”. In: *Journal of the Physical Society of Japan* 83.8 (2014), p. 083706.

[83] Kei Yosida. “Paramagnetic susceptibility in superconductors”. In: *Physical Review* 110.3 (1958), p. 769.